Environmental Resuspension and Health Impacts of Radioactive Particulate Matter

A dissertation by

Shaun Alan Marshall

for the

Department of Physics

in partial fulfillment of the requirements
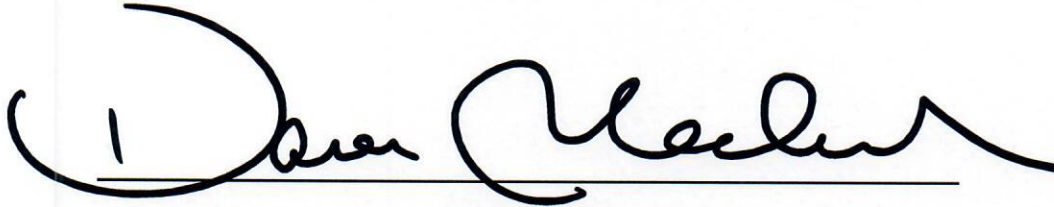for the degree of

Doctor of Philosophy

in the subject of

Physics

Dissertation Committee Approval

David Medich, CHP, Ph.D.

Associate Professor

Primary Adviser

Charles Potter, CHP, Ph.D.

Distinguished System Research & Analysis

Committee Member

Germano Iannacchione

Germano Iannacchione, Ph.D.

Professor

Committee Member

Abstract

Surface-bound particulates containing radionuclides in the environment can become airborne through the process of resuspension. Once airborne, these radionuclides can be inhaled or ingested to deliver an internal dose of ionizing radiation. To that end, the resuspension factor method is a powerful tool for predicting a person's exposure to airborne particles from surface contaminations, and therefore is used to determine protective and intervening measures. The resuspension factor is calculated as the ratio measured airborne to surface mass concentration and has been found to generally decrease exponentially with time. Current models of the resuspension factor are empirical and have failed to predict recent measurement, motivating a stronger basis and physical model for the system. Additionally, federal guidances conservatively suggest an unphysical model of particulate radioactivity impact wherein the entirety of the radiation is absorbed.

For this dissertation, two- and three-compartment catenary models were derived which build on measured resuspension rate constants under various influences. These models were fit to a set of historic observations of resuspension factors using an instrumental uncertainty-weighting to resolve the large variances early in time which otherwise inflate calculations. When compared to previous resuspension models, our physical models better fit the data achieving reduced-χ^2 closer to 1.

An experiment was undertaken to validate our basic environment resuspension models in an urban environment without wind. A resuspension chamber is constructed by placing an acrylic tube atop a poured concrete surface and lowering a low-volume air sampler head from above. Europium oxide powder was dispersed upon the surface or from above the air sampling height to emulate ideal compartmentalized release scenarios, and air is sampled on an hourly, daily, or weekly basis. Sampler filters then were evaluated for Europium content using neutron activation and gamma spectroscopy. Hourly measurements following airborne release are within an order of magnitude of early-timeframe historic resuspension factors ($\sim 10^{-6}$ m^{-1}), whereas daily and weekly measure-

ments from surface release demonstrate a gradual decrease in resuspension factor ($\sim 10^{-8}$ m^{-1}). These results support a need to critically assess the resuspension factor definition and its relationship to "initial suspension" and the indoor background, non-anthropogenic resuspension.

Finally, a simulated model was generated to demonstrate loss of alpha radiation from relevant transuranic radioparticles. This was accomplished using the Geant4 Monte Carlo particle transport code. This basic model demonstrated a clear loss of average intensity and energy of exiting particles which are both directly related to the absorbed dose. The data shows a loss from 10 to 90% of intensity to occur at particle sizes approaching the range of alphas within them, and a loss of roughly half the initial alpha energy at around the same particle sizes. The results establish a first-order baseline for a particulate self-absorption model which complement existing dosimetry models for inhaled radionuclides.

Contents

List of Figures

List of Tables

Chapter 1

Introduction

1.1 Health Risks from Exposure to Radioactive Particulate Matter

1.1.1 Exposure to Ionizing Radiation

Sources of radioactivity may be broadly classified as primordial, cosmogenic, and anthropogenic (Eisenbud and Gesell, 1997). The former two categories make up the natural sources of ionizing radiation, which accounts for almost half of the an individual's average annual radiation exposure in the US. The most prominent concern among naturally occuring radioactivity is the presence of radioactive radon which is a decay product of primordial uranium. Radon is a gas which can enter into buildings and decay further into radioactive dust aggregates.

The largest component of background anthropogenic radiation exposure is the usage for medical diagnosis and treatment of diseases. A small fraction of this value can arise from consumer items and activies including building materials and air travel. In rare events, individuals can be exposed to additional sources of artificially produced radioactive particles. These include over 2000 weapons tests globally since 1945, accidents involving the nuclear devices, emissions from civilian nuclear

accidents, and releases from dumped nuclear material (Salbu and Lind, 2005).

The presence of inhaled particulates containing radionuclides pose a unique risk due to radiation induced biological damage. Radionuclides, isotopes of elements with a finite nuclear lifespan, disintegrate into a more preferable nuclear state spontaneously, though with characteristic average lifespans; a measurement of radioactive decay events will follow an exponential distribution. This distribution is characterized by the half-life, τ, the average time required to observe half of the remaining radioactive events in the quantity at hand to decay. A key component of these events is the release of energy in the form of radiation. There are numerous nuclear and sub-nuclear states which can radiate out from the decay reactions; the most common are:

- **Alpha (α):** A $+2e$ charge ion composed of two protons and two neutrons. Generally a by-product of larger radioisotopes like members of the uranium or thorium decay chain, this decay reduces the atomic number by 2, changing the elemental identity accordingly (Fig. 1.1).

- **Beta [minus] ($\beta-$):** A $-1e$ charge election, resulting from the conversion of a neutron to a proton. This reaction also gives rise to a high-speed anti-neutrino ($\bar{\nu}$), whose likelihood to interact with nuclei are so insignificant that they are practically ignored in the study of biological effects.

- **Gamma (γ):** A chargeless, high energy photon emitted from the electromagnetically unstable radionuclide. The resulting nuclear isotope is unchanged, but the energy of the photon is often in the keV to MeV range; well beyond visible and ultraviolet light frequencies.

- **Neutron (n):** A chargeless particle, with a mass comparable to the proton, their nuclear complement. Free neutrons have a half-life of just over 10 minutes, and are therefore a common indicator of artificial to anthropogenic radioactivity. Spontaneous fission is the only naturally-occurring decay mode which produces neutrons.
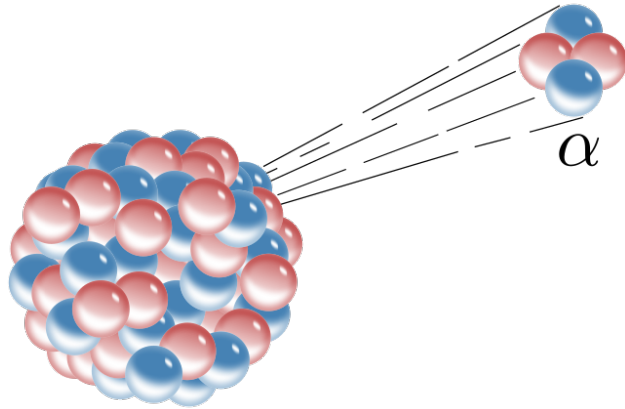
Figure 1.1: Cartoon diagram of alpha particle radiation from decay event.

Radiation produced by decay events is ionizing, meaning it is capable of imparting enough energy into atoms and molecules through one or more interactions that bound electrons are ejected as radiation. The quantities are given in terms of an *absorbed dose*- the energy deposited in a material divided by the mass of the material, in gray (Gy) $\left(1 \text{ Gy} = 1 \ \dfrac{\text{J}}{\text{kg}}\right)$. The concern of exposure to ionizing radiation is its capacity to damage and destroy DNA, producing either deterministic health effects or stochastic effects such as cancer.

The absorbed dose of ionizing radiation from a specific type of radiation can be made comparable to other types of by using a *radiation quality factor*. Each radiation type is weighted with a value normalized to γ-radiation. This factor is used to relate the relative onset of producing tumors in biological media; for neutrons, this has been found to vary significantly with energy. Table 1.1 shows the different quality factor multipliers based on the radiation type. Each type of radiation carries an equivalent dose, in sieverts (Sv), a weighted risk relative to a gamma ray of equal energy. Further, particular critical organs are more *radiosensitive* or *radioresistant* than others— the effective dose relates the risk of long-term tumor development effect relative to an average dose delivered to a whole body (Turner, 1986).

3

Table 1.1: Quality factors of equivalent dose by LET and radiation type (Turner, 1986)

Radiation	LET (keV/μm)	Quality factor
gamma, x-ray	any	1
beta+, beta-	any	1
	3.5	1
	3.5—7.0	1—2
alpha, ions	7.0-23	2—5
	23—53	5—10
	53—175	10—20

To control the risk present with ionizing radiation, the US enforces regulatory limits on the total exposure to radiation from licensed occupational and non-occupational activities through the Nuclear Regulatory Agency. This agency is responsible for maintaining and enforcing federal code 10 CFR 20: Standards for Protection Against Radiation. These regulations specify that radiological workers may be exposed to 5 rem (50 mSv) effective whole body dose, or 50 rem (0.5 Sv) to a specific organ annually (NRC, 2020).

1.1.2 Exposure to Particulate Matter

A person's risks from inhaling or ingesting particulate matter can depend upon a number of physic-ochemical factors such as: surface and interaction chemistry, the particle size distribution, and the trace element contents (Harrison and Yin, 2000). The particle shape results from both its creation process (whether nucleating in the atmosphere or through geological or anthropogenic activity), so attribution to particle size refers to the aerodynamic diameter, or the diameter of an equivalent spherical particle of the same gravitational settling rate. Inhalable particles are those smaller than 10 μm (also referred to as PM_{10} in air quality measurements), though it became clear by the 1990's that particulate matter smaller than 2.5 μm ($PM_{2.5}$, or *fine inhalable particles*) were respirable (able to enter gas-exchange regions of lungs) and were worth quantifying specifically (Dockery, 2009).

The World Health Organization (WHO) has recognized that exposure to air pollutants, including fine particulate matter, is a leading risk factor for an array of health effects including heart disease, inflammation, heart rate and blood pressure variations, and death (WHO, 2015; Brook et al., 2010). A recent evaluation of the health effects data from epidemiological, toxicological, and controlled studies connected specific pollutants to quantifiable observations. These include natural sources such as crustal aluminum, calcium, silicon, and iron producing an increase in hospital admissions, arterial narrowing, systemic inflammation, and mortality. The evaluation also considered anthropogenic sources such as gasoline exhaust, diesel exhaust, resuspended road dust, wood smoke, and oil-fired power plant emissions producing primarily increased mortality among increased hospital and emergency room visits and heart rate variation (Stanek et al., 2011).

Exposure to $PM_{2.5}$ and PM_{10} in relation to health risks is measured as an average airborne concentration, often expressed in units of μg/m^3, or ng/m^3 for trace quantities. Figure 1.2 depicts a dose-mortality response curve from an aggregate study of the largest US cities in the early 1990s.

Like the dose-response curves of ionizing radiation, the generally accepted trend is an increasing risk with particulate matter concentration, but there is debate on the exact behavior of the function at low doses (Daniels et al., 2000). Environmental monitoring of airborne particulate matter generally involves taking volumetric air samples followed by analyzing the filter or collection basin for content. Short-term exposures therefore have to be weighted against a reference timeframe to determine the effective dose in $\mu g/m^3$.
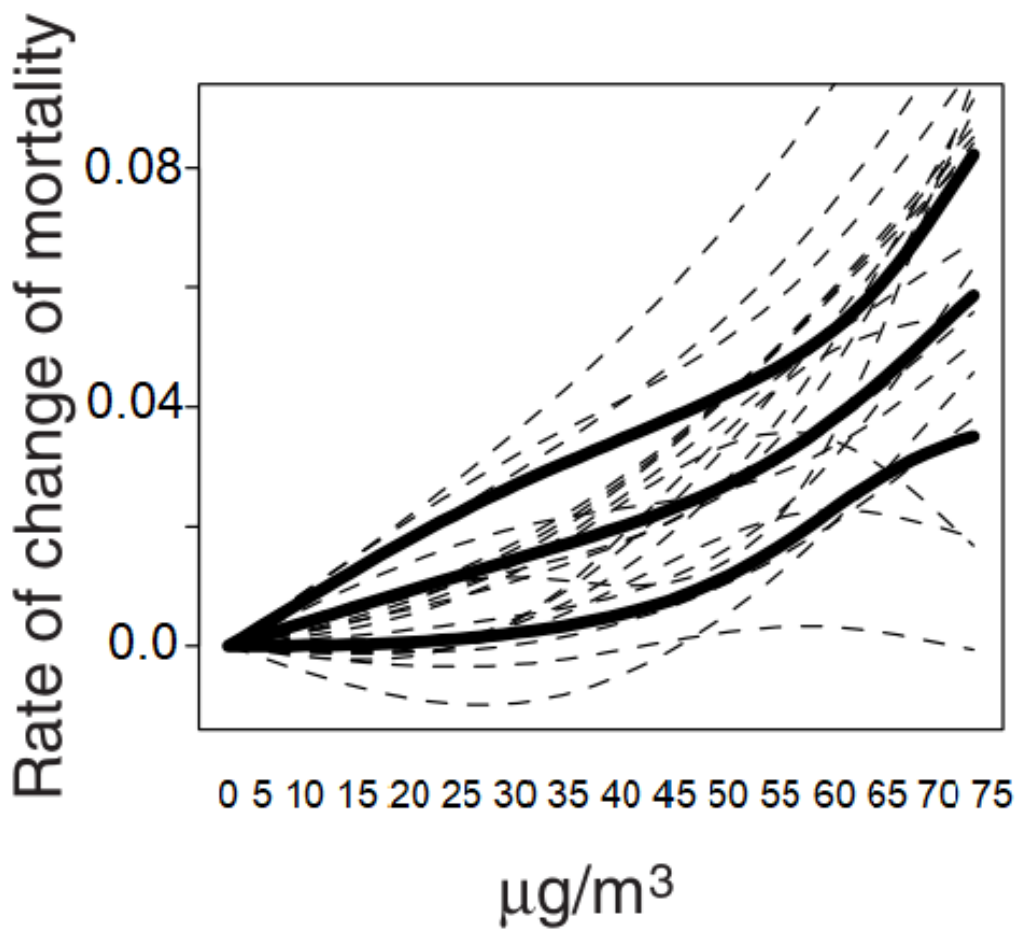
Figure 1.2: Particulate matter <10 μm in aerodynamic diameter (PM$_{10}$) total mortality rate dose-response curve for the mean lag PM$_{10}$ and 95% credible regions (solid lines), 20 largest US cities, 1987-1994. Dashed lines denote the Bayesian estimates of the city-specific dose-repsonse curves (Daniels et al., 2000).

1.1.3 Exposure to Radioactive Particulate Matter

Historical Radionuclide Resuspension Factor

Radiation doses receceived by individuals is a critical health physics calculation for emergency planning and response, active monitoring, and nuclear security limits. This is particularly true for alpha emitting radionuclides, whose delivered internal dose can far exceed external doses. In order to accurately construct the exposure profile for predictive purposes, the physical and chemical properties of the material and interactions with the environment must be precisely known. One such property, the resuspension factor, directly relates an individuals internal exposure of inhaled radionuclides to a known areal contamination.

The dose evaluation through the resuspension factor method is inherently complex and site-specific. This is primarily due to the high variability of the resuspending influences acting upon deposited particulates, such as aerosol size distribution (Karlsson et al., 1996), ambient temperature and pressure (Xu et al., 2016), humidity (Kim et al., 2016), vegetation and rainfall (Dreicer et al., 1984), and lateral wind speed (Harris and Davidson, 2008). At the Nevada Test Site, the plutonium dispersal tests known as Project 56 enabled the development of the resuspension factor S_f (Langham et al., 1955) as a metric to predict radiogenic risk from inhaled resuspended particulates. This method of taking the ratio of the volumetric airborne radioactivity to the surface area radioactivity directly beneath requires details of event conditions and available resuspending mechanisms (Langham, 1971), but remained successful in identifying a nonlinear decay of the suspended particulates over time following the dispersion (Garland, 1983; Tveten, 1990; Garland and Pomeroy, 1994). As an alternative, Brodsky proposed a maximum constant resuspension factor for conservative long-term predictions of 10^{-6} Bq m^2 $\left(\text{Bq m}^3\right)^{-1}$ (Brodsky, 1980). Most functional models have leaned towards exponential behavior rather than polynomial or power-law (Garger et al., 1999). Applying these sensitive approximations to early time-frames following deposition led to potentially 10—100x more conservative estimates than recent observations. (Maxwell and Anspaugh, 2011).

Resuspension models have been developed for use in prospective dose evaluations using data from existing studies, with measurements taken from opportunistic or specific experimental design to estimate of resuspension. The nominal reference for resuspension is NCRP Report 129 (NCRP, 1999). A more recent review and analysis in support of the Federal Radiological Monitoring and Assessment Center (FRMAC) was conducted by Maxwell and Anspaugh in 2011 the results of which are currently being used by the FRMAC community (2011). A review of the available data and methodologies resulted in a desire to determine if resuspension properties including chemical interactions with surface materials and particle size of resuspended material could be determined to develop a more holistic model that would apply to a particular radionuclide. Americium-241, being a current radionuclide of interest, was chosen for this study.

The Federal Radiological Monitoring and Assessment Center (FRMAC) publishes the *FRMAC Assessment Manual* (FRMAC, 2018) for determining action limits in the event of a radiological incident. These limits are represented by dose response levels (DRLs) which are based on the Protective Action Guide (EPA, 2017) developed by the US Environmental Protection Agency (EPA) and the Department of Homeland Security (DHS) for planned maximum dose anually. In calculating this limit, exposure pathways are considered separately, then combined, including the deposition inhalation dose parameter D_{inh} (Sv) from inhaling resuspended radionuclides from a contaminated area (Eq. 1.1, simplified from the version the assessment manual):

$$D_{inh} = C_{D,inh} \times \bar{f}_B \times KP, \tag{1.1}$$

- $C_{D,inh}$ is the inhalation committed dose coefficient for some radionuclide (Sv Bq^{-1}),

- $\bar{f}_B$ is the activity-averaged human breathing rate (usually taken as 0.92 m^3 h^{-1})

- KP is the resuspension parameter (Bq s m^{-3}), which considers airborne concentration of the radionuclide during the given time phase, with radioactive decay/in-growth and resuspension factor K_t (Eq. 1.2):

$$KP = \int_{t_1}^{t_2} K(t) \times Dp \times e^{-\lambda t} \, dt, \tag{1.2}$$

- Dp is the initial deposition of the radionuclide (Bq)

- λ is the decay coefficient of the radionuclide (s^{-1})

- $K(t)$ is the current empirical resuspension factor, which is that reported by Maxwell and Anspaugh (2011) (Eq. 1.3):

$$K(t) = \left(10^{-5}\right) e^{-\left(8.1 \times 10^{-2}\right)t} + \left(7 \times 10^{-9}\right) e^{-\left(2.31 \times 10^{-3}\right)t} + 10^{-9}. \tag{1.3}$$

The resuspension factor K_t (m^{-1}) as a function of time t (s) is computed by dividing the air activity concentration (Bq m^{-3}) by the areal activity of the deposition (Bq m^{-2}). To avoid the affects of confounding factors, data collection should be taken under calm, isolated conditions. Anthropological mechanical disturbances, including the induced turbulence from the walking of a passerby, have been to produce resuspension levels of 10^{-10} to 10^{-2} (Langham, 1971).

Radioparticulate Self-Attenuation

Radioparticulates will block a fraction of the particles and total outward energy emitted from internal decays. This process could be termed *self-attenuation* or *self-shielding* of the flux, though the latter does not appear widespread. There have been a number of studies into radioactive matter *self-shielding* but depending upon the context the definitions are split as to whether it implies:

1. the shielding of the object or part of an object *from external radiation* due to the object's molecular composition and structure, or

2. the shielding of exposed individuals *from radiation emitted from the object* due to the object's molecular composition and structure.

The former often comes into question when performing neutron activation analysis on geometrically large samples (Trkov et al., 2009). One recent study investigates the *self-shielding* of Boron-doped concrete which contained large granular Boron macrostructures (DiJulio et al., 2018). The aggregation of Boron in the concrete means that a proportion of the Boron concentration in the concrete was inaccessible to the incident external neutrons, which consequentially means there are regions with a lower than average Boron concentration, reducing the overall shielding capability (of exposed individuals) of the material. In another study, the shielding factor of tree-ring samples are systematically calculated and simulated to demonstrate a drop in detection efficiency due to gamma rays exiting through a bulk of organic matter (Sahin and Unlu, 2012).

Self-shielding *from* radioactive matter in a radiation protection context has largely been omitted from dose assessments. Instead, the particles are assumed to be uniform spheres containing an activity directly proportional to particle size (Voss, 2001). This leads to a general overestimation of both internal and external dose. This is especially present in the case of low-energy beta radiation and a wider spectrum of alpha radiation, but is usually negligible for gamma radiation (Pollanen, 2002). A recent simulation study of beta emissions absorbed by particulates in the nasal

cavity found a 20-90% loss of lower energy betas compared to the conventional no-attenuation prediction (Moussa, 2007). An analytical form of the fraction of exiting beta particles termed the *self-absorption factor* (SAF) as a function of particle diameter d_p and attenuation coefficient μ_p is given in Eq. 1.4 (Pollanen, 2002).

$$SAF_{\beta-} = \frac{2}{\mu_p d_p} - \frac{2}{(\mu_p d_p)^2}\left[1 - e^{-\mu_p d_p}\right] \approx 1 - \frac{\mu_p d_p}{3} \quad \text{when } \mu_p d_p \ll 1 \qquad (1.4)$$

In nuclear decommissioning, it is possible to encounter particles of large enough sizes (including larger inhalable airborne dusts) that may produce a lower gamma-ray field due to self-shielding. In one simulation study, an equation for intensity of gamma radiation emitted by uniform spherical particles (Eq. 1.5) is found explicitly (Gamage and Joyce, 2011) in terms of the particle density ρ, attenuation coefficient μ, decay gamma yield γ and particle radius r. This model is used to compute the relative loss in intensity for Pu-239 oxide particles (Fig. 1.3).
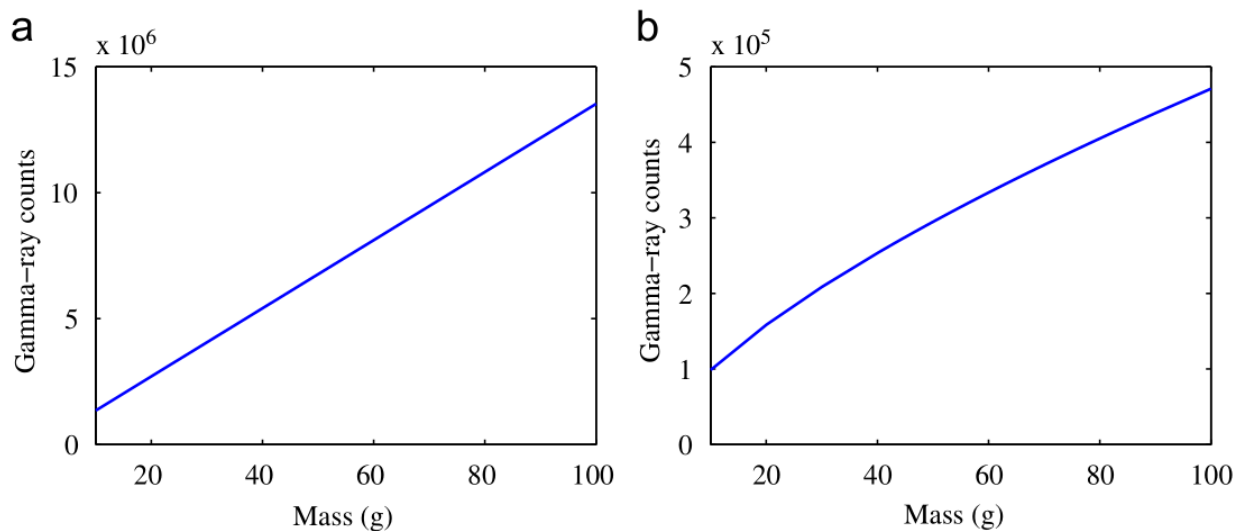
Figure 1.3: The self-shielding effect on 129 keV γ-ray counts for plutonium-239 as a function of the mass of the spherical radioactive deposit: (a) without and (b) with self-shielding (Gamage and Joyce, 2011).

The related SAF_γ for the fractional gamma intensity exiting the particle is thus the ratio of this

corrected intensity to the initial intensity I_0 (Eq. 1.6). An explicit form of this ratio, which may be termed the *self-shielding factor* or *source efficiency*, was also recently determined for cylindrical radioactive sources (Eq. 1.7) which should be employed when such sources are used to calibratibrate efficiencies for gamma spectroscopic systems (Valentin et al., 2012; Krar and Milad, 2015).

$$I(r) = \frac{4\pi\rho\gamma}{\mu^3} \left[r^2\mu^2 - 2r\mu + 2 - 2e^{-\mu r} \right] \tag{1.5}$$

$$SAF_{\gamma,sphere} = \frac{I(r)}{I_0} = \frac{4\pi\rho\gamma}{I_0\mu^3} \left[r^2\mu^2 - 2r\mu + 2 - 2e^{-\mu r} \right] \tag{1.6}$$

$$SAF_{\gamma,cylinder} = \frac{2\int_0^L \int_0^R P_{element}\rho d\rho dZ}{R^2 L}, \tag{1.7}$$

$$\text{where } P_{element} = \begin{cases} Z/|cos\theta| & \text{through the bottom} \\ \dfrac{\rho\cos\phi + \sqrt{(\rho\cos\phi)^2 + R^2 - \rho^2}}{\sin\theta} & \text{through the side} \\ (L-Z)/|cos\theta| & \text{through the top} \end{cases}$$

An explicit form for the self-absorption factor for specific geometries of alpha-emitting particles has not been explicitly derived. There has been progress in quantifying the self-shielding of alphas in inhaled airborne particulate, including an assessment of small mammal lung dose rates. A Monte Carlo simulation of alphas emitted from a homogenous spherical particle determined that the average yield of alphas emitted from a ^{239}Pu particle less than 5 μm is 85% and that the energy loss to the particulate rises above 10% for particles larger than 1 μm (Caffrey et al., 2017).

The range of an ionizing particle in a material is the cumulative sum of the stopping power for each step of remaining energy of the particle; that is, the integral of the inverse of stopping power (Eq. 1.8). Stopping powers can be calculated using the Bethe formula (Eq. 1.9) for the kinetic energy T of a heavy ion within the medium of the material. A simplified form of the equation is also given (Eq. 1.10) which uses only the ion atomic number z, the electron volume density of the material n, the ratio of the ion speed to that of light β, and the mean excitation energy of the material (in eV) I_{eV} (Turner, 1986).

$$R_\alpha(T) = \int_0^T \left(-\frac{dE}{dx}(\beta(T)) \right)^{-1} dE \tag{1.8}$$

$$-\frac{dE}{dx} = \frac{4\pi z^2 e^4 n}{mc^2 \beta^2} \left[\ln\left(\frac{2mc^2\beta^2}{I(1-\beta^2)} \right) - \beta^2 \right] \tag{1.9}$$

$$-\frac{dE}{dx} = \frac{5.09 \times 10^{-25} z^2 n}{\beta^2} \left[\ln\left(\frac{1.02 \times 10^6 \beta^2}{I_{eV}(1-\beta^2)} \right) - \beta^2 \right] \quad \frac{\text{MeV}}{\text{cm}} \tag{1.10}$$

For particles with diameter less than $2 \times R_\alpha$, these is expected to be almost no loss of alpha emissions from the particle with some variance due to the rare multiple scattering interactions preventing exit. In addition, due to the linear loss of energy of a particle's stopping power, the average energy of an exiting alpha can be approximated by establishing: (1) the average location of an alpha emission, and (2) the average distance the alpha radiation then travels. The variance of the exiting energy initially increases with the particle size as the radial distribution of decay locations emit on average higher alpha energies at larger radii. As the particle size increases beyond $2 \times R_\alpha$, only decays a radial thickness of R_α from the edge escape. The energy variance then increases as alphas from this radial *skin* gradually lose large polar angle emissions to the particle at larger sizes.

13

1.2 Environmental Transport of Particulate Matter

1.2.1 Particulate Transport Mechanisms

Turbulent Diffusion (Atmospheric Removal)

Diffusion of contaminant aerosols in the atmosphere is governed by the atmosperic conditions. This presents a wide range of possible diffusion coefficients (a measure of the rate of the diffuse surface area growth) for the transport of the particles- 0.2 cm^2 s^{-1} for molecular diffusion and 10^{11} cm^2 s^{-1} for large-scale cyclonic storms. Due to the height dependence of temperature, also called the *lapse rate* in the lower atmosphere (troposphere), there is a natural convective diffusion. As parcels of air move from lower to higher altitudes the temperature tends to decrease, with the exception of an *inversion* condition where the reverse occurs, generally due to a passing warm front or the nightly cooling of the surface and thus lower atmosphere (Fig. 1.4). The strength and combination of lapse and inversion conditions give rise to numerous plume profiles for a continuous-emission source, demonstrated in Figure 1.5 (Eisenbud and Gesell, 1997). These behaviors result in drastically different temporal and spatial air concentrations.
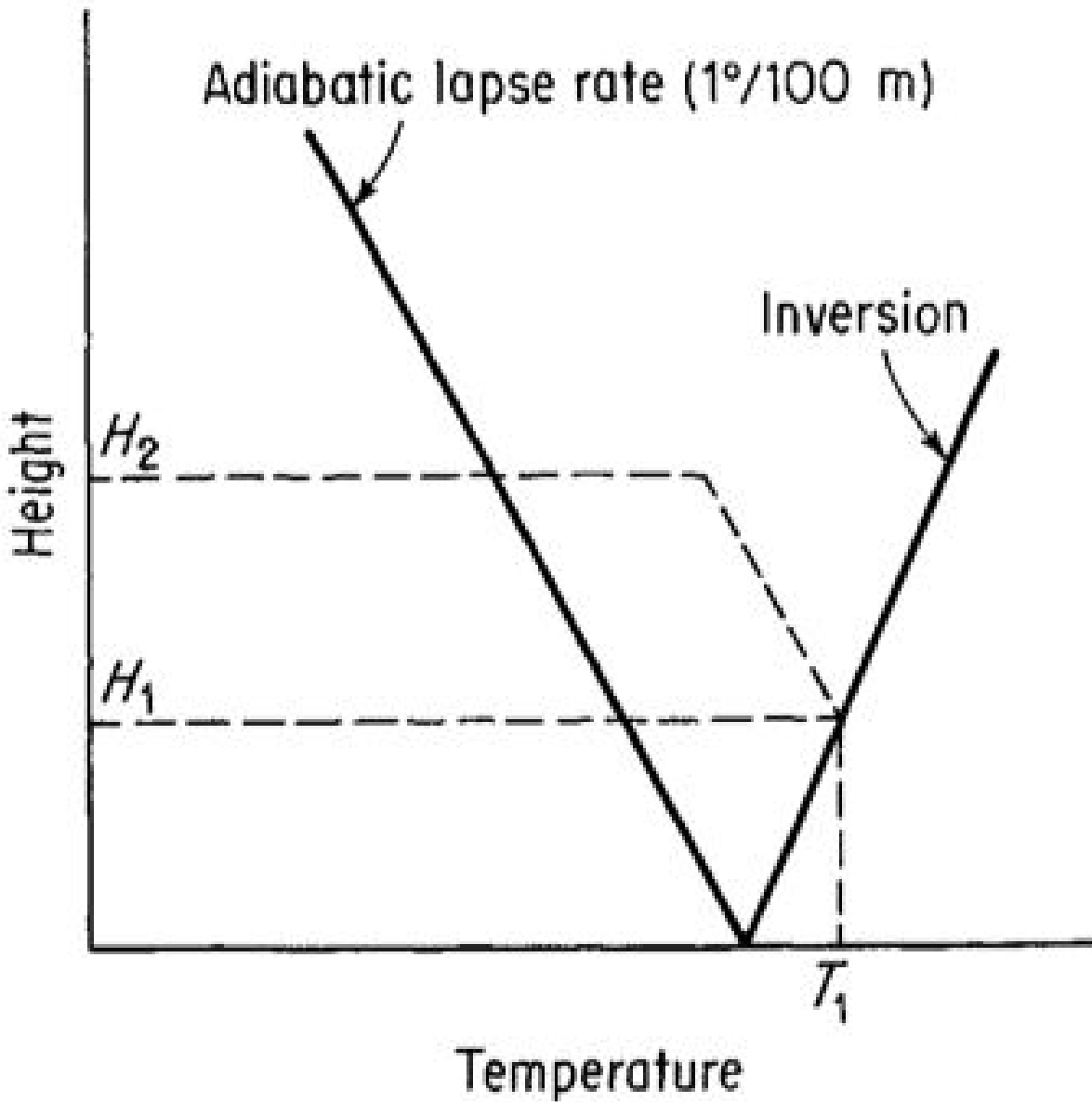
Figure 1.4: Inherent stability of the inverted temperature gradient. A parcel of air raised in height fro, H_1 to H_2, condenses adiabatically, then sinks to its original position (Eisenbud and Gesell, 1997).
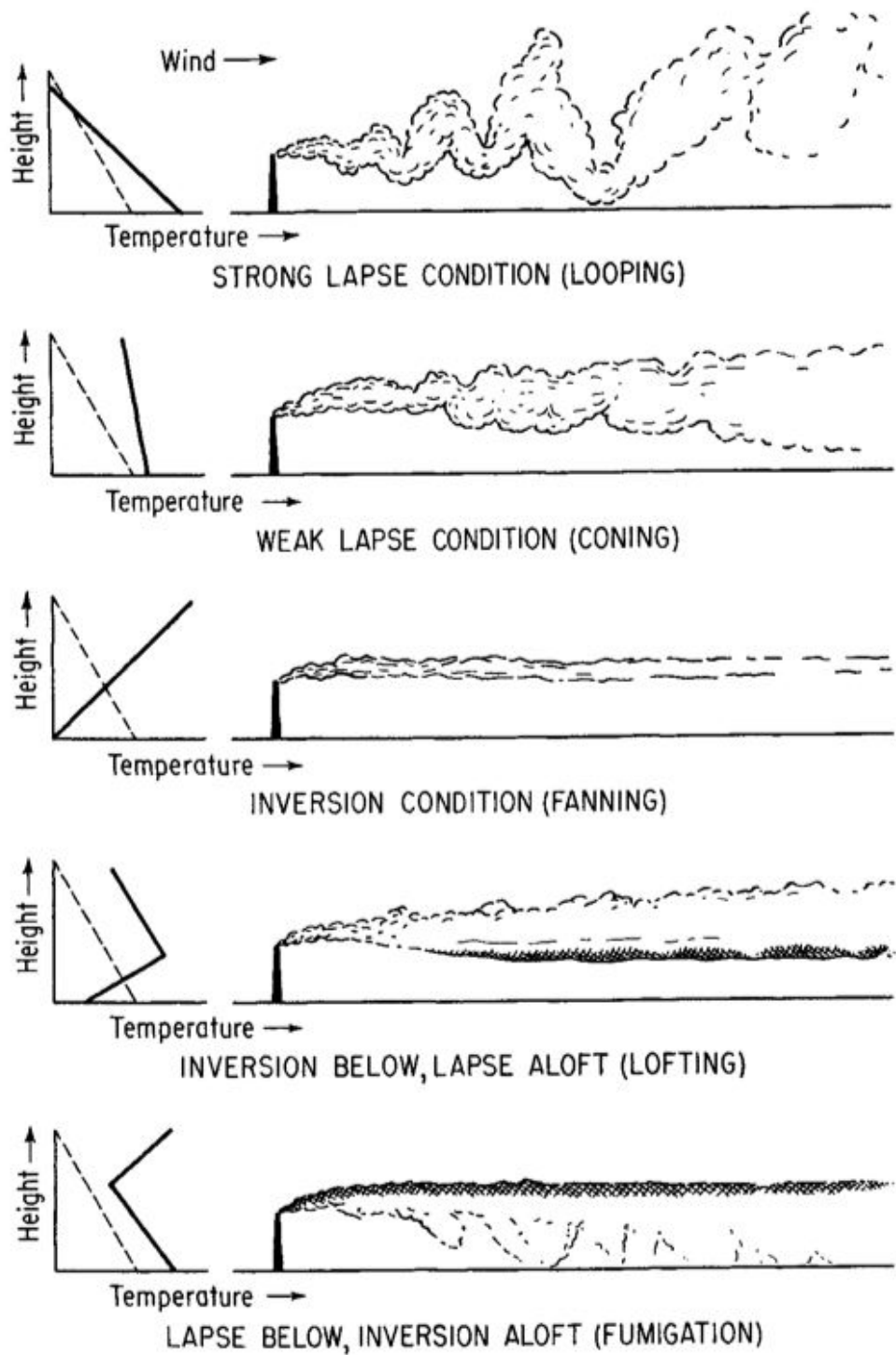
Figure 1.5: Schematic representation of stack-gas behavior under vairous conditions of vertical stability. Actual temperature (solid line) and dry adiabatic lapse rate (dashed line) are shown (Eisenbud and Gesell, 1997).

Thermal or Wind Erosion (Atmospheric Resuspension)

The rate of upward mass transfer of aerosols from a surface has been a sparsely measured quantity (Garger et al., 1997). Forces which resuspend particulates initially deposited upon a surface must overpower those of the friction or binding of the particle-surface chemistry. This is likely a prolonged process of agitating the surface particulate from different directions until it achieves lift-off; formally this has been summarized as the "rock-and-roll" scheme (Figure 1.6) (Caruso et al., 2015).
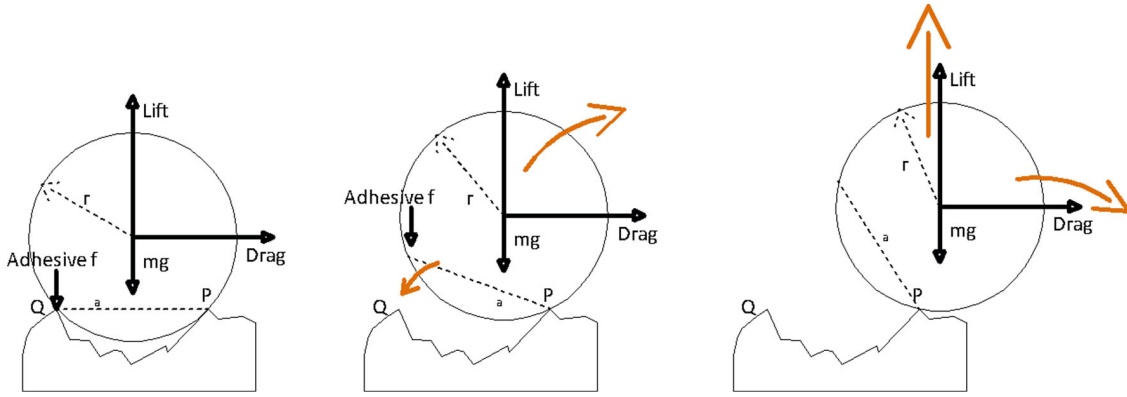
Figure 1.6: Schematic description of Rock n' Roll model

The resuspending force F_{RES} (μN) is considered the net upward force acting on each particle, with aerodynamic drag force $F_{R,d}$ and turbulent burst force $F_{R,b}$ pulling upward and gravitational force F_G, and adhesive particle cohesion force $F_{A,c}$ and friction force $F_{A,f}$ pulling downard (Eq. 1.11).

$$F_{RES} = F_{R,d} + F_{R,b} - (F_G + F_{A,c} + F_{A,f}) \tag{1.11}$$

This simple model of *quasi-static rock n' roll*, as opposed to its *dynamic* counterpart which considers resonant energy transfer to nearby particles, has been well implemented in a number of computer codes such as Melcor (Merrill and Humrickhouse, 2011). The resuspension rate Λ (s^{-1}) is defined as the as the ratio of surface concentration which achieves liftoff to that which does not per unit

time, an expression which gives rise to the resuspension flux Φ_r (kg m^{-2} s^{-1}, Eq. 1.12).

$$\Lambda = \frac{M/A}{M_0/A} \frac{1}{\Delta t} \qquad \longrightarrow \qquad \Phi_r = \frac{M/A}{\Delta t} = \Lambda \frac{M_0}{A} \qquad (1.12)$$

The results of the large-scale STORM experiment at the Ispra site of European Union's Joint Research Commission (Parozzi et al., 1998) have been used to construct an empirical functional form of Λ in terms of resuspending force F_{RES} (Eq. 1.13). The mass flow equation relates the mass flux (kg/s) flowing though through a cross-section to the kinetic fractional transfer of mass into the air (Eq. 1.14).

$$\Lambda = \begin{cases} 0.4037 \cdot F_{RES}^{0.6003}, & F_{RES} < 3.065 \times 10^{-4} \mu N \\ \\ 90.28 \cdot F_{RES}^{1.269}, & F_{RES} > 3.065 \times 10^{-4} \mu N \end{cases} \qquad (1.13)$$

$$\frac{dm_A}{dt} = \Phi_r A = \Lambda \frac{m_S}{A} A = \Lambda m_S \quad \therefore \quad \frac{dm_A}{dt} = k_{A \leftarrow S,RES} m_S \quad \longrightarrow \quad k_{A \leftarrow S,RES} = \Lambda \qquad (1.14)$$

The effective size of a particulate plays a great role in the fate of its location. Due to the competition of external atmospheric forces and internal coagulation forces, aerosols will typically exhibit a range of sizes.

The resuspended particle size distribution may undergo changes from that of the initial surface deposition (Anspaugh et al., 2002). Fine particulates have been found to make up a significant portion of resuspended material under light wind conditions (Chkhetiani et al., 2012), but coarse particulates increase in presence with lateral wind speed (Henry and Minier, 2014). A *roughness* surface rate constant can serve as the functional preference for particle size (Ziskind et al., 1995). The standard treatment is Gaussian potential barrier which is lowest at a preferred size r^*; the

deviation for a particle r_a will lower the rate constant as Eq. 1.15:

$$k_{A \leftarrow S,RES}(r_a) = k_{A \leftarrow S,RES,0} e^{-\frac{(r_a - r^*)^2}{r_0^2}}, \tag{1.15}$$

where r_0 characterizes the sensitivity of the deviation effect and k_0 is the maximum rate constant. In practice, k_0 is a function of surface layer wind speed which acoustically resonates with characteristic particle sizes.

Settling (Gravitational Deposition)

The deposition process of particulates may be modeled as a basic gravitational settling particles. Particulates will certainly possess unique chaotic surface structures, so the spherical equivalence is established through the *aerodynamic diameter*- that of a spherical particle falling at the same terminal velocity in the fluid (air). This terminal velocity, which accounts for buoancy (Eq. 1.16) is dependent upon the density of the particulate ρ_s, gravitational acceleration g, density of the fluid ρ, particle diameter d, and drag coefficient C_d; for spherical particles $C_d = 0.47$. This terminal velocity can be used to find the fractional rate of transfer for a column of particulates in the air that reach the surface (Eqs. 1.17, 1.18).

$$v_T = \sqrt{\frac{4gd}{3C_d}\left(\frac{\rho_s - \rho}{\rho}\right)} \tag{1.16}$$

$$\frac{dm_S}{dt} = \phi_g A = C v_T A = \frac{m_A}{V} v_T A = \frac{v_T A}{V} m_A = \frac{v_T}{h} m_A \tag{1.17}$$

$$\frac{dm_S}{dt} = k_{A \rightarrow S,GRAV} m_A \qquad \therefore \qquad k_{A \rightarrow S,GRAV} = \frac{v_T}{h} \tag{1.18}$$

This transfer rate depends only on the terminal velocity of the particulates in the fluid (air at some temperature at pressure), and the height of the naturally occuring column of airborne particulates.

19

This fractional transfer rate can be visualized as the fraction of the column which has dropped per second of time. If the naturally-occuring column small, the rate constant will be greater as particles do not on average have as far to travel.

Washout, Rainsplash, Filtration (Wet Deposition, Resuspension, Migration)

Non-meteorological processes which contribute to the availability of surface particulates for re-suspension can include colloidal migration channels to non-contaminated areas. Kinetic models for sorption and desorption of radionuclides to the surface binding sites at a boundary layer, and for colloid in the bulk ground matrix, have been employed successfully in both under- and over-saturated conditions (Lujaniene et al., 2012). Americium is readily absorbed into clays and organic mineral oxide topsoils (Bunzl et al., 1995; Lee and Lee, 2000). In colloidal form, Americium is strongly kinetic in granodiorite and infill (Mori et al., 2003; Vilks and Bachinski, 1996), but shows preference for anionic sorption in cementous pastes (Evans, 2008). It had significantly decreased mobility in the presence of snow drifts/melts compared alkali and alkaline earth metals (Chawla et al., 2010). Foliage in the region accumulates resuspended material proportionate to increased rainfall intensity and frequency (Dreicer et al., 1984).

Bioturbation (Anthropogenic or Biological Resurfacing or Resuspension)

In cases of a substrate made of soil, grass, or other organic material, burrowing organisms may also significantly contribute to radionuclide movement. Bioturbators actively mix bulk material through digging or ingestion (known as bioturbators). Earthworms have been found to overturn 1 meter of topsoil with a throughput of 5 to 10 years (Muller-Lemens and van Dorp, 1996). This type of movement is difficult to model as a kinetic process, but is well-described by a diffusive local mixing process; this approached enabled measurements of 1 to 2 cm year^{-1} biodiffusion mixing coefficient in both California (USA) grassland and Australian forests (Kaste et al., 2007; Matisoff et al., 2011). It was determined that greater biota activity in soils contributed to higher rates of observed erosion.

1.3 Detection of Radioactive Materials

1.3.1 Neutron Activation Analysis

The analysis of trace quantities of some radionuclides is achieved using neutron activation analysis, a proven technique for achieving optimal detection limits (Murarka, 2001). Figure 1.7 demonstrates the resulting nuclear states following successful absorption of a neutron (NMIII, 2012). *Prompt gamma activation analysis* (PGAA) is one modality for tracking radioactive decay events induced by neutron absorbtion which involves a detector immediately in proximity of the irradiation zone; detected *prompt* gammas occur upon nuclear transformation. In this study, the gammas are tracked with gamma spectroscopy which grants the flexibility of a simpler activation setup and the use of an external detector system.
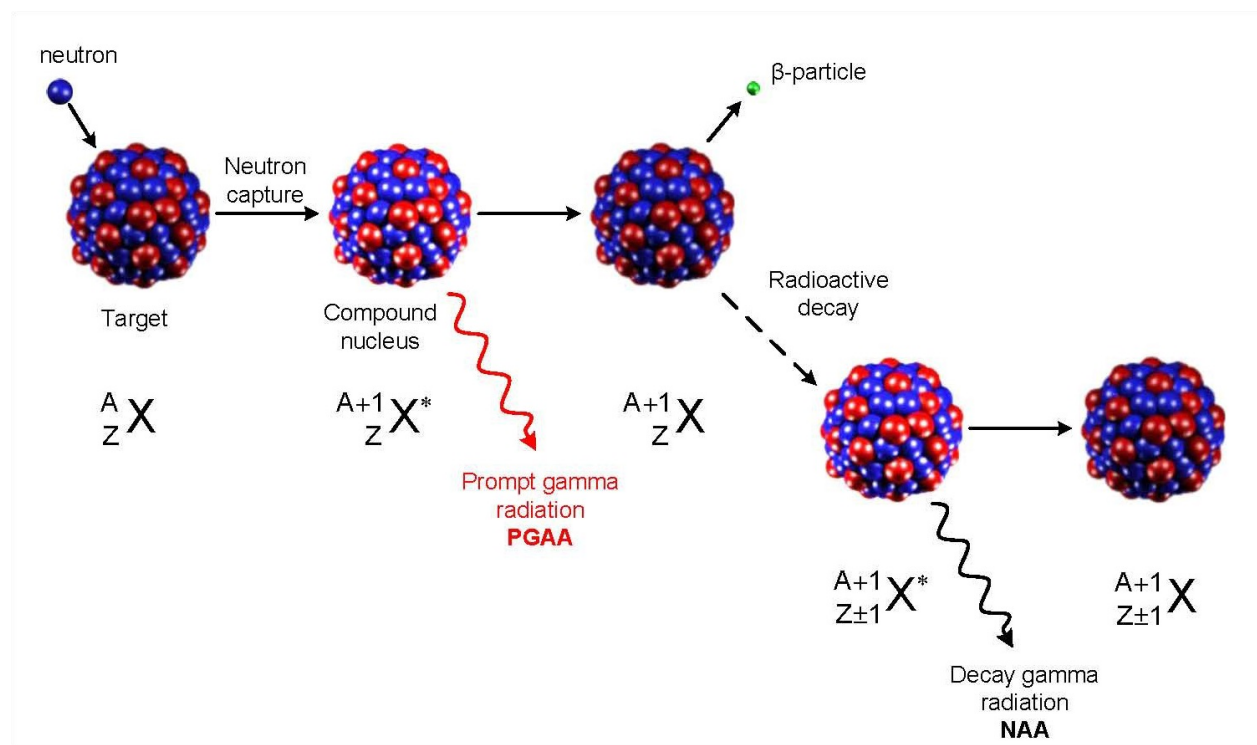
Figure 1.7: Schematic of neutron capture by some stable nuclide $^{A}_{Z}X$ and resulting decay and radiation pathway of the unstable nucleus.

Neutron Generator Beam Characterization

A deuterium-fusion accelerator neutron generator provides a spectrum of thermal to fast neutrons. The forward momentum of the isotropic fusion reaction produces a forward-facing cone of neutrons. Such an ideal projection of the isotropic flux would provide a consistently decreasing particle flow with radial distance from the center. A recent characterization of the DD110M neutron generator (Adelphi Technology, Inc.) at Worcester Polytechnic Institute (WPI) demonstrated that the neutron flux experiences variation in its spatial distribution due to a number of confounding factors, like lab room temperature and electrostatic buildup (Gardner and Crespi, 2015). A computer-generated profile of the beam based on an analysis of Gafchromic film is presented in Fig. 1.8.
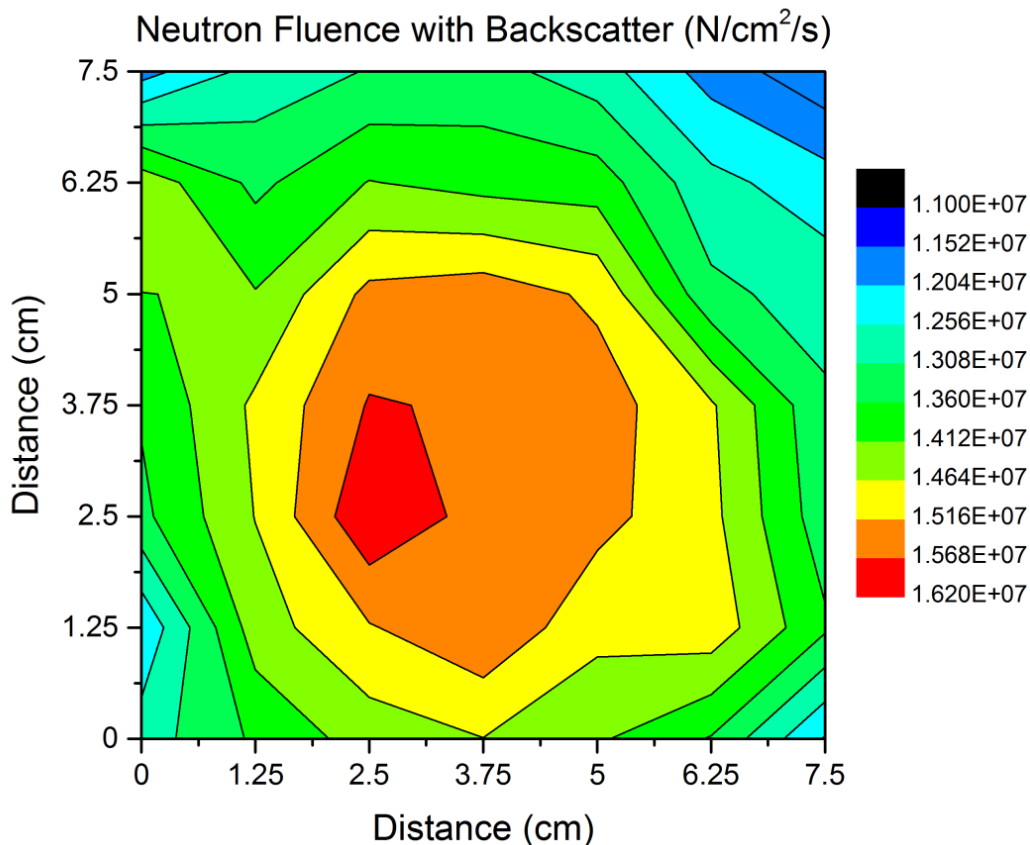
Figure 1.8: Fluence colormap of the WPI neutron generator exit beam profile (Gardner and Crespi, 2015).

1.3.2 Experimental Detection Characteristics

Minimum Detectable Activity (MDA)

The following uses similar notation and derivation as (Currie, 1968), where a background count for time t_b yields $\mu_b \pm \sigma_b$, and a gross count (sample + background) for time t_g yields $\mu_g \pm \sigma_g$. The net signal is therefore $\mu_s \pm \sigma_s$ where

$$\mu_s = \mu_g - \mu_b, \quad \text{and} \quad \sigma_s = \sqrt{\sigma_g^2 + \sigma_b^2}. \tag{1.19}$$

To begin, we present the null hypothesis which supposes a zero count-rate of radioactivity from the sample (Eq. 1.20),

$$H_0: \quad \mu_s = 0. \tag{1.20}$$

There is a *critical limit* L_C beyond which the gross count rate disqualifies the null hypothesis. This is determined by the limiting probability of making a Type I error (false positive), 1-α. This can be expressed as a multiple of the gross count standard deviation (Eq. 1.21), from which the cumulative probability is α.

$$L_C = k_\alpha \sigma_0, \quad \text{where } k_\alpha = k_\alpha(p) \tag{1.21}$$

That is, one may *reject* H_0 with 1-α confidence when a gross count rate of $\mu_g = \mu_b + k_\alpha \sigma_0$ is measured. Expanding the terms with Gaussian statistics assuming the same counting time for both background and gross counts, we have (Eq. 1.22):

$$L_C = k_\alpha \sigma_0 = k_\alpha \sqrt{\sigma_g^2 + \sigma_b^2} = k_\alpha \sqrt{\cancel{\mu_s} + \mu_b + \mu_b} = k_\alpha \sqrt{2\mu_b} \tag{1.22}$$

Acceptance of H_0 at this limit leads to a likely Type II error (false negative) when there *is* radioactivity present; this motivates a *detection limit* L_D above L_C constructed in a similar manner. Considering the hypothesis that there *is* radioactivity present (Eq. 1.23), the detection limit is

given by

$$H: \quad \mu_s = L_D, \qquad L_D = L_C + k_\beta \sigma_D = L_C + k_\beta \sqrt{\sigma_s^2 + \sigma_0^2} = L_C + k_\beta \sqrt{L_D + \sigma_0^2}. \qquad (1.23)$$

Combining Eqs. 1.21 and 1.23, L_D is expressed as (Eq. 1.24)

$$L_D = L_C + \frac{k_\beta^2}{2} \left[1 + \sqrt{1 + \frac{4L_C}{k_\beta^2} + \frac{4L_C^2}{k_\alpha^2 k_\beta^2}} \right]. \qquad (1.24)$$

If $k_\alpha = k_\beta = k$, such as the area pertaining to a 95% confidence interval ($k(p = 0.05) = 1.645$), Eq. 1.24 reduces to (Eq. 1.25)

$$L_D = k^2 + 2L_C = k^2 + 2k\sqrt{2\mu_b}. \qquad (1.25)$$

The detection limits as constructed in Eqs. 1.24 and 1.25 are known as *minimum detectable true activity* (MDA). The detector receives a fraction of the counts of a source over time given by the detector efficiency ϵ (Eq. 1.26).

$$MDA = \frac{L_D}{\epsilon \Delta t} = \frac{k^2 + 2k\sqrt{2\mu_b}}{\epsilon \Delta t}. \qquad (1.26)$$

Minimum Detectable Mass (MDM)

Following now a similar approach to that of Currie, this value can relate to the *minimum detectable mass* (MDM) of a neutron-activated source by accounting for the *production rate* $P(\sigma)$ (Bq g^{-1}) and *saturation* of the sample $S(\lambda, \tau)$, and the *time synchronization* of irradiation τ, delay t, and

count Δt, $T(\lambda, t, \Delta t)$ (Eq. 1.27):

$$MDM = \frac{L_D}{\epsilon Y P(\sigma) S(\lambda, \tau) T(\lambda, t, \Delta t)}, \quad \text{where} \tag{1.27}$$

$$T(\lambda, t, \Delta t) = \left(\frac{e^{-\lambda t}}{\lambda}\right)\left(1 - e^{-\lambda \Delta t}\right),$$

$$S(\lambda, \tau) = 1 - e^{-\lambda \tau}, \quad \text{and}$$

$$P(\sigma) = \frac{N \sigma \phi}{m}.$$

Here λ (s^{-1}) is the decay constant, Y is the gamma yield for the radioactive decay, m (g) is the mass of the sample, and ϕ $(\text{n cm}^{-2} \text{ s}^{-1})$ is the neutron flux. N indicates the quantity of activation product produced; this will be the same value as for both the number of parent nuclides activated.

$$^{A}_{Z}X + n \rightarrow ^{A+1}_{Z} ZX \tag{1.28}$$

This quantity is obtained through atomic weights and relative isotope abundances (Eq. 1.29):

$$m = \sum \frac{M_{X_i} N_{X_i}}{N_A} = \frac{N_{X_*}}{N_A} \left(M_{X_*} + \sum_{i \neq *} \frac{M_{X_i} a_{X_i}}{a_{X_*}}\right) \tag{1.29}$$

$$\therefore \quad N = N_{X_*} = \frac{m N_A}{\left(M_{X_*} + \sum_{i \neq *} \frac{M_{X_i} a_{X_i}}{a_{X_*}}\right)}$$

The production rate for this reaction may then be written as Eq. 1.30:

$$P(\sigma) = \frac{N_A \sigma \phi}{\left(M_{X_*} + \sum_{i \neq *} \frac{M_{X_i} a_{X_i}}{a_{X_*}}\right)} \tag{1.30}$$

The complete expression for the minimum detectable mass is therefore (Eq. 1.31):

$$MDM = \frac{L_D \left(M_{X_*} + \sum_{i \neq *} \frac{M_{X_i} a_{X_i}}{a_{X_*}} \right)}{\epsilon Y N_A \sigma \phi \left(1 - e^{-\lambda \tau} \right) \left(\frac{e^{-\lambda t}}{\lambda} \right) \left(1 - e^{-\lambda \Delta t} \right)} \tag{1.31}$$

Minimum Detectable Resuspension Factor (MDS$_f$)

The MDM which is collected through the air sampler corresponds to a particulate resuspension factor (S_f) measured within the chamber over the course of the sampling period (t_s). An average resuspension factor ($\bar{S}_f$) can be presumed if the concentration is expected not substantially change over the time phase, which is obtainable in indoor measurements. A time-weighted resuspension factor would be a more preferable expression of observations, but requires simultaneous monitoring of the depositing mechanism.

The minimum detectable (average) resuspension factor (MDS$_f$, Eq. 1.32) is the ratio of the minimum detectable mass of the isotope of interest through the available limits of neutron activation analysis and air sampling concentration C_V (g m^{-3}) and the initial areal deposit of the isotope mass C_S (g m^{-2}). Also factored into this ratio is the limiting efficiency of the filter used for sampling, ϵ_F. The volume of air sampled is directly proportional to the flow rate f and sampling period t_s. The initial quantity of the compound dispersed is m_0, and the fractional molecular mass of the isotope of interest to that of the particulate compound is X_F.

$$MDS_f = \frac{C_V}{C_S} = \frac{\frac{MDM}{\epsilon_F V}}{\frac{m_0^*}{A}} = \frac{\frac{MDM}{\epsilon_F f t_s}}{\frac{m_0 X_F}{A}} = \frac{MDM \times A}{\epsilon_F m_0 X_F f t_s} \tag{1.32}$$

$$= \frac{A \left(k^2 + 2k\sqrt{2\mu_b} \right) \left(M_{X_*} + \sum_{i \neq *} \frac{M_{X_i} a_{X_i}}{a_{X_*}} \right)}{\epsilon_F Y m_0 X_F f t_s \epsilon N_A \sigma \phi \left(1 - e^{-\lambda \tau} \right) \left(\frac{e^{-\lambda t}}{\lambda} \right) \left(1 - e^{-\lambda \Delta t} \right)}$$

Neutron Flux Calibration

The neutron flux ϕ used in the neutron activation analysis may vary slightly between beam usages. To find this for each irradiation interval, a small foil with a known mass m_Q, molar mass M_Q, neutron absorbtion cross-section σ_Q, resulting reaction decay constant λ_Q, and gamma yield Y_Q will produce a number of counts C^Q when irradiated. Substituting respective values into in Eq. 1.27, the neutron flux which produces C^Q can be found (Eq. 1.33).

$$m_Q = \frac{C^Q}{\epsilon Y_Q P(\sigma_Q) S(\lambda_Q, \tau) T(\lambda_Q, t, \Delta t)}, \quad \text{where}$$

$$T(\lambda_Q, t, \Delta t) = \left(\frac{e^{-\lambda_Q t}}{\lambda_Q}\right)\left(1 - e^{-\lambda_Q \Delta t}\right),$$

$$S(\lambda_Q, \tau) = 1 - e^{-\lambda_Q \tau}, \quad \text{and}$$

$$P(\sigma_Q) = \frac{N_Q \sigma_Q \phi}{m_Q} = \frac{\left(\frac{m_Q N_A}{M_Q}\right)\sigma_Q \phi}{m_Q} = \frac{N_A \sigma_Q \phi}{M_Q}, \quad \text{so}$$

$$\phi = \frac{C^Q M_Q}{\epsilon Y_Q m_Q N_A \sigma_Q \left(1 - e^{-\lambda_Q \tau}\right)\left(\frac{e^{-\lambda_Q t}}{\lambda_Q}\right)\left(1 - e^{-\lambda_Q \Delta t}\right)} \tag{1.33}$$

1.4 Compartment Modeling of Particle Transfer

Compartment models are widely used in predicting radioisotope quantities in organs through so-called *biokinetic models* (ICRP, 1994; ICRP, 1997). The models assume that each measurable location of particles in the body constitutes a well-defined compartmentalized volume, and that the rates of transfer of particles from each connecting compartment is directly proportional to the quantity in the compartment. When particles can travel back and forth between consecutive compartments, the kinetics are called *recycling*. Explicit solutions for recycling compartment models (*forward problem*) can become very difficult to derive. However, when an explicit model is found, it can provide a means of working backwards (*inverse problem*) to determine the rate coefficient for a given measurement of impulse of conditions (Sanchez and Lopez-Fidalgo, 2003).

A compartment is *identifiable*, that is it can be calculated for and assigned to a particular system based on time-intervals of compartment measurements under certain conditions (Vicini et al., 2000). These conditions are related to the total input and output based on the compartment diagrams (Fig. 1.9). For the catenary compartment system, these conditions are listed in Eq. 1.34. In general, when there are more parameters than the system has unique equations of relation, the parameters may be determined if one or more are initially known and set as constants.
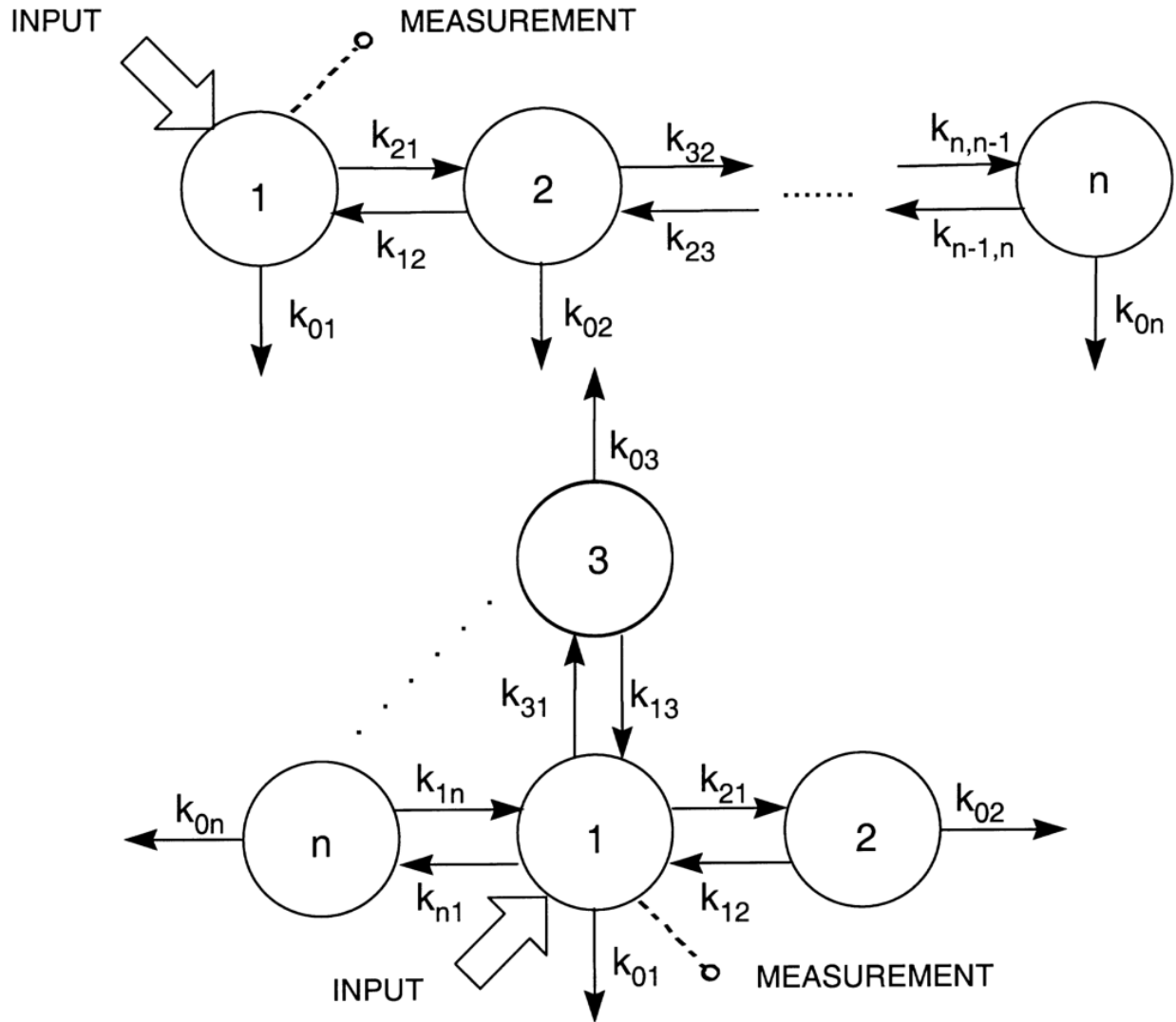
Figure 1.9: General catenary (upper) and mammillary (lower) compartmental models with both input and output in compartment 1 (Vicini et al., 2000).

$$
\begin{aligned}
-k_1 &= k_{01} + k_{21} \\
-k_i &= k_{0i} + k_{i-1,i} + k_{i+1,i} \\
-k_n &= k_{0n} + k_{n-1,n} \\
\gamma_i &= k_{i-1}k_{i,i-1}, \quad i = 2, 3, \ldots, n
\end{aligned}
\tag{1.34}
$$

29

The concentration of a dispersion of particulates in the atmosphere can be quantified using an air sampling setup. Particles are generally quantified by specific nuclide or by gross alpha or beta count for radionuclides. In the case of the former, particulates are collected for further radiochemical analysis, but in the latter the sampler system is often directly conected to radiation detector. Collection can be performed with disposible filters with pore-size comparable to the sample particle size, or with cascade impactors which separate particles by diameter in stages.

1.4.1 Compartment Modeling of Air Sampling

The transfer of isotopes onto an air filter is modeled with a compartment model in Eq. 1.35. The rate of transfer is proportional to the current air concentration concentration (Eq. 1.36). This leads to an equation of exponential decrease in the fractional quantity X_A remaining in the air compartment with its complement then found on the filter (Eq. 1.37). The simplified form of the fractional quantity provides a means to calibrate the removal rate $k_{A\rightarrow}$ for a given air sampling result (Eq. 1.38).

$$\boxed{\text{Filter,} \quad X_F(t)}$$
$$\uparrow k_{A\rightarrow} \tag{1.35}$$
$$\boxed{\text{Air,} \quad X_A(t)}$$

$$\begin{aligned} \dot{X}_F &= k_{A\rightarrow}X_A \\ \dot{X}_A &= -k_{A\rightarrow}X_A \end{aligned}, \qquad X_A(t=0)=1, \quad X_F(t=0)=0 \tag{1.36}$$

$$X_A(t) = e^{-k_{A\rightarrow}t} \qquad \longrightarrow \qquad X_F = \int_0^{t_s} k_{A\rightarrow}e^{-k_{A\rightarrow}t}dt = 1 - e^{-k_{A\rightarrow}t_s} \tag{1.37}$$

$$k_{A\rightarrow} = \frac{1}{t_s}\ln\left(\frac{1}{1-X_F}\right) = \frac{1}{t_s}\ln\left(\frac{1}{1-\frac{m}{m_0}}\right) \tag{1.38}$$

As is generally the case, if the air sampler does not appreciably remove mass from the air, the air concentration can be considered constant. Then, the mass of isotopes collected on a filter is proportional to the mass flux provided by the ambient concentration (Eq. 1.39). This measurement is often taken by measuring a concentration C with a sampler flow rate F and filter efficiency ϵ_f (NRC, 2011), which provides a second avenue for calibrating the rate constant (Eq. 1.40).

$$\dot{X}_F = k_{A\rightarrow} \qquad \longrightarrow \qquad X_F = k_{A\rightarrow}t_s \qquad \longrightarrow \qquad m = m_0 k_{A\rightarrow}t_s \tag{1.39}$$

$$m = CV\epsilon_f = CF\epsilon_f t_s \qquad \longrightarrow \qquad k_{A\rightarrow} = \frac{CF\epsilon_f}{m_0} \tag{1.40}$$

For a radioactive air sample, the collected activity decays during both the sampling time and any delay previous to analysis. The activity A follows with a sampling with flow rate F for time t_s of some mass concentration C, specific activity A_m, and delay time t_d (Eq. 1.41; NRC, 2011).

$$A = \frac{A_m C F \epsilon_f}{\lambda} \left(1 - e^{-\lambda t_s} \right) e^{-\lambda t_d} \tag{1.41}$$

1.4.2 Proportionate Air Sampling

Depending upon the flow rate of the air sampler, the system may "oversample" or "undersample" the particle concentration. At sampler flow rates greater than the thermal velocity of the medium, the sampler will collect an unrepresentatively large amount of mass for the siphoned volume. Similarly, when the sampler flow rate lags behind thermal air speed, the filter will collect less mass than the concentration would normally deposit for the sampled volume. This is illustrated in the sketches in Figure 1.10 (Supriya, 2016).

EXPLANATION

$\overline{V}$ AMBIENT STREAM VELOCITY

V_n VELOCITY INTO THE SAMPLER NOZZLE

$\overline{C}$ SEDIMENT CONCENTRATION IN THE STREAM

C_s SAMPLE SEDIMENT CONCENTRATION
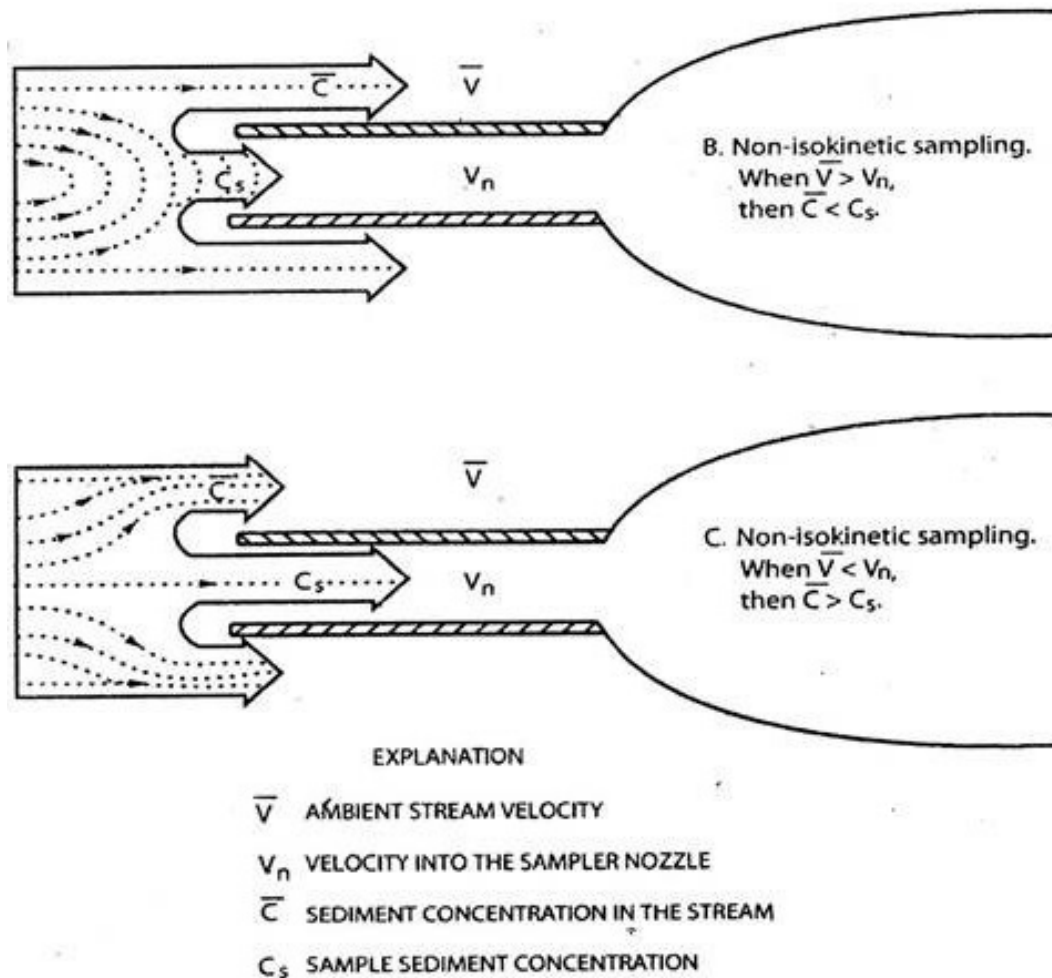
Figure 1.10: Schematic of air sampler "over-" and "undersampling" a sediment concentration in a stream.

Chapter 2

Methodology

2.1 Resuspension Factor Model Assessment of Historical Data

The historic dataset of resuspension factors are modeled using a compartmental system to provide an theoretical foundation for the resuspension rate constant. The semi-empirical approach is incidentally related to a closed, three-compartment model which establishes an equlibrium constant term. In this method, the air sampling compartment model is expanded to include additional transfer terms and measurable compartments.

2.1.1 Historic Dataset Binning

The resuspension factor measurements from the Nevada Test Site, Chernobyl-threatened regions, and other artificial release scenarios provide a thorough foundation in measurements from which to base catenary models. The trend is best illustrated with the sampling taken by Maxwell and Anspaugh (Figure 2.1). The data follow a heteroscedastic trend, in that the variance appears to change as a function of time, almost exponentially.
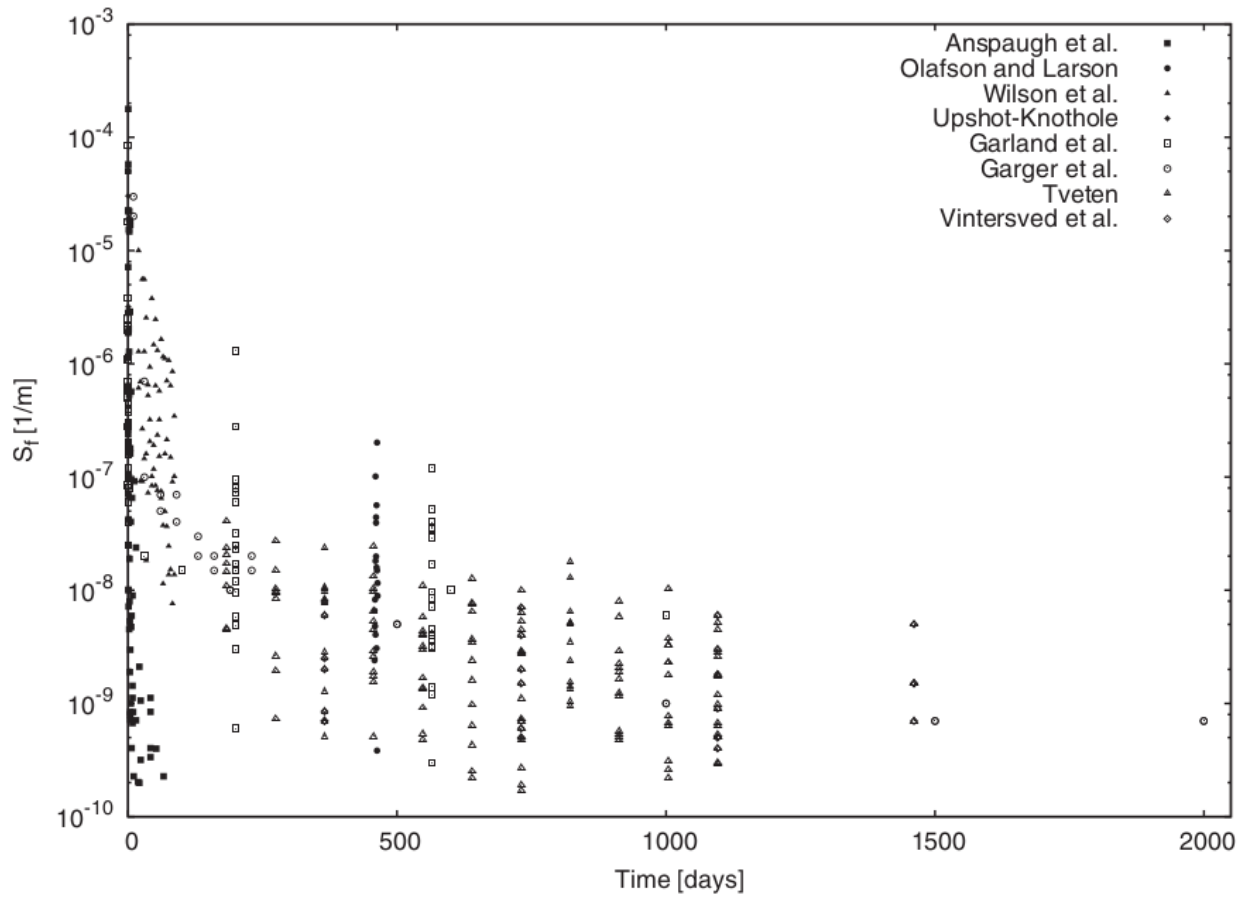
Figure 2.1: Sampling of historic dataset of resuspension factors analyzed by Maxwell and Anspaugh (2011).

2.1.2 Weighted Curve Fitting

Measurements made in the historic resuspension factor data sets were made at regular intervals post deposition, particularly daily and weekly. Therefore, a roughly 3 day bin size was used (based on available data) to discretize data. Within each bin, the geometric average (Eq. 2.1) and standard deviation (Eq. 2.2) are determined. The averages are then fit to a catenary model using a linear least-squares regression. The importance of each bin's average resuspension factor is weighted by the uncertainty in the bin's distribution $\left(W_i = \sigma_{S_{f_i}}^{-2} \right)$. This then has the effect of increasing the importance of low-uncertainty coincidence present in the long-term data, as well as decreasing the importance of high-uncertainty coincidence present in the short-term data.

$$\mu_{S_f} = e^{\frac{1}{n} \sum^n \ln(S_f)} \tag{2.1}$$

$$\sigma_{S_f} = e^{\sqrt{\frac{1}{n} \sum^n \left(\ln(S_f) - \mu_{S_f} \right)^2}} \tag{2.2}$$

To serve as a control analysis with the previous assessment, the offset double-exponential equation is initial used. The advantage of this model is the outcome of the same semiempirical equation used, but this model does not factor in the lateral transport of particulates and further assumes that the total amount is locally conserved. This is exemplified to the presence of an offset term, a constant which persists after the exponentials have decayed. The catenary model was applied both with fixed traditional 10^{-9} and unfixed variable offset constant to test if the offset term can contribute to a better fit. These procedures are outlined in greater detail in the author's publication in the Health Physics journal (Marshall et al., 2018).

2.2 Catenary Kinetic Models

By compartmentalizing local measurable concentrations of contaminants, a kinetic model of mass transport can be constructed. Compartments linked in a chain with only forward and backward pathways are called *catenary* systems, as opposed to the *mammalian* systems of side chains and dead-ends, named after their primary application in medicinal chemistry. The following sections describe analytical solutions to a catenary model of the outdoor environment. Equations in these derivations will be expressed in terms of dimensionless fractions X which readily applies to systems where total mass is known.

2.2.1 Open and Closed Catenary Systems

The catenary (chain) model features compartments which connect to either one or two neighbors in a linear fashion (Eq. 2.3). Each ith compartment exchanges particulates with the previous and next compartments with positive rate constants k_{-i} and k_i respectively. The kinetic equations to this model for N compartments are given by (Eq. 2.4).

$$
\begin{array}{ccc}
& \vdots & \\
k_{-(i-1)} & \uparrow\downarrow & k_{i-1} \\
& \boxed{X_{i-1}} & \\
k_{-i} & \uparrow\downarrow & k_i \\
& \boxed{X_i} & \\
k_{-(i+1)} & \uparrow\downarrow & k_{(i+1)} \\
& \boxed{X_{i+1}} & \\
& \vdots &
\end{array}
\tag{2.3}
$$
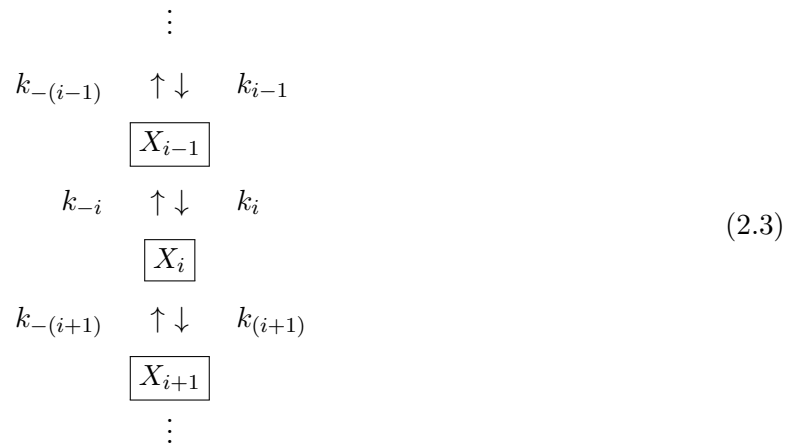
$$\dot{\vec{X}} = \mathcal{K}\vec{X}, \qquad \text{where } \mathcal{K} \text{ is} \tag{2.4}$$

$$\begin{pmatrix} -k_{-1} & k_1 & 0 & \dots & & 0 \\ k_{-1} & -k_1 - k_{-2} & k_2 & & & \vdots \\ 0 & & \ddots & k_{N-1} & & 0 \\ \vdots & & k_{-(N-2)} & -k_{N-2} - k_{-(N-1)} & k_{N-1} \\ 0 & \dots & 0 & k_{-(N-1)} & & -k_{N-1} \end{pmatrix}.$$

Rate constants for unconserved sources and sinks for *open* systems may be appended to the diagonal elements of this otherwise *closed* system. To solve this first order system, the eigenvalue problem arising from the ansatz (Eq. 2.5) must be satisfied.

$$\vec{X} = C\vec{\nu}e^{\omega t} \quad \text{where} \;\; \omega \;\; s.t. \;\; \det |\mathcal{K} - \omega \mathcal{I}| = 0 \tag{2.5}$$

This determinant has no closed-form expression, but nonetheless generates the characteristic polynomial to supply N eigenvalues ω. The closed system will always produce $\omega = 0$, a constant term corresponding to the quasi-static equilibrium values of each compartment. A single source or sink will collapse the equilibrium constant into the final N^{th} exponential term. Eigenvectors $\vec{\nu}$ are obtained (Eq. 2.6) to orthogonalize the terms. The unique solution is a superposition of these eigenfunctions, found by determining normalization coefficients C_j from initial conditions (Eq. 2.7).

$$(\mathcal{K} - \omega \mathcal{I})\,\vec{\nu} = 0 \quad \forall \; \omega \tag{2.6}$$

$$\vec{X}(t = 0) = (X_1(0), X_2(0), \dots, X_N(0))^\dagger = \sum_j^N C_j \vec{\nu_j}$$

$$\therefore \quad \vec{X}(t) = \sum_j^N C_j \vec{\nu_j} e^{\omega_j t} = \sum_j^N \vec{X_j} e^{\omega_j t} \tag{2.7}$$

38

In the remaining sections, compartments are defined for airborne (A), surface-bound (S), and ground colloidal bulk-matrix (G) forms of the particulates. Kinetic rate constants are laid out in Table 2.1 which may encompass the mechanisms of multiple environmental influences introduced in the previous chapter.

Table 2.1: Transport mechanisms for catenary model system micro-rate constants

Rate constant (s^{-1})	Transport	Mechanisms
$k_{A\rightarrow}$	Migration	wind erosion
$k_{A\rightarrow S}$	Deposition	settling, washout
$k_{A\leftarrow S}$	Resuspension	thermal/wind erosion, rainsplash, bioturbation
$k_{S\rightarrow G}$	Removal	filtration, bioaccumulation
$k_{S\leftarrow G}$	Resurfacing	bioturbation

2.2.2 Model Rate Equations

Closed Two-Compartment Model

$$\boxed{\text{Air (A)}, \quad X_A(t)}$$
$$k_{A\leftarrow S} \quad \uparrow\downarrow \quad k_{A\rightarrow S} \tag{2.8}$$
$$\boxed{\text{Surface (S)}, \quad X_S(t)}$$

This small system (Eq. 2.8) for mass transport is effective when there are no external forces involved. For an indoor air sampling setup, the transport mechanism for resuspension is possibly driven virtually entirely by the sampler. Beyond this, the particles are otherwise gravitationally settling. In an indoor or outdoor scenario, wind may well be a factor but no substantial loss latterally to dispersion or air sampling occurs, sufficient for a large enough measurement area in a short enough period of time.

The continuity differential equations for this system (Eq. 2.9) and initial conditions (Eq. 2.10) form an initial-value problem for which there is a unique solution.

$$\dot{X}_A = -k_{A\rightarrow S}X_A + k_{A\leftarrow S}X_S$$
$$\dot{X}_S = k_{A\rightarrow S}X_A - k_{A\leftarrow S}X_S \tag{2.9}$$

$$X_A(t=0) = X_A(0), \quad X_S(t=0) = X_S(0) = 1 - X_A(0) \tag{2.10}$$

The characteristic equation of the macro-rate constants ω_i with respect to the micro rate constants k_j for this system is given by Eq. 2.11. The fit coefficients for the unique solution (Eq. 2.12) are parameterized in Table 3.11. This system can then be inverted to provide a solution for the parameters in terms of the fit coefficients in Table 3.16.

$$\omega^2 + (k_{A\leftarrow S} + k_{A\rightarrow S})\omega - k_{A\leftarrow S}k_{A\rightarrow S} = 0 \tag{2.11}$$

$$X_A(t) = X_1 + X_2 e^{\omega_2 t} \tag{2.12}$$

Open Two-Compartment Model

$$\uparrow k_{A\rightarrow}$$

$$\boxed{\text{Air (A)}, \quad X_A(t)}$$

$$k_{A\leftarrow S} \quad \uparrow\downarrow \quad k_{A\rightarrow S}$$

$$\boxed{\text{Surface (S)}, \quad X_S(t)} \qquad (2.13)$$

This small system (Eq. 2.13) for mass transport is effective when there is are few forces involved. For an indoor air sampling setup, the transport mechanisms are limited to thermal resuspension including the effect of the air sampler, gravitational settling, and bioturbation of the experimental procedure. In an outdoor scenario, wind may be included as with washout, but may not adequately account for the semi-permanent loss of particulate filtering into porous media.

The continuity differential equations for this system (Eq. 2.14) and initial conditions (Eq. 2.15) form an initial-value problem for which there is a unique solution.

$$
\begin{aligned}
\dot{X}_A &= -(k_{A\rightarrow} + k_{A\rightarrow S})X_A \;+\; k_{A\leftarrow S}X_S \\
\dot{X}_S &= \phantom{-(k_{A\rightarrow} +)} k_{A\rightarrow S}X_A \;-\; k_{A\leftarrow S}X_S
\end{aligned}
\qquad (2.14)
$$

$$X_A(t=0) = X_A(0), \quad X_S(t=0) = X_S(0) = 1 - X_A(0) \qquad (2.15)$$

The characteristic equation of the macro-rate constants ω_i with respect to the micro rate constants k_j for this system is given by Eq. 2.16. The fit coefficients for the unique solution (Eq. 2.17) are parameterized in Table 3.12. This system can then be inverted to provide a solution for the parameters in terms of the fit coefficients in Table 3.17.

$$\omega^2 + (k_{A\leftarrow S} + k_{A\rightarrow S})\omega - k_{A\leftarrow S}k_{A\rightarrow S} = 0 \qquad (2.16)$$

$$X_A(t) = X_1 e^{\omega_1 t} + X_2 e^{\omega_2 t} \qquad (2.17)$$

Closed Three-Compartment Model

$$\boxed{\text{Air (A)}, \quad X_A(t)}$$

$$k_{A\leftarrow S} \quad \uparrow\downarrow \quad k_{A\rightarrow S}$$

$$\boxed{\text{Surface (S)}, \quad X_S(t)} \tag{2.18}$$

$$k_{S\leftarrow G} \quad \uparrow\downarrow \quad k_{S\rightarrow G}$$

$$\boxed{\text{Ground (G)}, \quad X_G(t)}$$

This system (Eq. 2.18) for mass transport is useful when there is a considerable loss of particulates to sinks around the surface or ground. Compared to the open two-compartment model, it accounts for filtration and bioturbation. The implicit assumption of a constant total mass in the system suggests this model may be productive in conjunction with another model which assesses lateral transport of particulates, such as with an atmospheric dispersion models. It is also an approximate condition when the filtration occurs on a timescale much larger than the available dataset of observations. The continuity differential equations for this system (Eq. 2.19) and initial conditions (Eq. 2.20) form an initial-value problem for which there is a unique solution.

$$
\begin{aligned}
\dot{X}_A &= -k_{A\rightarrow S}X_A \;+\; & k_{A\leftarrow S}X_S & \\
\dot{X}_S &= \;k_{A\rightarrow S}X_A \;-\; (k_{A\leftarrow S}+k_{S\rightarrow G})X_S \;+\; & k_{S\leftarrow G}X_G & \\
\dot{X}_G &= \;+\; & k_{S\rightarrow G}X_S \;-\; k_{S\rightarrow G}X_G &
\end{aligned}
\tag{2.19}
$$

$$X_A(t=0)=X_A(0), \quad X_S(t=0)=X_S(0)=1-X_A(0), \quad X_G(t=0)=0 \tag{2.20}$$

The characteristic equation of the macro-rate constants ω_i with respect to the micro rate constants k_j for this system, and unique solution in terms of fit parameters are given in (Eq. 2.21).

$$\omega^2 + (k_{A\leftarrow S}+k_{A\rightarrow S})\omega - k_{A\leftarrow S}k_{A\rightarrow S}=0 \qquad X_A(t)=X_1+X_2 e^{\omega_2 t}+X_3 e^{\omega_3 t} \tag{2.21}$$

Alternative Closed Three-Compartment Model

$$
\boxed{\text{Filter (F)}, \quad X_F(t)}
$$

$$
\uparrow k_{A\rightarrow}
$$

$$
\boxed{\text{Air (A)}, \quad X_A(t)} \tag{2.22}
$$

$$
k_{A\leftarrow S} \quad \uparrow\downarrow \quad k_{A\rightarrow S}
$$

$$
\boxed{\text{Surface (S)}, \quad X_S(t)}
$$

This system (Eq. 2.22) for mass transport is useful when there is a considerable loss of particulates to the air filter. Compared to the open two-compartment model, it provides an equilibraition point between the filter, air, surface. The implicit assumption of a constant total mass in the system suggests this model may productive in conjunction with another model which assesses lateral transport of particulates, such as with an atmospheric dispersion models. It is also an approximate condition when the filtration occurs on a timescale much larger than the available dataset of observations. The continuity differential equations for this system (Eq. 2.23) and initial conditions (Eq. 2.24) form an initial-value problem for which there is a unique solution.

$$
\begin{aligned}
\dot{X}_F &= -k_{A\rightarrow}X_A \\
\dot{X}_A &= k_{A\rightarrow S}X_A - (k_{A\leftarrow S} + k_{S\rightarrow G})X_S \\
\dot{X}_S &= k_{A\rightarrow S}X_A - k_{A\rightarrow S}X_S
\end{aligned} \tag{2.23}
$$

$$
X_F(t=0) = 0, \quad X_A(t=0) = X_A(0), \quad X_S(t=0) = X_S(0) = 1 - X_A(0) \tag{2.24}
$$

The characteristic equation of the macro-rate constants ω_i with respect to the micro rate constants k_j for this system, and unique solution in terms of fit parameters are given in (Eq. 2.26).

$$
\omega^2 + (k_{A\leftarrow S} + k_{A\rightarrow S})\omega - k_{A\leftarrow S}k_{A\rightarrow S} = 0 \tag{2.25}
$$

$$
X_F(t) = X_1 + X_2 e^{\omega_2 t} + X_3 e^{\omega_3 t} \tag{2.26}
$$

Open Three-Compartment Model

$$\uparrow k_{A\to}$$

$$\boxed{\text{Air (A)}, \quad X_A(t)}$$

$$k_{A\leftarrow S} \quad \uparrow\downarrow \quad k_{A\to S}$$

$$\boxed{\text{Surface (S)}, \quad X_S(t)}$$

$$k_{S\leftarrow G} \quad \uparrow\downarrow \quad k_{S\to G}$$

$$\boxed{\text{Ground (G)}, \quad X_G(t)} \tag{2.27}$$
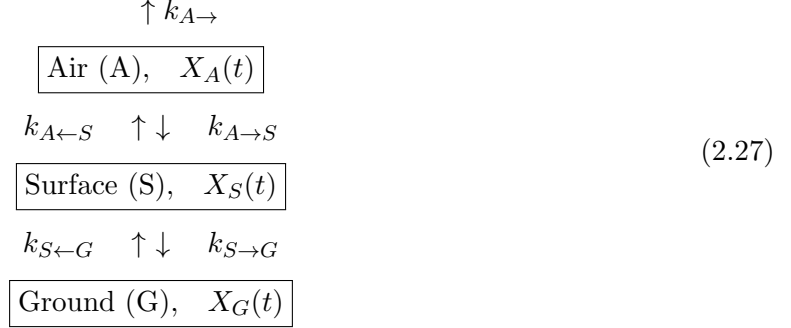
This system (Eq. 2.27) for mass transport is more useful when there a large number of transport influences contained in the observation sample set. It may include all mechanisms described in the previous chapter, as well as any others which have yet to be determined. Beyond this, larger systems will become arduous to analytically solve and are best left to numerical solvers.

The continuity differential equations for this system (Eq. 2.28) and initial conditions (Eq. 2.29) form an initial-value problem for which there is a unique solution.

$$
\begin{aligned}
\dot{X}_A &= -(k_{A\to} + k_{A\to S})X_A \;+\; & k_{A\leftarrow S}X_S \\
\dot{X}_S &= \quad k_{A\to S}X_A \;-\; (k_{A\leftarrow S} + k_{S\to G})X_S \;+\; k_{S\leftarrow G}X_G \\
\dot{X}_G &= \quad + \quad k_{S\to G}X_S \;-\; k_{S\to G}X_G
\end{aligned}
\tag{2.28}
$$

$$X_A(t=0) = X_A(0), \quad X_S(t=0) = X_S(0) = 1 - X_A(0), \quad X_G(t=0) = 0 \tag{2.29}$$

The characteristic equation of the macro-rate constants ω_i with respect to the micro rate constants k_j for this system is given by Eq. 2.30. The fit coefficients for the unique solution (Eq. 2.31) are parameterized in Table 3.15.

$$\omega^2 + (k_{A\leftarrow S} + k_{A\to S})\omega - k_{A\leftarrow S}k_{A\to S} = 0 \tag{2.30}$$

$$X_A(t) = X_1 e^{\omega_1 t} + X_2 e^{\omega_2 t} + X_3 e^{\omega_3 t} \tag{2.31}$$

2.3 Monte Carlo Simulation of Radioactive Particle

A preliminary Monte Carlo simulation of alphas uniformly ejecting from a spherical particulate of transuranic oxide through respirable particle sizes was performed using the Geant4 Particle Transport code. A wireframe model of the radioparticulate is depicted in Fig. 2.2 which includes the trajectories for several alpha emissions. The simulation required the *UltraPhysicsList.hh* header file appended with alpha particle definitions for the low energy electromagnetic interactions and Bragg ion models. Ten million alpha events were generated from uniformly probable locations within the sphere to determine the average yield (Fig. 3.10) and average energy (Fig. 3.11) of exiting particles
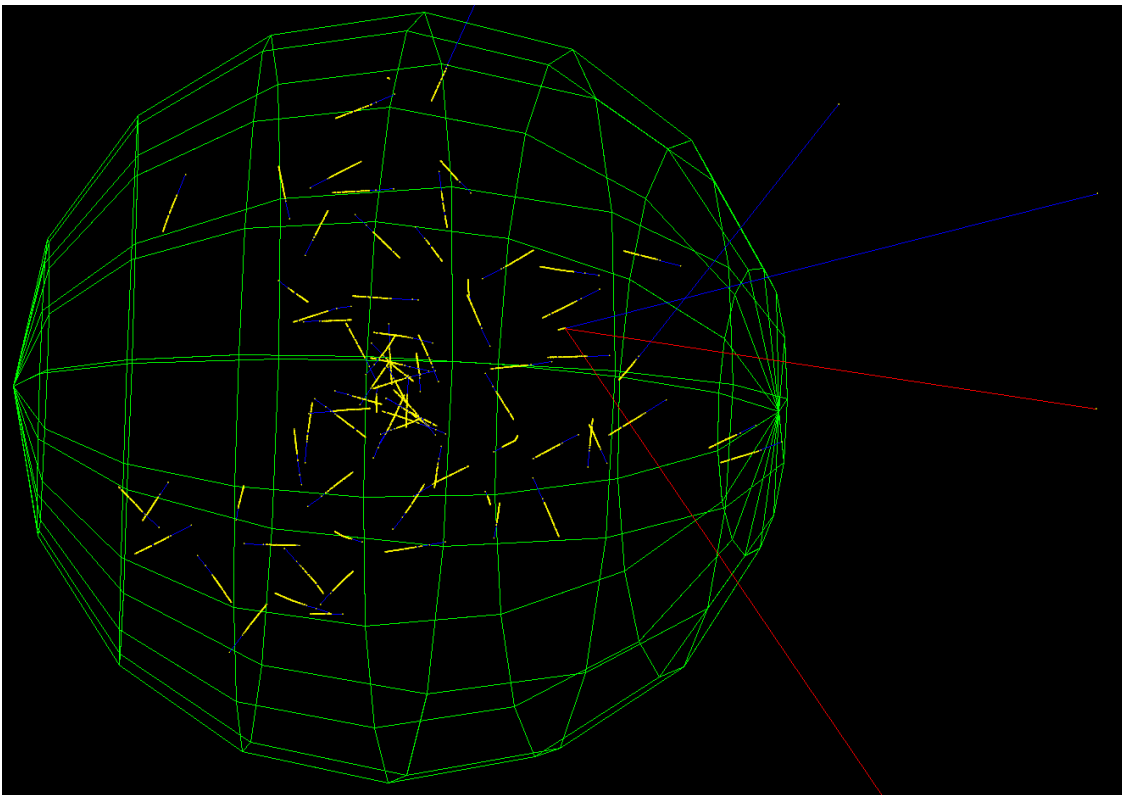
Figure 2.2: Geant4 AmO$_2$ particulate geometry 20 μm in diameter with 100 5.485 MeV alpha event trajectories. Blue lines are positive α tracks, red lines are negative $\beta-$ tracks, and yellow dots indicate nuclear collisions.

2.3.1 Geometry Definitions

Each radioparticulate was defined as a uniform sphere of dioxides of each radioisotope. The diameter ranged from 0.125 to 20 μm in steps of 0.125 μm. Using a custom *DetectorConstruction.cc*, each oxide material was defined at 1 atm of pressure and 20°C, which are the default parameters for new materials. The selected oxides are listed in Table 2.2 with the corresponding accepted densities. (Lide, 2006).

Table 2.2: Radioisotope oxides and their densities simulated in Geant4.

Radioisotopes	Oxide	Density (g/cm^3)
U-234 U-235 U-238	UO_2	10.15
Np-237	NpO_2	11.10
Pu-238 Pu-239 Pu-240 Pu-241	PuO_2	11.50
Am-241	AmO_2	11.68

The world was then defined to be spherical, containing the concentrically positioned particle, with twice the diameter of the particle. The default method for defining vacuum in Geant4, which was preferred for the external shell of space in the world, is to construct a nearly empty volume of hydrogen at extremely low density, pressure, and temperature. These values are part of the *PhysicalConstant.h* file in the base code. It will be irrelevant here as the process will be to simply check for exiting alpha particles, ignoring any interactions after they cross the boundary of the radioparticle.

2.3.2 Tracking and Analyses

Tracking Procedure

1. **Wait for step.** A step is an interaction- this occurs stochastically but will always occur at the boundary between two media in Geant4. When a step occurs, commands and functions defined in a custom *SteppingAction.cc* file will process.

2. **Check if alpha in world volume.** If the step involves an alpha particle whose current position is the world volume (external to the particle), <u>do all of the following</u>:

    (a) Increment the tally of total exited alphas N by one.

    (b) Increment the tally of total exiting alpha $\sum E$ by the current energy.

    (c) Increment the tally of total exiting alpha $\sum E^2$ by the (current energy)^2.

    (d) "Kill" the particle track, so as to not double-count a later interaction.

Analysis Procedure

1. **Wait for end of run.** A run is the series of primary events, wherein each event simulates all steps of interactions resulting from the primary action. Commands and functions defined in a custom *RunAction.cc* file will process before or after with separate class functions.

2. **Calculate average and standard deviation of yield (Eq. 2.32):**

$$\bar{Y} = \frac{N}{(\text{total events})} \qquad Y_\sigma = \sqrt{\frac{\bar{Y}(1-\bar{Y})}{(\text{total events})}} \qquad (2.32)$$

3. **Calculate average and standard deviation of exiting energy (Eq. 2.33):**

$$\bar{E} = \frac{\sum E}{N} \qquad E_\sigma = \frac{\sqrt{N\left(\sum E^2\right) - \left(\sum E\right)^2}}{N} \qquad (2.33)$$

47

2.4 Experimental Measurements of Particulate Resuspension

To measure the resuspension factor experimentally, a reproducible environmental setup and analytical workflow must be created. The concept is to disperse particulate powder of an identifiable isotope within a confined area, sample the air above the dispersal, and analyze the air samples using neutron activation analysis. The confined area is manifested as a **resuspension chamber**-several of these chambers are set up in a low vibration area of Olin Hall at WPI.

2.4.1 Resuspension Chamber

Equipment and Materials

The resuspension chamber experiment (Figure 2.3) involves a *base*, *tube*, *sampler system*, *base* and *sampler stabilizers* and *tracer powder*.

- The *base* surface is made of a 1 ft^2 poured concrete, a tile of which was purchased from Home Depot. This base, compared to one more organic and porous in nature, contributes to the study being more representative of an urban environment.

- The *tube* is a 6 ft open-ended acrylic tube with 4.25 in inner diameter (US Plastic Corp.) which serves as the chamber wall. The tube is open at both ends.

- The *sampler system* is a low-volume vacuum pump air sampler system (Atlantic Nuclear Corp.) which siphons a flow rate of 2 L min^{-1} through a plastic nozzle fitted with a 47 mm diameter glass fiber filter (Hach Co.). The glass fiber filter is specified by the manufacturer to have a collection efficiency of 99%

- The *base stabilizers* which help hold the tube in place on the base are velcro straps which wrap around the tube and an array of physics stands. Due to the lack of traffic around the chambers, the stabilizers did not need to be robust.

- The *sampler stabilizers* helps hold the sampler head in place in the center of the tube. This is a metal bar to which the sampler tube was clipped.

- The *tracer power* was selected as Europium oxide (Eu_2O_3, $d_p > 1\mu$m, Sigma-Aldrich Corp.), due to being a non-radioactive chemical analog of an isotope of interest, Americium-241. The particle size distribution is such that the average diameter is a few microns, and follows a gaussian distribution.

In addition, continued use of the resuspension chambers will require a digital scale for weighing out powder, one or more utensils for scooping powder, and supplies of the mentioned glass fiber filters, paper sample boats for transporting the tracer, sealable coin envelopes for transporting the used sampler filters, and latex gloves and NIOSH N95 facemasks to protect against exposure to particles.

Resuspension Chamber Construction

1. **Position the bases.** Seek a low-traffic area which has plenty of floorspace and shelving above. Place the bases below and in front of the shelves. Give each base some buffer room from each other for the physics stands.

2. **Stabilize the tubes.** Position the tube in the center of the base. Then place the physics stands around the base and use velcro straps to wrap the tube in place. Once the tube is secure, mark the tube's position with a marker on the concrete around the circumference. To optionally guard against tipping, concrete bricks can be positioned around the chamber.

3. **Install air sampler system.** Assemble the air sampler system and fit the sampler head with a 47 mm diameter glass fiber filter. Place this system on the shelving above the base and tube and connect the power cable to an outlet.

4. **Position the sampler stabilizers.** Lower each sampler head into the tubes. Use the sampler stabilizer to position and clip in-place the sampler tube such that the head hangs in

49
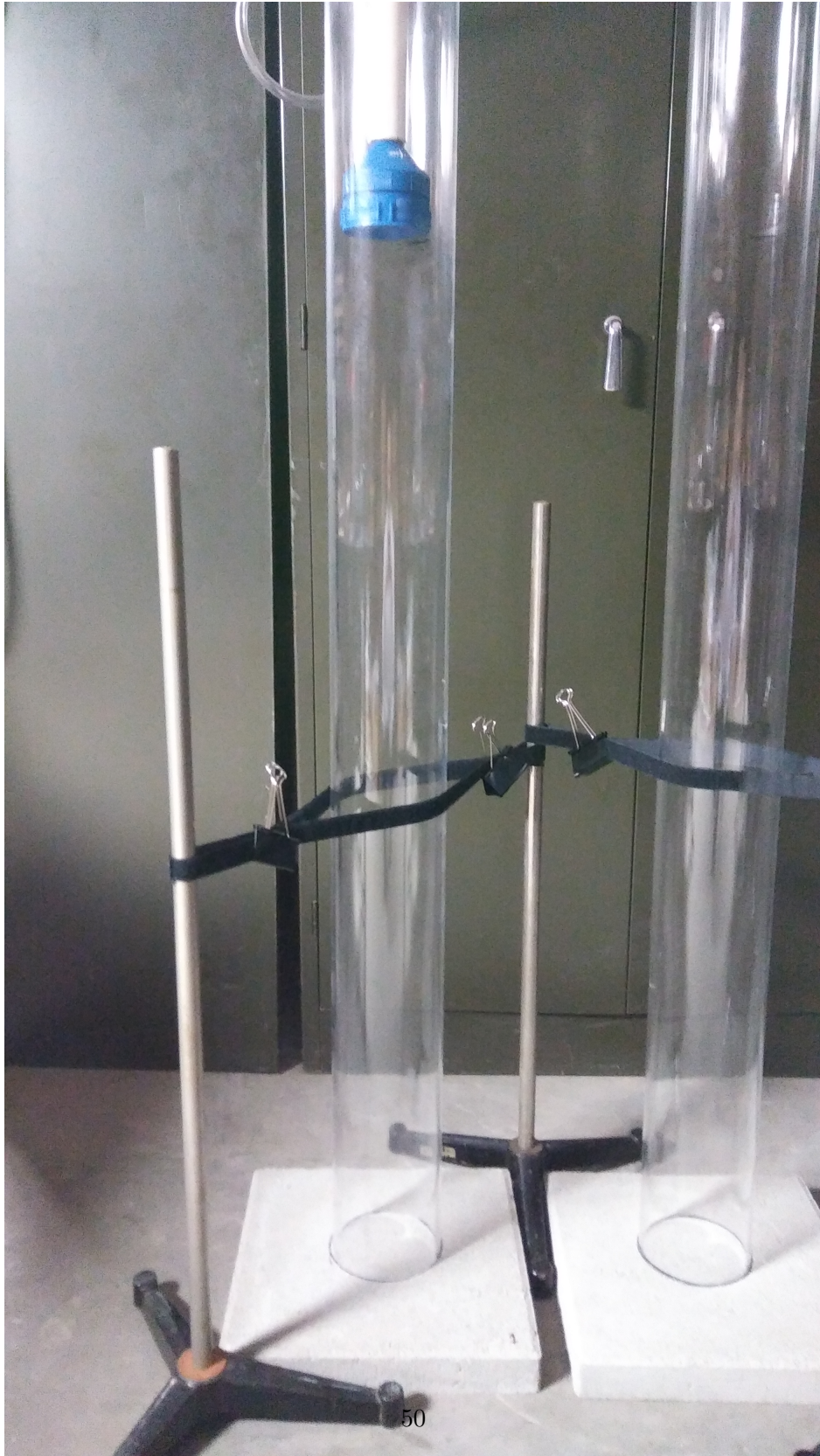
Figure 2.3: Experimental chamber developed for quantifying resuspended powder materials.

the center of the tube, 1 m from the base. When the position is correct, keep the clip on the air sampler tube but remove the sampler head from the resuspension chamber.

Operational Procedure

1. **Measure dispersal samples.** Use the digital scale and scooping utensils to weigh out a mass of the Europium power into the paper sample boats. Repeat this to get as many samples as constructed chambers.

2. **Release the samples into the tubes.**

   - **In a surface release scenario,** the base of the chamber is lifted to one side and the sample is poured within the outline marking the surface area inside the chamber. The chamber is then repositioned to ensure edge placement over the outline, and the paper boat is disposed.

   - **In an air release scenario,** the paper boat containing the sample is inverted within the open top end of the chamber, and the paper boat is disposed.

3. **Begin sampling.** Lower the sampler heads into the resuspension chambers, clipping the sampler tubes to the sampler stabilizer such that the sampler head hangs 1 m above the center of the base. Turn the vacuum pumps on, marking the start time. The room should be locked and public disallowed from entry when running to avoid inadvertent air flow.

4. **Retrieve sample.** On an hourly, daily, or weekly basis, the pumps are turned off to retrieve air sampler filters. Sampler heads are gently pulled directly up and out of each chamber, the head cap is twisted off, and the filter is removed using tongs and placed in coin envelopes which are sealed. New filters are inserted into the sampler head and capped off, and hung back inside the chamber. Upon acquisition and replacement of all filters, the pumps are turned back on for the next time interval.

5. **End experiment.** The experiment ends after a succession of sampler filter collections depending the availability of the workspace. Samplers are turned off and filters are retrieved as usual but sampler heads are not replaced with a new ones. Instead, the chambers are removed from their base and the deposited particulates are vacuumed using a NIOSH-approved HEPA filter. The chambers are then rinsed using a 5:1 water and soap mixture to both remove clung particulates and to create a thin non-polar film of soap to protect against clinging in furture experiments.

Safety

The europium oxide nanopowder used in this study is a dispersable contaminant. The Safety Data Sheet supplied describes the compound as both a toxin and irritant, and recommends a NIOSH/MSHA approved full-facepiece airline respirator, and protective equipment to minimize exposure to the eyes and skin. Wrap-around safety goggles, a full-length labcoat, a double layer of nitrile gloves (to minimize recontamination during strip-down), and N95 model respirator mask are used to address these basic concerns. The only available toxicity data is an oral LD50 of 5000 mg/kg, which resides in the least dangerous Category 5 acute toxicity classification.

Compliance with occupation safety and health standards concerning toxic and hazardous air contaminants is described in 29 CFR 1910.1000(c); specifically, the exposure "shall not exceed the 8-hour time weighted average limit given for that substance in the table". Europium oxide nanopowder is practically a fully respirable mineral dust, which establishes the cumulative exposure concentration limit of 5 mg/m^3. Cumulative exposure E throughout contact with the substance is tallied with the weighted average (Eq. 2.34):

$$E = \sum C \cdot T/(8 \ hours), \tag{2.34}$$

where C is the concentration of the inhaled hazard in mg/m^3, and T is the residence time in hours exposed to C. Exposures resulting from accidents or proximity can be estimated from scenarios with conservative estimates: though this experiment is investigating the fraction resuspended over time, historic observations range from parts per billion (ppb) to parts per million (ppm), so a full tenth resuspension is more than sufficient. In addition, the accident scenario volume for calculating concentration will conservatively consider the active workspace rather than the whole room which it would realistically be dispersed in.

- Source bottle 0.25 m is knocked over and spills 10 g, immediately resuspending a tenth. The user remains one second before making a quick exit (Eq. 2.35):

$$E = \left(\left(\frac{1000 \ mg}{(0.25 \ m)^3}\right) \cdot \left(\frac{1}{3600} \ hours\right)\right)/(8 \ hours) = 2.22 \ mg/m^3 \qquad (2.35)$$

- 0.5 mg falls from the scoopula 0.25 m away, immediately resuspending a tenth. The user remains for another five minutes to complete the preparations (Eq. 2.36):

$$E = \left(\left(\frac{0.05 \ mg}{(0.25 \ m)^3}\right) \cdot \left(\frac{60 \cdot 5}{3600} \ hours\right)\right)/(8 \ hours) = 0.033 \ mg/m^3 \qquad (2.36)$$

- User stumbles and drops the sample cup, resuspending a tenth of a 1 g sample 0.1 m away. Student recovers and leaves within 3 seconds (Eq. 2.37):

$$E = \left(\left(\frac{0.1 \ mg}{(0.1 \ m)^3}\right) \cdot \left(\frac{3}{3600} \ hours\right)\right)/(8 \ hours) = 0.01 \ mg/m^3 \qquad (2.37)$$

- User stands 0.1 m away from a resuspension on the order of 10 parts per million of the original sample, for fifteen minutes to exchange all chamber filters (Eq. 2.38):

$$E = \left(\left(\frac{0.01 \ \mu g}{(0.1 \ m)^3}\right) \cdot \left(\frac{15}{60} \ hours\right)\right)/(8 \ hours) = 0.0003125 \ mg/m^3 \qquad (2.38)$$

These scenarios have been summarized in Table 2.3. By taking active steps of planning and shielding aside from the general practice of maximizing distance and miminimizing time, such as source workbench placement, cardboard-stabilized sample cups with caps, and glass barriers, the user can reduce the cumulative exposure to the hazardous material.

Table 2.3: Experimental respiratory hazard risks and precautionary actions taken to mitigate them.

Task	Issue	Risk	Exposure	Hazard	Precautionary Measures
Sample Preparation	Spill, source bottle	Low	$\sim$2 mg/m^3	Low	Abort and decontaminate
	Spill, scoopula	Low	$\sim$0.1 mg/m^3	Low	Window barrier, suboptimal scooping, separate disposal cup
Sample Injection	Spill, sample cup	Low	$\sim$10 μg/m^3	Low	Stabilizing baseboard, cup cover w/ baseboard, inversion pour
Filter Exchange	Agitated resuspension	Med	$\sim$1 μg/m^3	Low	Chamber procedure leads user progressively further from agitations

2.4.2 Neutron Activation and Analysis

Equipment and Materials

Neutron activation analysis involves a *neutron source*, *gamma detector*, slabs of *Solid Water*, *gold foils*, and a supply of scotch tape for taping samples to the generator.

- The *neutron source* is an Adelphi Technology DD110M portable neutron generator (Figure 2.4) which is characterized by a thermal neutron flux of 10^7 n cm^{-2} s^{-1} at full power. A recent spatial analysis of the neutron flux produced by the model at WPI demonstrated that a flux of 2.0×10^7 n cm^{-2} s^{-1} can be achieved near the center of the beamline, and 1.0×10^7 n cm^{-2} s^{-1} around 3 cm away from the center (Gardner and Crespi, 2015). In addition, the use of a reflecting material such as Solid Water to scatter and thermalize fast neutrons back into a sample enhances the flux to 10^8 n cm^{-2} s^{-1} at full power. The system includes a *chiller*, *high voltage power supplies*, *roughing and turbo vacuum pumps*, *deuterium gas fuel*, *magnetron*, and *target chamber*. The system components are controlled using a proprietary LabView graphical user interface (Fig. 2.5).

Figure 2.4: Cutaway of DD110M Neutron Generator at Worcester Polytechnic Institute.
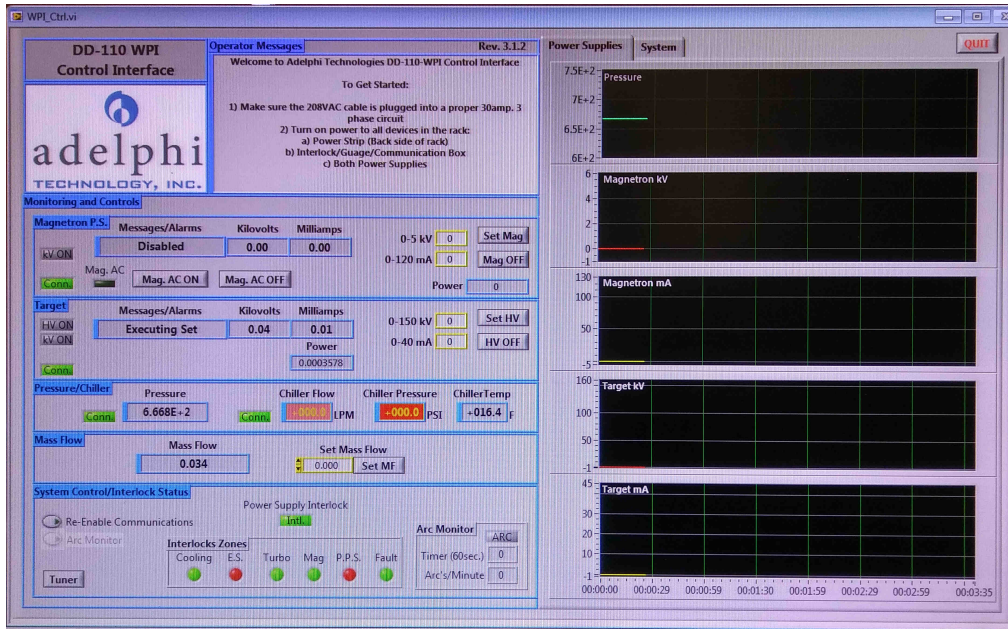
Figure 2.5: Screenshot of LabView interface to control neutron generator voltage, current, and mass flow.

- The *gamma detector* is a High-Purity Broad Energy Germanium Detector (HPGe) and a Lithium-Drifted Broad Energy Well Detector (GeLi, Figure 2.6) (Mirion Technologies [Canberra], Inc.). The detector gamma channel analyzer is regularly calibrated using check sources such as Co-60, Mn-54, and Eu-152. The detector efficiency functional is also calibrated using the dated activity of the check sources. Germanium detectors must be cooled with liquid nitrogen to produce spectrocscopic data, but HPGe detectors can warm to room temperatures when not in use.

- *Solid Water* is a proprietary medical physics phantom material which mimics the physical and nuclear properties of water. Slabs of Solid Water can serve as a moderator to absorb and rescatter neutrons back into the vicinity of the sample.

- By finding the weight of a *gold foil* and its activity after activation, the neutron flux can be back-calculated and used for a simultaneous sample analysis.

56

Figure 2.6: Lead-shielded Broad Energy GeLi Well Detector used to count active samples.

Operational Procedure

1. **Initialize and ramp up generator.** The generator chamber must be evacuated to near vacuum pressure before usage- this requires the *roughing and turbo vacuum pumps* to be running for 2-3 days before usage. The user must turn on the *chiller* and *high voltage power supplies*, and open the stop-valve of the *deuterium gas fuel*. Then in the LabView computer interface, the user slowly increases the voltage of the *magnetron* and *target chamber* to their operating levels. This process can vary from 10 minutes to an hour depending on the presence of "arcing" or short-circuits followed by immediate shutdown of the magnetron.

2. **Fix gold foil and sample to generator at beam centerline.** A gold foil of known mass is taped to an envelope stack containing filter samples, which is then taped to the generator in front of the beamline. Slabs of Solid Water are pressed to the back of the samples to increase local neutron flux.

3. **Engage magnetron and control beamline.** With the magnetron voltage and current set (5 kV, 115 mA), turn on the magnetron in the LabView software and irradiate for 8 hours, comparable to the 9.316 hour half-life of the prominent nuclear reaction Eu-151(n,γ)Eu-152m.

4. **Halt irradiation and count gold foil activity.** Use the LabView software to shut down the generator magnetron, and bring the gold foil from the generator to the BEGe/GeLi detector, using tape as needed. In the GENIE 2000 or Prospect gamma acquisition software (Mirion Technologies (Canberra), Inc.), engage the detector high voltage supply and count the gamma events from the gold for 5-10 minutes.

5. **Count sample activity.** Bring the gold foil from the generator to a shielded storage then bring the sample to the BEGe/GeLi detector, using tape as needed. Engage the detector high voltage supply and count the gamma events from the sample for 2-8 hours.

Safety

Compliance with occupational dose limits for adults concerning workplace radiation is described in 10 CFR 20.1201; specifically, (1) an annual limit of "the total dose equivalent being equal to 5 rems (0.05 Sv); or" (2) an annual limit of "a shallow-dose equivalent of 50 rem (0.5 Sv) to the skin of the whole body or to the skin of any extremity".

The europium oxide tracer powder is non-radioactive, but the powder and gold foil become activated after irradiation with the neutron beam, both with appreciable half-lives. The radionuclide data sheet for each activated nuclide (Eu-152, Eu-154, Au-198) provides the gamma constants, the dose-rates relative to the activity of the nuclide for different exposure scenarios (Delacroix et al., 2002). These are used in determining the effective dose from an external point gamma source equation (Eq. 2.39; NRC, 2012). The equation is simplified such that the decay is assumed to not be appreciable and is thus a more conservative estimate (Domenech, 2017).

$$E = \frac{\Gamma A_0 t}{r^2} \tag{2.39}$$

- **During transportation,** the gold and sample can be considered as point sources from 30 cm away ("average length of forearm" in datasheet calculations).

- **During counting,** the gold and sample can be considered as point sources approximately 1 m away from the computer which controls the detector. Normally, the user is sitting further away but this will serve as a conservative basline.

The dose rate (mSv h^{-1}) from a point source of 1 MBq of Au-198, Eu-152, and Eu-154 30 cm away are given by Eq. 2.40. For a distance of 1 m from point source, the proportionate dose rate can be found using the inverse-square law (Eq. 2.41).

$$\dot{D}_{MBq \ Au-198} = 0.124764, \quad \dot{D}_{MBq \ Eu-152} = 0.02698, \quad \dot{D}_{MBq \ Eu-154} = 0.06747 \tag{2.40}$$

$$\dot{D}_1 r_1^2 = \dot{D}_2 r_2^2 \quad \longrightarrow \quad \dot{D}_{1m} = \dot{D}_{30cm}/11.11 \tag{2.41}$$

The activity of the gold or sample can be found with the neutron activation production rate (Eqs. 1.27, 2.42) for a given mass of each species.

$$A = N\sigma\phi = mN_A\sigma\phi/M \tag{2.42}$$

The mass of the gold is generally less than 0.1 g, but said value will provide a reasonable conservative mass. The Europium, which has relative abundances between Eu-151 and Eu-153, is likely to be orders of magnitudes less than the deposited amount in the experiment, but like with the particulate matter an assumed resuspension and collection of one-tenth will suffice, so 0.1 g Eu_2O_3, or 0.0413 g Eu-151 and 0.0451 g Eu-153. Using 2 minutes for transportation, 10 minutes for Au-198 counting and 2 hours for Eu counting, dose predictions are calculated for different irradiation times in Table 2.4. By maximizing distance and shielding and miminimizing time, the user can reduce the cumulative exposure to radiation.

Table 2.4: Radiation dose estimates (Sv) for the experimental procedure for different irradiation times.

Task	2 hr	4 hr	8 hr	24 hr
Transportation				
Au-198	1.330×10^{-7}	2.631×10^{-7}	5.153×10^{-7}	1.422×10^{-6}
Eu-152	7.883×10^{-10}	1.577×10^{-9}	3.153×10^{-9}	9.459×10^{-9}
Eu-154	1.148×10^{-10}	2.295×10^{-10}	4.590×10^{-10}	1.377×10^{-9}
Counting				
Au-198	1.197×10^{-8}	2.368×10^{-8}	4.637×10^{-8}	1.280×10^{-7}
Eu-152	7.095×10^{-11}	1.419×10^{-10}	2.838×10^{-10}	8.513×10^{-10}
Eu-154	1.033×10^{-11}	2.065×10^{-11}	4.131×10^{-11}	1.239×10^{-10}
Total	1.459×10^{-7}	2.888×10^{-7}	5.656×10^{-7}	1.562×10^{-6}

Thus, the radiation dose for any given sample analysis procedure is orders of magnitude lower than the annual dose limit prescribed by 10 CFR 20.1201. Performing the analysis using a 24 hr irradiation every day of the year will still only amount to a whole body dose of 0.5701 mSv, just over a hundredth of the limit.

2.4.3 Summary of Experimental Parameters

The resuspension factor S_f and minimum detectable resuspension factor S_f are given below in terms of the ^{151}Eu(n,γ)^{152}Eu reaction, the Eu$_2$O$_3$ compound, and other outlined experimental procedures (Eqs. 2.43,2.44). These are calculated in a similar manner as the minimum detectable resuspension factor MDS$_f$ (Eq. 1.32); in place of the lower detection limit L_D we use measured counts C^* and C^{Au}. The values listed in Table 2.5 will be obtained during the experimental calibration and procedure. Table 2.6 list the physical properties and assumed parameters used in the experiments.

$$MDS_f = \frac{A\left(k^2 + 2k\sqrt{2\mu_b}\right)\left(M_{Eu-151} + \frac{M_{Eu-153}a_{Eu-153}}{a_{Eu-151}}\right)}{\epsilon_F Y_{Eu} m_0 X_F f t_s \epsilon N_A \sigma_{Eu} \phi \left(1 - e^{-\lambda\tau}\right)\left(\frac{e^{-\lambda t}}{\lambda}\right)\left(1 - e^{-\lambda\Delta t}\right)} \tag{2.43}$$

$$S_f = \frac{AC^*\left(M_{Eu-151} + \frac{M_{Eu-153}a_{Eu-153}}{a_{Eu-151}}\right)}{\epsilon_F Y_{Eu} m_0 X_F f t_s \epsilon N_A \sigma_{Eu} \phi \left(1 - e^{-\lambda\tau}\right)\left(\frac{e^{-\lambda t}}{\lambda}\right)\left(1 - e^{-\lambda\Delta t}\right)} \tag{2.44}$$

$$\phi = \frac{C^{Au} M_{Au}}{\epsilon Y_{Au} m_{Au} N_A \sigma_{Au} \left(1 - e^{-\lambda_{Au}\tau}\right)\left(\frac{e^{-\lambda_{Au} t}}{\lambda_{Au}}\right)\left(1 - e^{-\lambda_{Au}\Delta t}\right)} \tag{2.45}$$

Table 2.5: Experimental values to be obtained during the procedure governing S_f and MDS_f through neutron actviation analysis in the experiments of this study.

Parameter	Description
μ_b	(s^{-1}); Average detector background count rate
ϵ	Total detector efficiency for gamma spectroscopy
C^*	Count of gamma events from irradiated sample
m_{Au}	Mass of goil foil used for flux callibration
C^{Au}	Count of gamma events from irradiated gold foil
ϕ	(neutrons cm^{-2} s^{-1}); Neutron flux delivered to samples
t	(hr); time delay between activation and gamma detection
Δt	(hr); gamma detection time period

Table 2.6: Physical constants and assumed parameters governing S_f and MDS_f through neutron actviation analysis in the experiments of this study.

Parameter	Value	Description
k	1.645	k-value of 95% confidence of non-Type I and II errors
Y_{Eu}	0.1420	Average yield of 841.6 keV γ from ^{151}Eu(n,γ)^{152}Eu
Y_{Au}	0.96	Average yield of 841.6 keV γ from ^{197}Au(n,γ)^{198}Au
σ_{Eu}	3.30×10^{-25}	(m^2); absorbtion cross-section of ^{151}Eu(n,γ)^{152}Eu
σ_{Au}	9.87×10^{-27}	(m^2); absorbtion cross-section of ^{197}Au(n,γ)^{198}Au
N_A	6.022×10^{23}	(mol^{-1}); Avogadro's number- number of atoms in a mole
M_{Eu-151}	150.9	(g mol^{-1}); Molar mass of Eu-151
M_{Eu-153}	152.9	(g mol^{-1}); Molar mass of Eu-153
M_{Au}	197.0	(g mol^{-1}); Molar mass of Au-197
a_{Eu-151}	0.4791	Relative abundance of of Eu-151
a_{Eu-153}	0.5219	Relative abundance of of Eu-153
λ	0.0746	(hr^{-1}); decay constant for Eu-152
λ_{Au}	0.0746	(hr^{-1}); decay constant for Au-198
t_s	[1, 24, 168]	(hr); air sampling time period
τ	[2, 8, 24]	(hr); neutron irradiation time period
m_0	[0.010, 1.00]	(g); mass of initial compound deposition
X_F	0.70	Relative fraction of Eu to Eu$_2$O$_3$ by mass
A	9.152×10^{-3}	(m^2); surface area of deposition
f	3.333×10^{-5}	(m^3 s^{-1}); flow rate of air sampler
ϵ_F	0.99	Fiberglass filter partiulate capture efficiency

Chapter 3

Results

3.1 Resuspension Factor Model Assessment of Historical Data

The historic resuspension data available from references of the assessment by Maxwell and Anspaugh (2011) were used. Some data, such as those provided by Tveten (1990) and Garger (1997) provided additional long-term observations than the sample set depicted in the assessment. These were incorporated into this work to achieve greater accuracy with longer-term fitting. As few studies provided intrinsic collection error, uncertainty propagation was not included in this analysis. The values used are plotted in Fig. 3.1.

Initial resuspension factor observations within days to weeks post-deposition are roughly centered around 10^{-6} m^{-1}, and span up to five orders of magnitude. The majority of measurements past one year have decreased by a factor of 10^3 and span 2-3 orders. The long-term observations approximately contain yearly oscillation in magnitude from Cs-137 measurements following the Chernobyl disaster provided by Garger (1997).
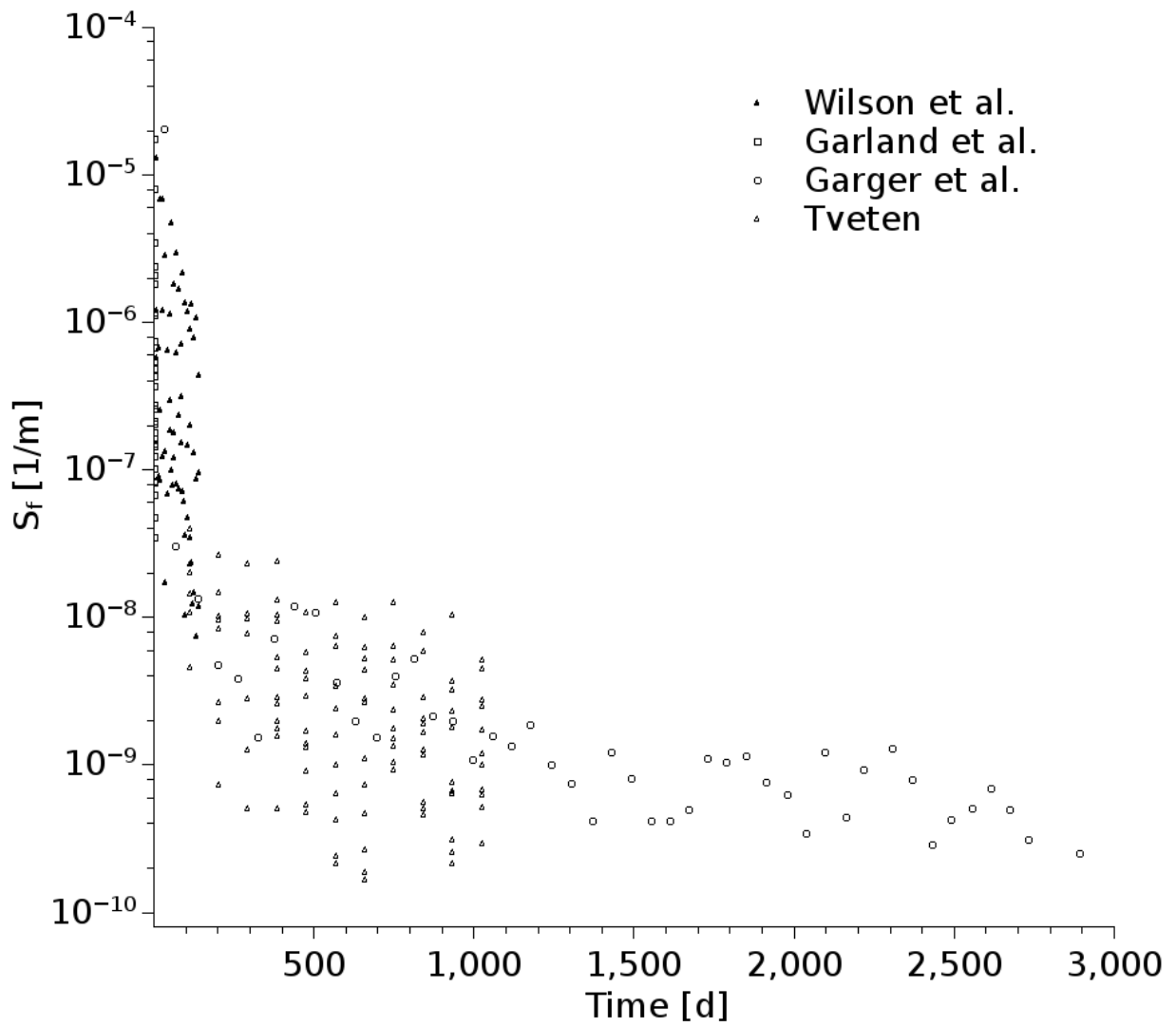
Figure 3.1: Semilog plot of resuspension factor observations from 0.005 to 2890 d.

The dataset is then discretized into bins, roughly three to four days wide in Figure 3.2. Bins which contained only one observation used the lowest calculated spread from the remainder of the set to provide a *relative* instrumental weighting of fits.

65
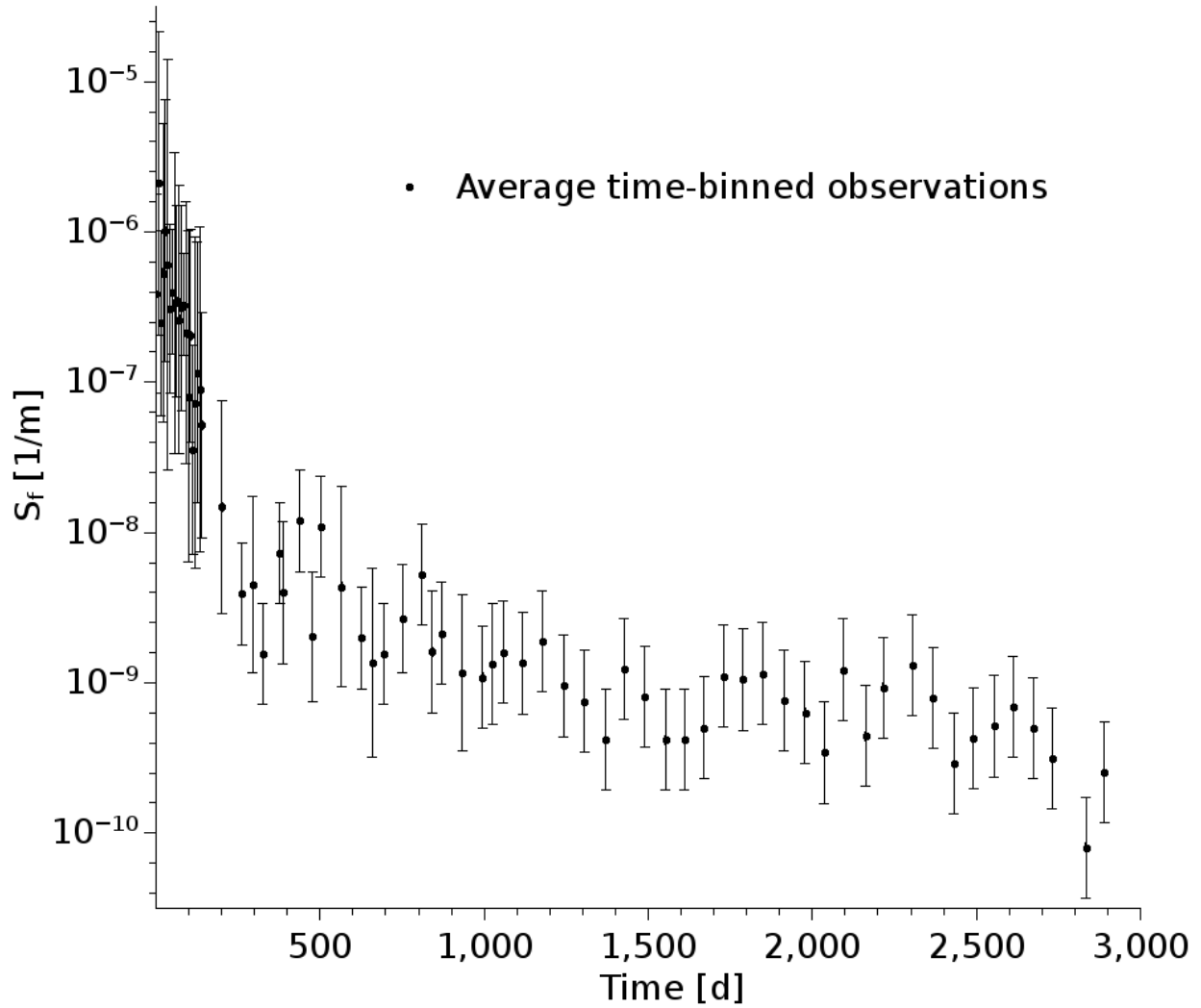
Figure 3.2: Semilog plot of time-bin averaged resuspension factor observations from 0.005 to 2890 d.

The averaged resuspension factor observations are then used to create a best-fit equation similar to the current accepted model of an offset double-exponential (Maxwell and Anspaugh, 2011). This is done both a fixed (10^{-9}) and unfixed (variable) offset term, which is described in further detail among the additional model fits in the next section. The fit equations from this work are plotted on top of the averaged resuspension factor observations among previous models in Figure 3.3.
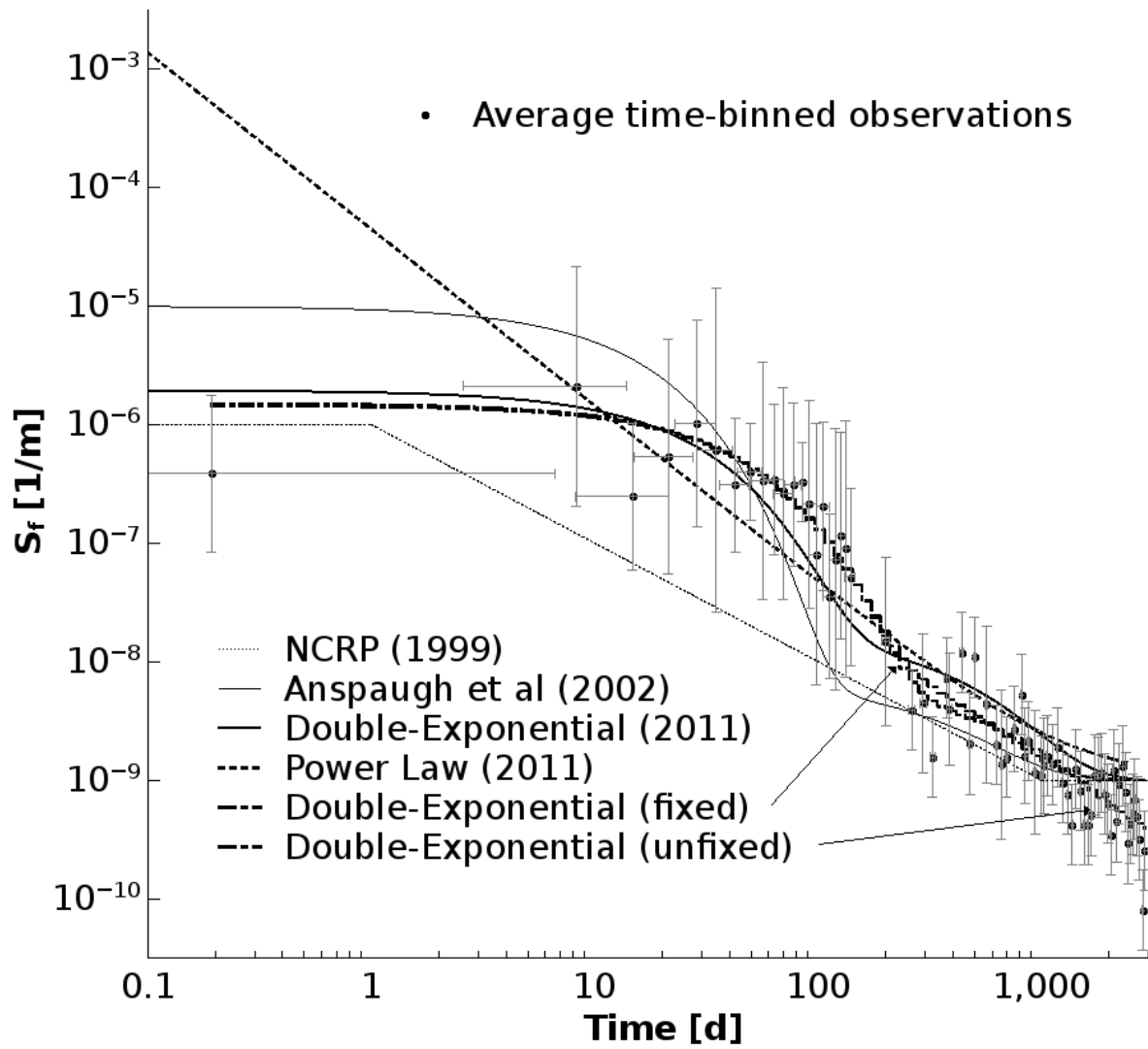
Figure 3.3: Log-log plot of averaged resuspension factor observations, overlaid with recent models including this work (indicated with arrows).

3.1.1 Model Regression Output

The linear regression fit for each model equation is plotted over the binned data in Fig. 3.4. Logarithmic axes are used in both t and S_f for better visibility of short-term changes in observations, normally washed out in an exponential decay. Curve fit parameters with uncertainties and reduced-χ^2 values are given in Tables 3.1 through 3.4.
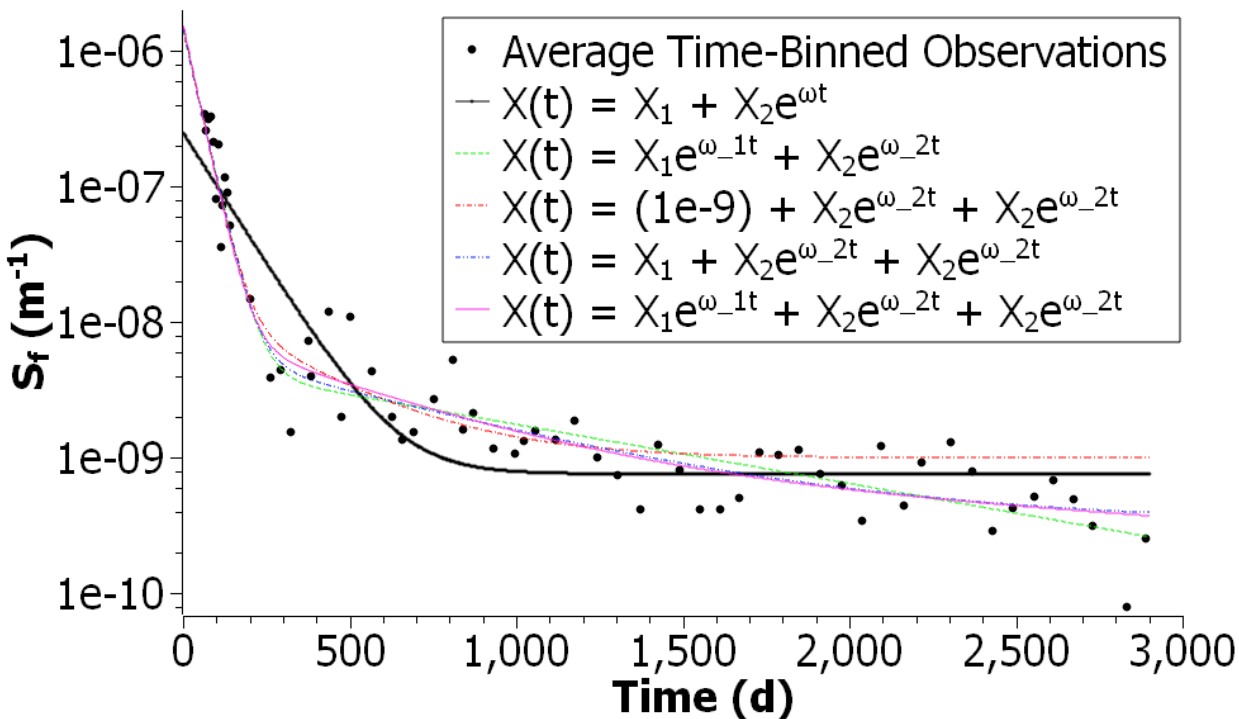
Figure 3.4: Semi-log plot of averaged resuspension factor observations, overlaid with all forms of derived compartment models.

Table 3.1: Best-fit linear regression parameters in log-space of averaged observations for the closed, two-compartment system, which fit with reduced-χ^2 of 0.80.

$X_1\ (\mathrm{m}^{-1})$	$7.62 \times 10^{-10} \pm 9.35 \times 10^{-11}$
$X_2\ (\mathrm{m}^{-1})$	$2.49 \times 10^{-7} \pm 8.97 \times 10^{-8}$
$\omega_2\ (\mathrm{d}^{-1})$	-0.00893 ± 0.00112

Table 3.2: Best-fit linear regression parameters in log-space of averaged observations for the open, two-compartment system, which fit with reduced-χ^2 of 0.43.

X_1 (m^{-1})	$4.82 \times 10^{-9} \pm 8.89 \times 10^{-10}$
X_2 (m^{-1})	$1.40 \times 10^{-6} \pm 6.26 \times 10^{-7}$
ω_1 (d^{-1})	-0.001004 ± 0.000108
ω_2 (d^{-1})	-0.0248 ± 0.00468

Table 3.3: Best-fit linear regression parameters in log-space of averaged observations for the closed, three-compartment system, which fit with reduced-χ^2 of 0.47.

	Fixed	Unfixed/Alternative
X_1 (m^{-1})	$1.00 \times 10^{-9} \pm 0$	$3.31 \times 10^{-10} \pm 1.38 \times 10^{-10}$
X_2 (m^{-1})	$1.37 \times 10^{-8} \pm 9.67 \times 10^{-9}$	$6.12 \times 10^{-9} \pm 2.01 \times 10^{-9}$
X_3 (m^{-1})	$1.50 \times 10^{-6} \pm 9.98 \times 10^{-7}$	$1.45 \times 10^{-6} \pm 6.89 \times 10^{-7}$
ω_2 (d^{-1})	-0.00346 ± 0.00116	-0.00157 ± 0.000426
ω_3 (d^{-1})	-0.0264 ± 0.00833	-0.0253 ± 0.00534

Table 3.4: Best-fit linear regression parameters in log-space of averaged observations for the open, three-compartment system, which fit with reduced-χ^2 of 0.42.

X_1 (m^{-1})	$9.36 \times 10^{-10} \pm 2.62 \times 10^{-9}$
X_2 (m^{-1})	$8.05 \times 10^{-9} \pm 4.26 \times 10^{-19}$
X_3 (m^{-1})	$1.55 \times 10^{-6} \pm 7.18 \times 10^{-7}$
ω_1 (d^{-1})	-0.000329 ± 0.000763
ω_2 (d^{-1})	-0.00219 ± 0.00193
ω_3 (d^{-1})	-0.0267 ± 0.00605

3.1.2 Model Micro-Rate Constants Evaluation

The initial fractional quantities and micro-rate constants are reported in Tables 3.5 through 3.7. These terms were were extracted from the model fit parameters (Table 3.13) to their respective terms using Mathematica (Version 9.0, Wolfram Research, Inc., Champaign, IL). The assumption that no material is initially dispersed *underground*, $X_G(t = 0) = 0$, constrains the other initial fractional quantities (airborne and surface-bound) to add to unity. The micro-rate constants express the broad time-averaged effects of a naturally-occurring system. Periodically occurring mechanisms apply an average power on the released particulates to achieve a net fractional transport into respective compartments.

Table 3.5: Initial fractional quantities and kinetic rate constants for closed, two-compartment catenary model as determined by historic dataset.

Fractional quantity	
$X_A(0)$	2.50×10^{-7}
$X_S(0)$	$1 - X_A(0)$
Rate constants (d^{-1})	
$k_{A \to S}$	0.0089
$k_{A \leftarrow S}$	6.80×10^{-12}

Table 3.6: Initial fractional quantities and kinetic rate constants for open, two-compartment catenary model as determined by historic dataset.

Fractional quantity	
$X_A(0)$	1.40×10^{-6}
$X_S(0)$	$1 - X_A(0)$
Rate constants (d^{-1})	
$k_{A \to}$	0.0010
$k_{A \to S}$	0.0248
$k_{A \leftarrow S}$	1.147×10^{-10}

Table 3.7: Initial fractional quantities and kinetic rate constants for closed, three-compartment catenary model as determined by historic dataset.

Fractional quantity	
$X_A(0)$	1.46×10^{-6}
$X_S(0)$	$1 - X_A(0)$
Rate constants (d^{-1})	
$k_{A \to S}$	0.0253
$k_{A \leftarrow S}$	1.54×10^{-10}
$k_{S \to G}$	1.48×10^{-3}
$k_{S \leftarrow G}$	8.56×10^{-5}

The calculated micro-rate constants were then used to reconstruct the predicted resuspension under two conditions: $X_A(0) = 0$ and $X_A(0) = 1$. These conditions, the *perfect airborne release* and *perfect surface release* scenarios respectively, provide the minimum and maximum range of resuspension factor values depending upon the initial dispersion fraction in-air. These predictions overlay the averaged historic resuspension factors in Figure 3.5.
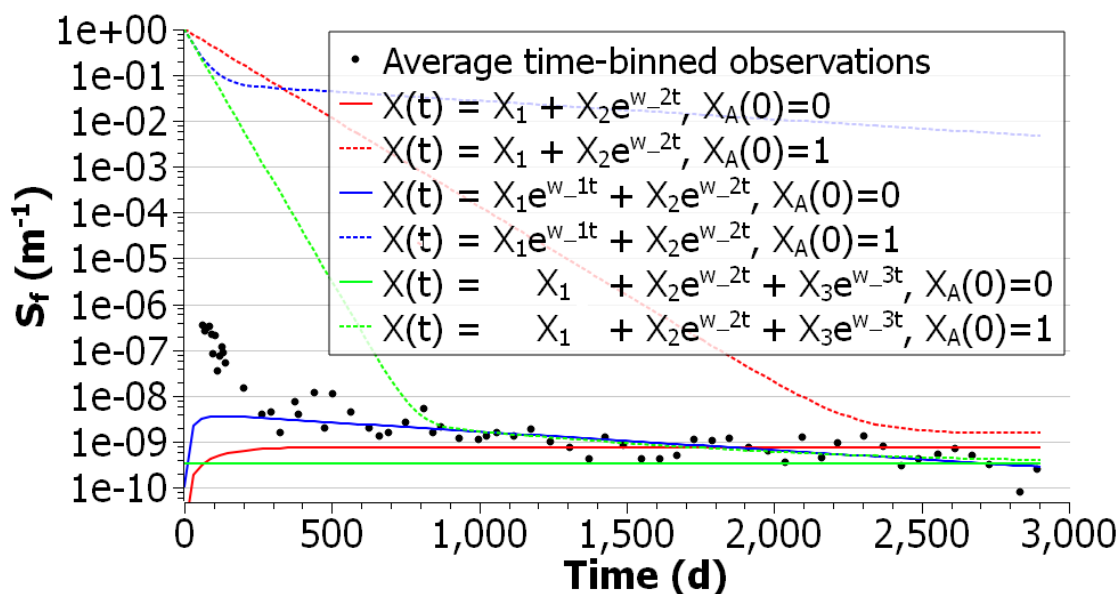
Figure 3.5: Semi-log plot of averaged resuspension factor observations, overlaid with *perfect airborne* and *surface release* scenarios of compartment models based on calculated kinetic rate constants.

The airborne and surface release resuspension factor parameters for each compartment model are listed in Tables 3.8 through 3.10.

Table 3.8: Perfect airborne and surface release predictive model parameters for the closed, two-compartment system.

	Airborne	Surface
X_1 (m^{-1})	~ 1	7.64×10^{-10}
X_2 (m^{-1})	1.53×10^{-9}	7.64×10^{-10}
ω_2 (d^{-1})	-0.00893	-0.00893

Table 3.9: Perfect airborne and surface release predictive model parameters for the open, two-compartment system.

	Airborne	Surface
X_1 (m^{-1})	0.0697	4.15×10^{-9}
X_2 (m^{-1})	0.9303	-4.15×10^{-9}
ω_1 (d^{-1})	-0.000928	-0.000928
ω_2 (d^{-1})	-0.0267	-0.0267

Table 3.10: Perfect airborne and surface release predictive model parameters for the closed, three-compartment system.

	Airborne	Surface*
X_1 (m^{-1})	3.33×10^{-10}	3.33×10^{-10}
X_2 (m^{-1})	6.54×10^{-9}	6.53×10^{-29}
X_3 (m^{-1})	~ 1	1.45×10^{-20}
ω_2 (d^{-1})	-0.0016	-0.0016
ω_3 (d^{-1})	-0.0254	-0.0254

*Though this used the formulas to be prescribed in Tables 3.13 and 3.18, this does not appear to be a reliable output from Mathematica, as $X_A(0) \neq 0$.

3.2 General Solutions to Compartment Models

3.2.1 Model Coefficients and Macro-Rate Constants

The analytical solutions for each parameter of the closed and open two-compartment models are presented in Tables 3.11 and 3.12 respectively. It is assumed in the former that coefficient X_1 corresponds to the constant term wherein $\omega_1 = 0$.

Table 3.11: Solutions to the macro-rate constants and exponential coefficients for the closed, two-compartment catenary system.

ω_2	$-\dfrac{1}{2}\left[(k_{A\to S} + k_{A\leftarrow S}) - \sqrt{(k_{A\to S} + k_{A\leftarrow S})^2 + 4k_{A\to S}k_{A\to S}}\right]$
X_1	$\dfrac{1}{\omega_2}[X_A(0)(k_{A\leftarrow S} + k_{A\to S} + \omega_2) - k_{A\leftarrow S}]$
X_2	$\dfrac{1}{\omega_2}[k_{A\leftarrow S} - X_A(0)(k_{A\leftarrow S} + k_{A\to S})]$

Table 3.12: Solutions to the macro-rate constants and exponential coefficients for the open, two-compartment catenary system.

ω_1	$-\dfrac{1}{2}\left[(k_{A\to S} + k_{A\leftarrow S} + k_{A\to}) + \sqrt{(k_{A\to S} + k_{A\leftarrow S} + k_{A\to})^2 - 4k_{A\to S}k_{A\to}}\right]$
ω_2	$-\dfrac{1}{2}\left[(k_{A\to S} + k_{A\leftarrow S} + k_{A\to}) - \sqrt{(k_{A\to S} + k_{A\leftarrow S} + k_{A\to})^2 - 4k_{A\to S}k_{A\to}}\right]$
X_1	$\dfrac{k_{A\leftarrow S} - (k_{A\to S} + k_{A\leftarrow S} + \omega_2)X_A(0)}{\omega_1 - \omega_2}$
X_2	$\dfrac{(k_{A\to S} + k_{A\leftarrow S} + \omega_1)X_A(0) - k_{A\leftarrow S}}{\omega_1 - \omega_2}$

The analytical solutions for each parameter of the initial and alternative closed three-compartment models are presented in Tables 3.13 and 3.14 respectively. It is assumed in both that coefficient X_1

73

corresponds to the constant term wherein $\omega_1 = 0$.

Table 3.13: Solutions to the macro-rate constants and exponential coefficients for the closed, three-compartment catenary system.

ω_2	$-\dfrac{\chi + \sqrt{\chi^2 - 4(k_{A \to S} k_{S \to G} + k_{A \to S} k_{S \leftarrow G} + k_{A \leftarrow S} k_{S \leftarrow G})}}{2}$
ω_3	$-\dfrac{\chi - \sqrt{\chi^2 - 4(k_{A \to S} k_{S \to G} + k_{A \to S} k_{S \leftarrow G} + k_{A \leftarrow S} k_{S \leftarrow G})}}{2}$
χ	$k_{A \to S} + k_{A \leftarrow S} + k_{S \to G} + k_{S \leftarrow G}$
X_1	$\dfrac{k_{A \leftarrow S} k_{S \leftarrow G}}{\omega_1 \omega_2}$
X_2	$\dfrac{X_A(0)(\omega_1^2 + \omega_1(k_{S \to G} + k_{S \leftarrow G}) + k_{A \leftarrow S}(k_{S \leftarrow G} + \omega_1))}{\omega_1(\omega_1 - \omega_2)}$
X_3	$\dfrac{X_A(0)(\omega_2^2 + \omega_2(k_{S \to G} + k_{S \leftarrow G}) + k_{A \leftarrow S}(k_{S \leftarrow G} + \omega_2))}{\omega_2(\omega_2 - \omega_1)}$

Table 3.14: Solutions to the macro-rate constants and exponential coefficients for the alternative closed, three-compartment catenary system.

ω_2	$-\dfrac{1}{2}\left[(k_{A \to S} + k_{A \leftarrow S} + k_{A \to}) + \sqrt{(k_{A \to S} + k_{A \leftarrow S} + k_{A \to})^2 - 4k_{A \to S} k_{A \to}}\right]$
ω_3	$-\dfrac{1}{2}\left[(k_{A \to S} + k_{A \leftarrow S} + k_{A \to}) - \sqrt{(k_{A \to S} + k_{A \leftarrow S} + k_{A \to})^2 - 4k_{A \to S} k_{A \to}}\right]$
X_1	$\dfrac{k_{A \leftarrow S} - (k_{A \to} + k_{A \leftarrow S})X_A(0)}{(k_{A \to} + k_{A \to S}) + (k_{A \to} + k_{A \to S} + \omega_2)\left(\frac{\omega_3}{\omega_2 - \omega_3}\right) - (k_{A \to} + k_{A \to S} + \omega_3)\left(1 + \frac{\omega_3}{\omega_2 - \omega_3}\right)}$
X_2	$\dfrac{k_{A \to} X_A(0) + \omega_3 X_1}{\omega_2 - \omega_3}$
X_3	$-X_1 - X_2$

The analytical solutions for each parameter of the open three-compartment models are presented in Table 3.15. It should be noted that intermediate terms χ_a, χ_b, and χ_c are defined in order to simplify the expressions in ω_1, ω_2, and ω_3.

Table 3.15: Solutions to the macro-rate constants and exponential coefficients for the open, three-compartment catenary system.

ω_1	$\chi_a - \dfrac{(k_{A\rightarrow} + k_{S\leftarrow G} + k_{A\leftarrow S} + k_{S\rightarrow G} + k_{A\rightarrow S})}{3} - \dfrac{\chi_b}{\chi_a}$
ω_2	$\dfrac{\chi_b}{2\chi_a} - \dfrac{\chi_a}{2} - \dfrac{(k_{a\rightarrow S} + k_{A\rightarrow} + k_{S\leftarrow G} + k_{A\leftarrow S} + k_{S\rightarrow G})}{3} - \mathbf{i}\dfrac{\sqrt{3}\left(\chi_a + \frac{\chi_b}{\chi_a}\right)}{2}$
ω_2	$\dfrac{\chi_b}{2\chi_a} - \dfrac{\chi_a}{2} - \dfrac{(k_{a\rightarrow S} + k_{A\rightarrow} + k_{S\leftarrow G} + k_{A\leftarrow S} + k_{S\rightarrow G})}{3} + \mathbf{i}\dfrac{\sqrt{3}\left(\chi_a + \frac{\chi_b}{\chi_a}\right)}{2}$
χ_a	$\sqrt[3]{\sqrt{\left(\dfrac{(k_{A\rightarrow S} + k_{A\rightarrow} + k_{S\leftarrow G} + k_{A\leftarrow S} + k_{S\rightarrow G})^3}{27} - \chi_c + \dfrac{k_{A\rightarrow}k_{S\leftarrow G}k_{A\leftarrow S}}{2}\right)^2 + \chi_b^3 \cdots} - \dfrac{(k_{A\rightarrow S} + k_{A\rightarrow} + k_{S\leftarrow G} + k_{A\leftarrow S} + k_{S\rightarrow G})^3}{27} + \chi_c - \dfrac{k_{A\rightarrow}k_{S\leftarrow G}k_{A\leftarrow S}}{2}}$
χ_b	$\dfrac{(k_{A\rightarrow S}k_{S\leftarrow G} + k_{A\rightarrow S}k_{S\rightarrow G} + k_{S\leftarrow G}k_{A\leftarrow S})}{3} - \dfrac{(k_{A\rightarrow S} + k_{A\rightarrow} + k_{S\leftarrow G} + k_{A\leftarrow S} + k_{S\rightarrow G})^2}{9}$
χ_c	$\dfrac{(k_{A\rightarrow S}k_{S\leftarrow G} + k_{A\rightarrow S}k_{S\rightarrow G} + k_{S\leftarrow G}k_{A\leftarrow S})(k_{A\rightarrow S} + k_{A\rightarrow} + k_{S\leftarrow G} + k_{A\leftarrow S} + k_{S\rightarrow G})}{6}$
X_1	$\dfrac{\dfrac{X_A(0)\left(\frac{k_{A\rightarrow S}+\omega_3}{\omega_2-\omega_3}-1\right)(k_{A\rightarrow S}+\omega_3)}{k_{A\rightarrow}+k_{S\leftarrow G}+\omega_3} + \dfrac{X_A(0)(k_{A\rightarrow S}+\omega_2)(k_{A\rightarrow S}+\omega_3)}{(\omega_2-\omega_3)(k_{A\rightarrow}+k_{S\leftarrow G}+\omega_2)}}{\dfrac{k_{A\rightarrow S}+\omega_1}{k_{A\rightarrow}+k_{S\leftarrow G}+\omega_1} + \dfrac{(k_{A\rightarrow S}+\omega_3)\left(\frac{\omega_1-\omega_3}{\omega_2-\omega_3}-1\right)}{k_{S\leftarrow G}+k_{A\rightarrow}+\omega_3} + \dfrac{(k_{A\rightarrow S}+\omega_2)(\omega_1-\omega_3)}{(\omega_2-\omega_3)(k_{A\rightarrow}+k_{S\leftarrow G}+\omega_2)}}$
X_2	$\dfrac{X_1(\omega_3-\omega_1) - X_A(0)(k_{A\rightarrow S}+\omega_3)}{\omega_2-\omega_3}$
X_3	$X_A(0) - X_1 - X_2$

3.2.2 Model Initial Conditions and Micro-Rate Constants

The analytical solutions for each average initial conditions and micro-rate constants for the closed and open two-compartment models are presented in Tables 3.16 and 3.17 respectively.

Table 3.16: Solutions to the initial condition and micro-rate constants for the closed, two-compartment catenary system.

$X_A(0)$	$X_1 + X_2$
$k_{A \to S}$	$\dfrac{4X_1^2 + 6X_1X_2 - 4X_1 + 2X_2^2 - 3X_2 - 1 \ldots \\ \quad + \sqrt{1 + 4X_1 + 2X_2 - 4X_1^2 - 4X_1X_2 + X_2^2}}{2\left(X_1^2 + 2X_1X_2 - X_1 + X_2^2 - X_2\right)(1 - X_1 + X_2)^{-1}\omega_2^{-1}}$
$k_{A \leftarrow S}$	$\dfrac{4X_1^2 + 6X_1X_2 - 4X_1 + 2X_2^2 - 3X_2 - 1 \ldots \\ \quad + \sqrt{1 + 4X_1 + 2X_2 - 4X_1^2 - 4X_1X_2 + X_2^2}}{2\left(X_1^2 + 2X_1X_2 - X_1 + X_2^2 - X_2\right)(X_1 + X_2)^{-1}\omega_2^{-1}}$

Table 3.17: Solutions to the initial condition and micro-rate constants for the open, two-compartment catenary system.

$X_A(0)$	$X_1 + X_2$
$k_{A \leftarrow S}$	$\dfrac{(X_1 - X_2)(\omega_1 - \omega_2) + X_1X_2(\omega_1 + \omega_2) + X_1^2\omega_2 + X_2^2\omega_1 - (X_1 + X_2)\chi}{2(1 - X_1 - X_2)}$
$k_{A \to S}$	$\dfrac{-(X_1 + X_2)(\omega_1 + \omega_2) + X_1X_2(\omega_1 + \omega_2) + X_1^2\omega_2 + X_2^2\omega_1 - (X_1 + X_2)\chi}{2(X_1 + X_2)}$
$k_{A \to}$	$\dfrac{-X_1\omega_2 - X_2\omega_1 - \frac{(X_1-X_2)(\omega_1-\omega_2)+X_1X_2(\omega_1+\omega_2)+X_1^2\omega_2+X_2^2\omega_1-(X_1+X_2)\chi}{2(1-X_1-X_2)}}{X_1 + X_2}$
χ	$\sqrt{2\omega_1\omega_2(X_1X_2 + X_1 + X_2 - 1) + (1 - X_2)^2\omega_1^2 + (1 - X_1)^2\omega_2^2}$

The analytical solutions for average initial condition and micro-rate constants for the closed three-compartment model is presented in Table 3.18. The micro-rate constant parameterization for the open three-compartment model was found to not have an analytical closed-form solution for the terms due to overparameterization of the system.

Table 3.18: Solutions to the initial conditions and micro-rate constants for the closed, three-compartment catenary system.

$$X_A(0) \qquad \frac{X_2 + X_3}{1 - X_1}$$

$$k_{A \leftarrow S} \qquad \frac{2X_2 X_3 \omega_1 \omega_2 (1 - X_1) - X_2 \omega_1^2 (X_1 X_2 + X_3) - X_3 \omega_2^2 (X_1 X_3 + X_2)}{(X_2 + X_3)(X_2 \omega_1 + X_3 \omega_2)}$$

$$k_{A \rightarrow S} \qquad \frac{(X_2 \omega_1 + X_3 \omega_2)(X_1 - 1)}{X_2 + X_3}$$

$$k_{S \rightarrow G} \qquad \frac{\omega_1 \omega_2 (X_2 + X_3)(X_2 X_3 \omega_1^2 - 2X_2 X_3 \omega_1 \omega_2 + X_2 X_3 \omega_2^2)}{(X_2 \omega_1 + X_3 \omega_2)(2X_2 X_3 \omega_1 \omega_2 (1 - X_1) - X_2 \omega_1^2 (X_1 X_2 + X_3) - X_3 \omega_2^2 (X_1 X_3 + X_2))}$$

$$k_{S \leftarrow G} \qquad \frac{X_1 \omega_1 \omega_2 (X_2 + X_3)(X_2 \omega_1 + X_3 \omega_2)}{2X_2 X_3 \omega_1 \omega_2 (1 - X_1) - X_2 \omega_1^2 (X_1 X_2 + X_3) - X_3 \omega_2^2 (X_1 X_3 + X_2)}$$

3.3 Experimental Measurements of Resuspended Particulates at 1 meter

The resuspension chamber experimental setup was evaluated by testing two main conditions: one of a non-energetic but elevated release, and one of a non-energetic surface release. The former condition provided a control from which to test similar releases used in the historic dataset of resuspension factors, most of which were airborne releases, while the latter test provides a method to quantify the resuspension rate by assuming an entirely surface-borne release.

In the airborne release, the majority of the content immediately deposited clumps at the the center of the base, but otherwise uniform (Fig. 3.6). This release was then sampled hourly, the process of which took approximately 20 minutes with the vacuum pumps off.

Figure 3.6: Photo of concrete base of resuspension chamber with small, white, aggregate piles of the sample dust seen in the upper right region of the enclosed area.

Following quantification of the hourly samples through neutron activation analysis, multiple surface tests were carried out using daily sampling; the sample exchange period gradually decreased to 10-15 minutes with user experience. The daily and weekly samples were found to not have any quantifiable mass on the filter with this experimental setup. To determine the limiting timeframe of sampling at this height, the vacuum pumps were left on to sample first a week at a time, then biweekly.

Figure 3.7: Semi-log plot of resuspension factor measurements with the air sampler head positioned a height of 1 m above the surface.

Table 3.19: Resuspension factor measurements of Eu_2O_3 powder on air sampler filters positioned at 1 m via neutron activation analysis for each day- and week-long collection sample, accompanied by corresponding minimum detectable mass (MDM) and resuspension factor (MDS_f) for each analysis.

Mass [g]	Sampling time [h]	Irradiation time [h]	Delay time [h]	Count time [h]	MDS_f [m^{-1}]	Measured S_f [m^{-1}]
0.05	1	2	0.38	2	1.402×10^{-7}	1.038×10^{-6}
0.05	1	2	0.17	2	1.049×10^{-7}	1.373×10^{-7}
0.05	1	2	0.083	2	1.042×10^{-7}	$< MDS_f$

Table 3.20: Resuspension factor measurements of Eu_2O_3 powder on air sampler filters positioned at 1 m via neutron activation analysis for each day- and week-long collection sample, accompanied by corresponding minimum detectable mass (MDM) and resuspension factor (MDS_f) for each analysis.

Mass [g]	Sampling time [h]	Irradiation time [h]	Delay time [h]	Count time [h]	MDS_f [m^{-1}]	Measured S_f [m^{-1}]
0.01	24	2	0.083	2	1.902×10^{-8}	$< MDS_f$
0.05	24	8	0.083	24	5.263×10^{-10}	$< MDS_f$
0.01	168	24	0.5	24	2.125×10^{-10}	$< MDS_f$
0.01	168	7	0.5	24	4.869×10^{-10}	$< MDS_f$
0.01	168	20	5	24	3.005×10^{-10}	$< MDS_f$
0.05	168	24	0.5	24	3.685×10^{-11}	$< MDS_f$
0.05	336	4	0.4	2	1.420×10^{-10}	5.024×10^{-8}

3.4 Experimental Measurements of Resuspended Particulates at $^1/_4$ meter

Following the results of the 1 m sampling height experiments, it was determined that there is not a sufficient amount of resuspended material at that height from which to analyze samples. Therefore, the sampler head was lowered to a height of $\dfrac{1}{4}$ m from the resuspension chamber base. This was done by adjusting the clip on the sampler stabilizer to give the sampler head tube more slack into the chamber. The remaining experimental protocol was followed.
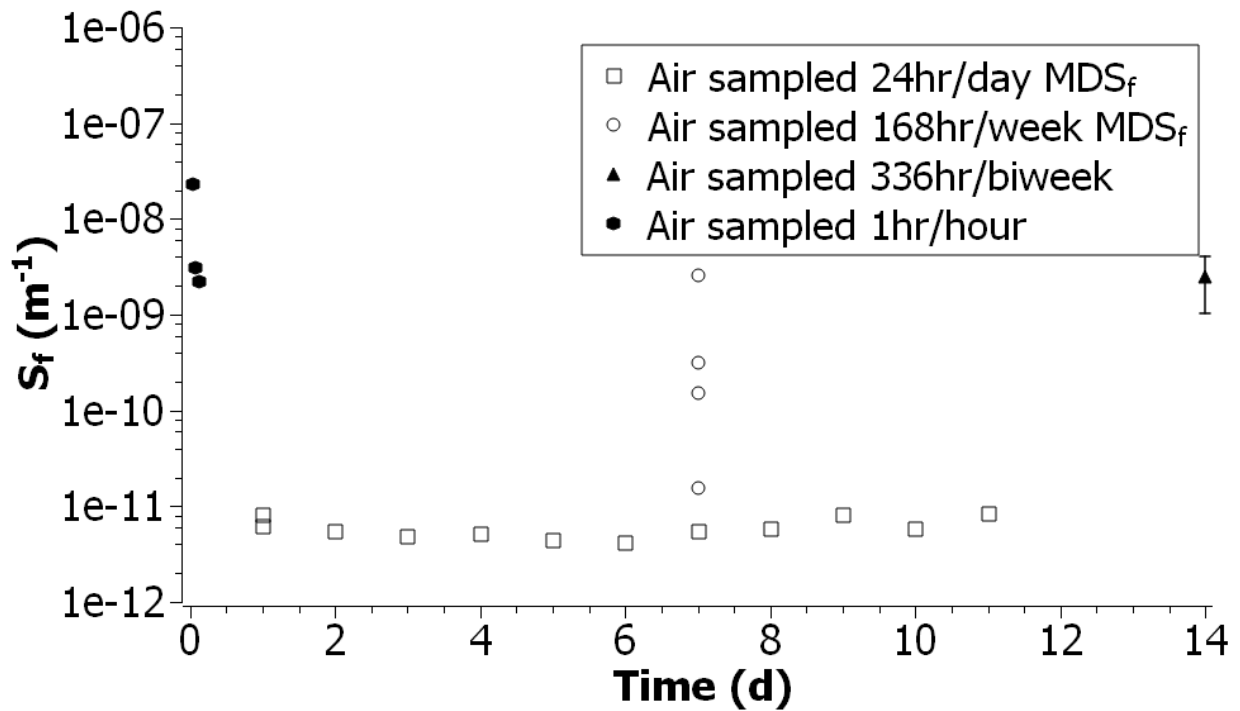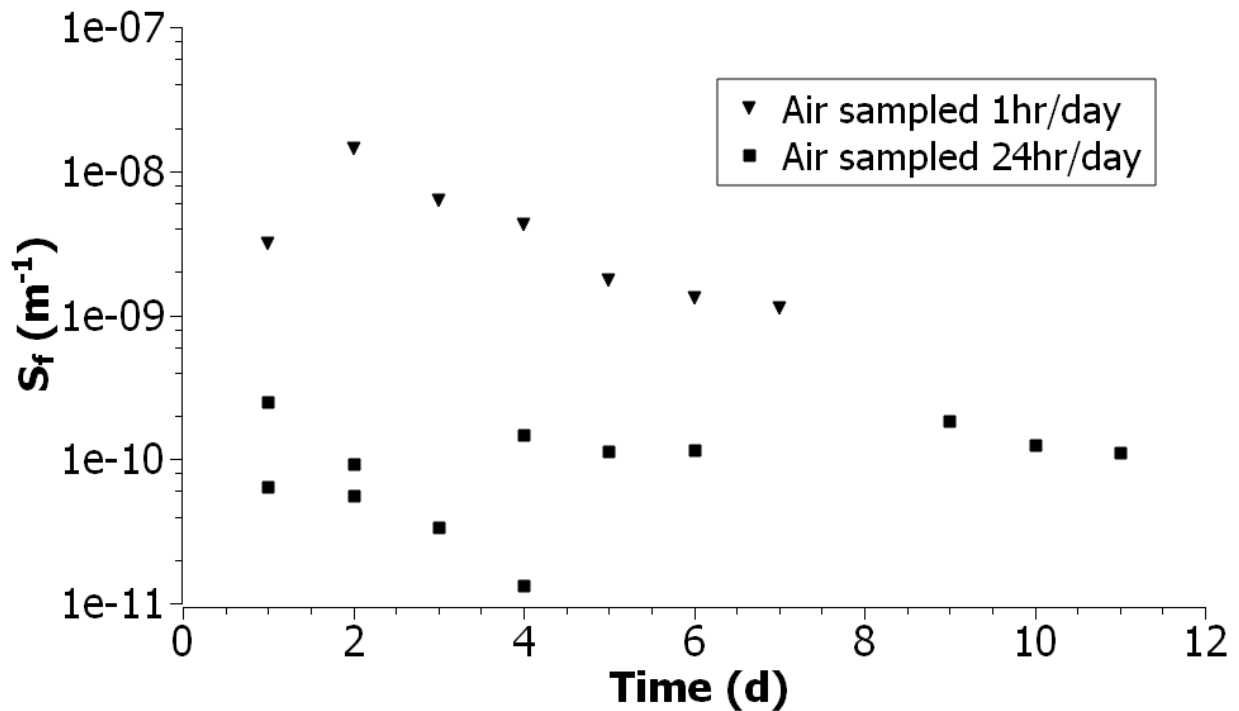

Figure 3.8: Semi-log plot of resuspension factor measurements with the air sampler head positioned a height of 0.25 m above the surface.

Table 3.21: Resuspension factor measurements of Eu_2O_3 powder on air sampler filters positioned at 0.25 m via neutron activation analysis for each day- and hour-long collection sample, accompanied by corresponding minimum detectable mass (MDM) and resuspension factor (MDS_f) for each analysis.

Mass [g]	Sampling time [h]	Irradiation time [h]	Delay time [h]	Count time [h]	MDS_f $[m^{-1}]$	Measured S_f $[m^{-1}]$
5	24	2	0.3	2	2.042×10^{-11}	6.487×10^{-11}
5	24	2	0.3	2	1.402×10^{-11}	5.558×10^{-11}
5	24	2	0.3	2	6.606×10^{-12}	3.347×10^{-11}
5	24	2	0.3	2	3.195×10^{-12}	1.398×10^{-11}
5	24	2	0.3	2	1.263×10^{-11}	4.285×10^{-10}
5	24	2	0.3	2	1.277×10^{-11}	9.196×10^{-11}
5	24	2	0.3	2	5.115×10^{-12}	1.481×10^{-10}
5	24	2	0.3	2	4.496×10^{-12}	1.144×10^{-10}
5	24	2	0.3	2	4.163×10^{-12}	1.165×10^{-10}
5	24	2	0.3	2	8.282×10^{-12}	1.861×10^{-10}
5	24	2	0.3	2	5.770×10^{-12}	1.248×10^{-10}
5	24	2	0.3	2	8.384×10^{-12}	1.110×10^{-10}
5	1	2	0.3	2	1.659×10^{-9}	3.101×10^{-9}
5	1	2	0.3	2	1.267×10^{-9}	1.440×10^{-8}
5	1	2	0.3	2	1.051×10^{-9}	6.255×10^{-9}
5	1	2	0.3	2	1.629×10^{-9}	4.240×10^{-9}
5	1	2	0.3	2	1.458×10^{-9}	1.759×10^{-9}
5	1	2	0.3	2	1.122×10^{-9}	1.313×10^{-9}
5	1	2	0.3	2	1.337×10^{-9}	1.120×10^{-9}

These experimental measurements across the two sampling scenarios demonstrated lower magnitudes than historic observations, but provided enough data to apply similar curve fits as before. The relevant open, two-compartment catenary model which uses a double-exponential with no constant offset, was fit to each scenario separately shown in Figure 3.9. Fit equations are parameterized in Table 3.22, and the resulting calculation of initial quantities and kinetic rate constants are presented in Table 3.23.
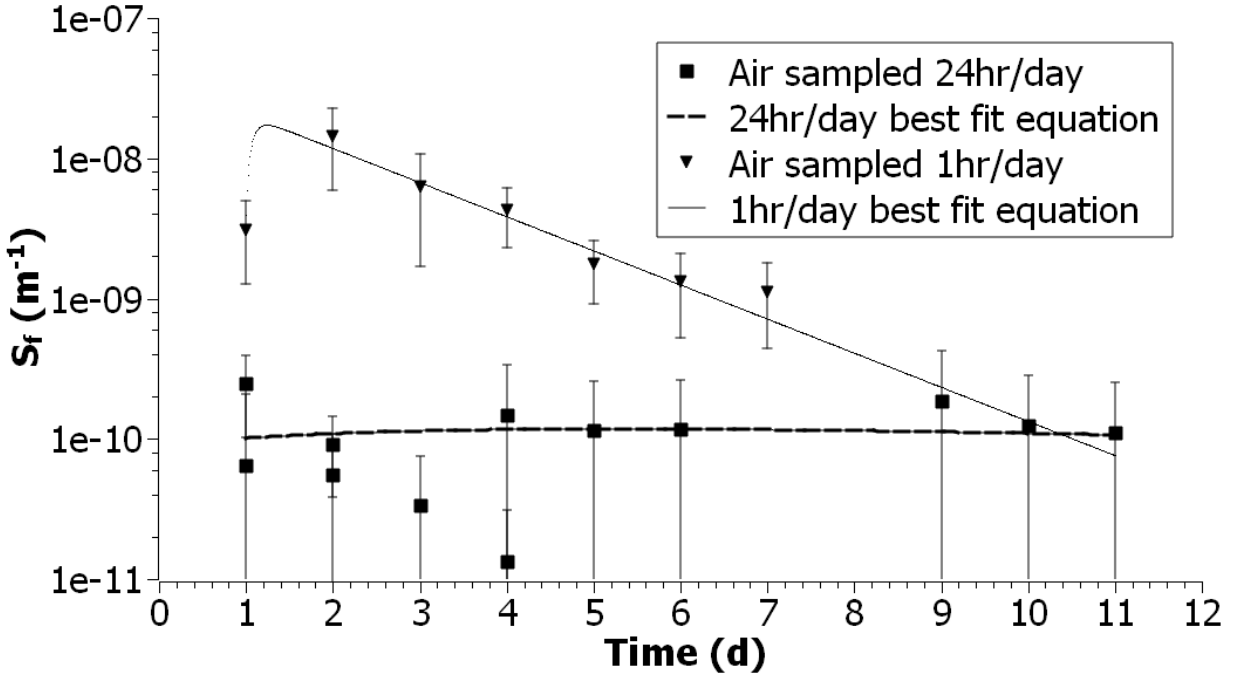
Figure 3.9: Semi-log plot of Resuspension factor measurements via NAA of Eu_2O_3 on filters at 0.25 m for surface releases, overlaid with best fit double-exponential equations.

Table 3.22: Best-fit linear regression parameters in log-space of averaged observations for the hourly- and daily-per-day air sampling data.

	24hr/day	1hr/day
X_1 (m^{-1})	1.68×10^{-10}	5.46×10^{-8}
X_2 (m^{-1})	-7.84×10^{-11}	-0.0187
ω_1 (d^{-1})	-0.0375	-0.676
ω_2 (d^{-1})	-0.254	-13.5

Table 3.23: Initial fractional quantities and kinetic rate constants for open two-compartment model as determined by terms of curve fits of experimental data.

Fractional quantity	24hr/day	1hr/day
$X_A(0)$	8.96×10^{-11}	8.96×10^{-11}
$X_S(0)$	$1 - X_A(0)$	$1 - X_A(0)$
Rate constants (d^{-1})		
$k_{A\rightarrow}$	0.254	13.2
$k_{A\rightarrow S}$	0.203	0.0062
$k_{A\leftarrow S}$	8.49×10^{-12}	0.1154

3.5 Simulation of Particulate Radiation

3.5.1 Average Exiting Alpha Yield

The average yield of alpha particles from the surface of the particle for each radioparticulate is given in Figure 3.10. The range of characteristic alpha particles in their corresponding radioparticulate material extends only a few microns, which is demonstrated by the sudden drop after 2 microns followed by a gradual decline near zero.
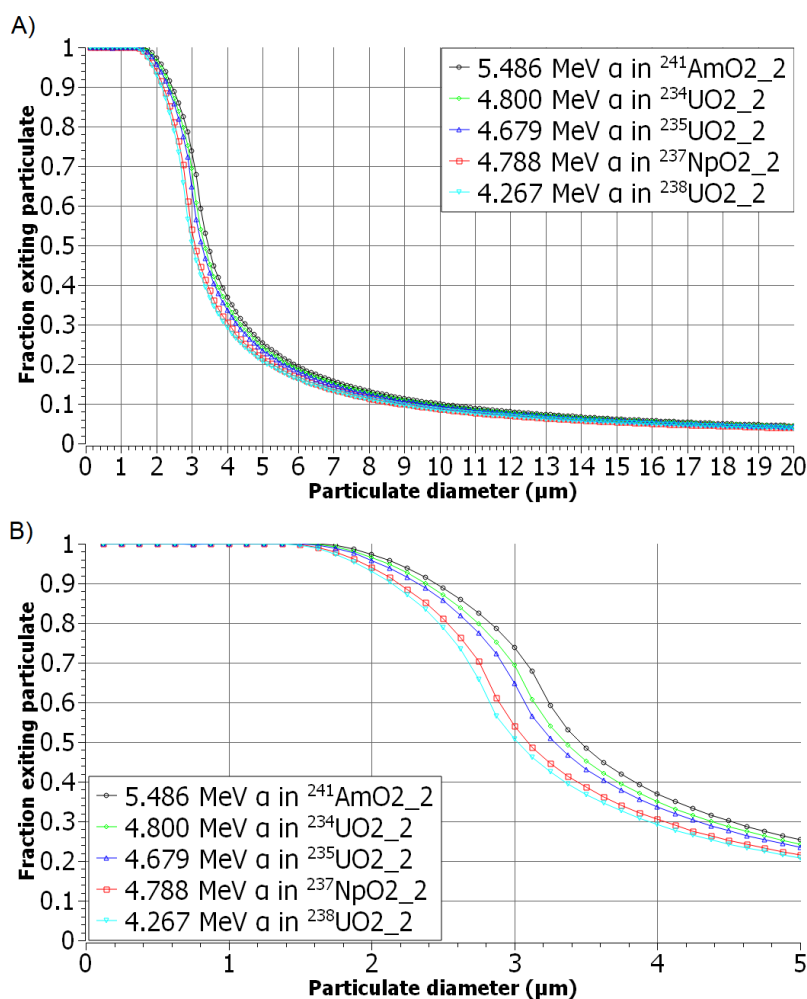
Figure 3.10: Yield of exiting alpha particles from spherical transuranic oxide particulates (A) with zoom into the first five microns in particle diameter (B).

The initial energy, range, and average percent yield for exiting radioparticulate alphas across selection of respirable particle sizes are presented in Table 3.24, alongside respective particulate densities.

Table 3.24: Calculated range and simulated average yield of characteristic alpha particles from the surface of each radioparticulate species.

Species	ρ_m [g/cm^3]	E [MeV]	R_m [μm]	$\bar{Y}_{1\mu m}$ [%]	$\bar{Y}_{2.5\mu m}$ [%]	$\bar{Y}_{5\mu m}$ [%]	$\bar{Y}_{7.5\mu m}$ [%]	$\bar{Y}_{10\mu m}$ [%]
^{241}AmO$_2$	11.68	5.49	4.57	99.9	88.9	25.5	14.4	10.0
^{234}UO$_2$	10.15	4.80	4.19	99.9	87.1	24.3	13.9	9.61
^{235}UO$_2$	10.15	4.68	4.00	99.9	85.7	23.5	13.4	9.36
^{237}NpO$_2$	11.10	4.79	3.81	99.9	81.2	21.6	12.5	8.73
^{238}UO$_2$	10.15	4.68	3.36	99.9	78.9	20.8	12.1	8.47

3.5.2 Average Exiting Alpha Energy

The average alpha energy is calculated for all alphas exiting the radioparticulate in Figure 3.11. The average energy initially decreases with diameter until it reaches a local minimum, followed by a gradual hyperbolic increase towarard an apparent limit.
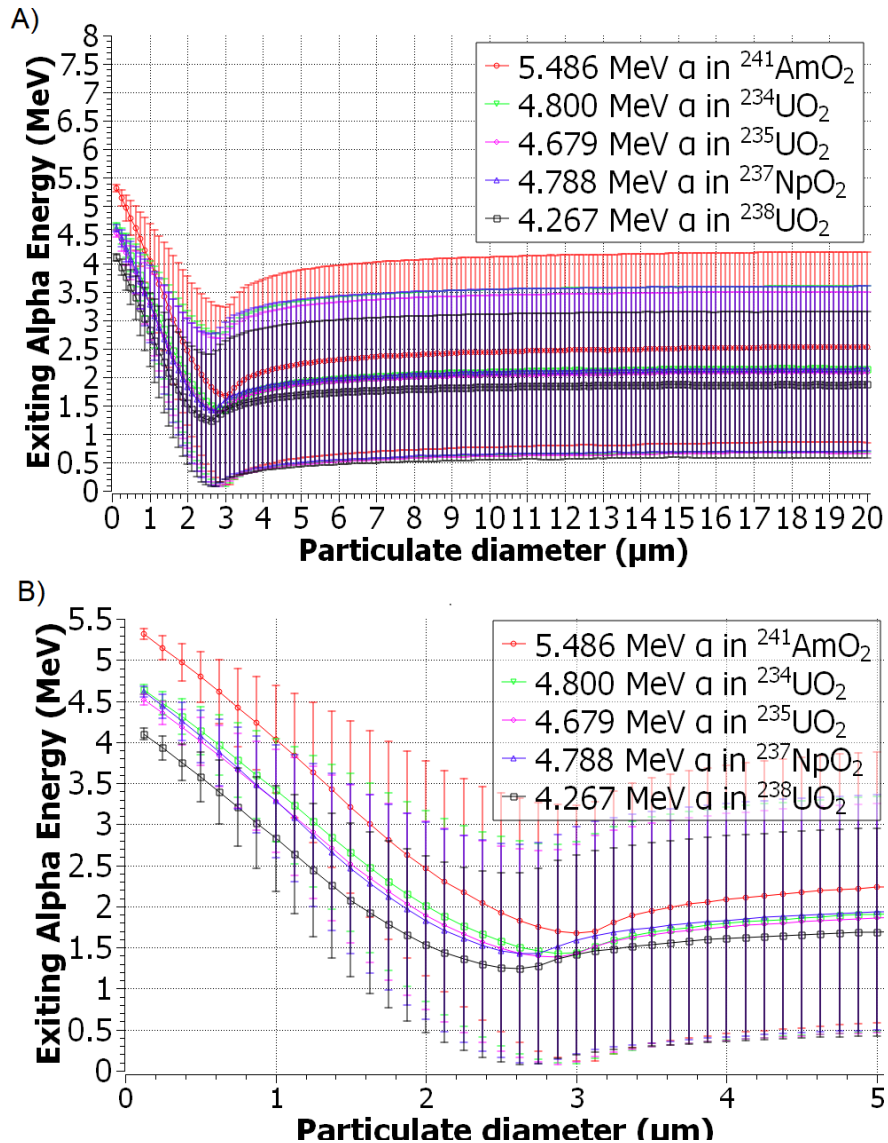
Figure 3.11: Average energy of exiting alpha particles from spherical transuranic oxide particulates (A) with zoom into the first five microns in particle diameter (B).

The initial energy, range, and average final percent of initial energy for exiting radioparticulate alphas across a selection of respirable particle sizes are presented in Table 3.25, alongside respective particulate densities.

Table 3.25: Calculated range and simulated average energy of exiting characteristic alpha particles from each radioparticulate species.

Species	ρ_m [g/cm^3]	E [MeV]	R_m [μm]	$\bar{E}_{1\mu m}$ [%]	$\bar{E}_{2.5\mu m}$ [%]	$\bar{E}_{5\mu m}$ [%]	$\bar{E}_{7.5\mu m}$ [%]	$\bar{E}_{10\mu m}$ [%]
^{241}AmO$_2$	11.68	5.49	4.57	73.5	35.1	40.7	43.3	44.4
^{234}UO$_2$	10.15	4.80	4.19	71.2	32.8	39.7	42.1	43.4
^{235}UO$_2$	10.15	4.68	4.00	70.2	31.9	39.7	42.1	43.3
^{237}NpO$_2$	11.10	4.79	3.81	68.5	30.6	40.3	42.5	43.6
^{238}UO$_2$	10.15	4.68	3.36	66.3	29.4	40.0	41.7	42.7

Chapter 4

Discussion and Conclusions

4.1 Experimental Outcomes

4.1.1 Resuspension Factor Model

The air concentration of traceable micron-sized particulates was modeled using the resuspension factor method. The current generally accepted model stems from a semi-empirical curve fit by Maxwell and Anspaugh (2011), but its predictive power was found to be limited due to the inflated result of the fit and the unphysical nature of the offset. The available historical resuspension factor observations were therefore statistically fit to exponential models with a physical basis using instrumental weighting to find better fitting equation. This initial task provided a means to probe the resuspension model parameters under specific environmental conditions and compare analogous upward rate constants for particle transport.

Physical catenary compartment models were established to provide a theoretical basis for the exponential fit equations. The upward flux in a one compartment system would depend on detailed boundary and internal force conditions, therefore a minimum of two compartments are necessary to define a kinetic rate constant for proportion of upward mobility. Additionally, a closed compart-

mental system implies a lack of interaction with environmental boundaries, which is not likely a reasonable model to use given its lack of application to the outdoor model. A possible exception to this is a closed whole-earth system where the whole 4π steradian ground surface and volume of atmosphere are considered. While this does motivate a relationship between the resuspension factor and the global errosion rate, the application of a global resuspension factor to predictive dosimetry due to a local site exposure is unhelpful due to the variation in local mixing rates. Thus, physical parameterization of these models presents an avenue of research to reconcile the use of historic observations from different sites to construct an average rate of resuspension.

Explicit parameterization of micro-rate constants were determined in terms of fit constant (coefficients and macro-rate constants) for four of the five presented resuspension compartment models. The open three-compartment system, however, contained more unknown variables than there were available conservation equations. Therefore, without either the fixing of rate constants from validated independent measurements or additional systematic observation such as simultaneous soil monitoring, a unique solution for the rate constants cannot be determined from a series air-sampling measurements. This parameterization of the closed three-compartment model, however, provided an analogy to the accepted semi-empirical model whose resuspension factor equation took a similar form. Using the same parameters from the curve-fitting of the available observations, the initial conditions were set to total airborne and total surface release to create visual boundaries of observability (Fig. 3.5). Depending on the prescribed model used, there are major differences of observed resuspension factors between release scenarios, with over 10 orders of magnitude of difference within the first hours to days.

The resuspension of particles under isolated circumstances was experimentally determined using an in-house, low-volume air-sampling system within an indoor static-free chamber. An easily identifiable compound chemically analogous to Americium was deposited in-air or on-surface in order to simulate varying initial conditions, then sampled systematically over the course of hours to days.

90

The particles on the filter were then quantified by neutron activation analysis and related back to air concentration and thus resuspension factor. The results of this experiment demonstrate the extreme sensitivity of the collected mass and therefore the resuspension factor to the initial deposition conditions, height of air sampling collector, and schedule of sampling. At one meter height, resuspension factor measurements from airborne releases were on the order of those from historical observations, whereas the surface release measurements were well below the detection limits of this technique unless sampled for two weeks straight. The schedule of sampling also revealed that oversampling easily occurs even at the low 2 Lpm flow rate of the air sampler; full-day daily sampling technique constantly depleted the chamber and dramatically reduced the resuspension factor over time, where hour-long daily sampling technique demonstrated a replenishing of the mass in the air through an *increasing* resuspension factor.

4.1.2 Impacts upon Inhalation Dose Parameter

The integrated resuspension factor (RF) values were calculated for the time periods used by Maxwell and Anspaugh (2011) as presented in Table 4.1. Additionally, percent deviations in RF between the unfixed regression from this work and previous model predictions are given to illustrate the relative increase or decrease of this work's prediction of inhalation dose.

Table 4.1: Integrated resuspension factors for relative dose effect of regression models, values are in units of $d\ m^{-1}$. Also provided are over- (+) and under-prediction (-) of this work's unfixed (u) regression resuspension factor relative to each model at integral times.

	Integration period [days]				
	0-1	0-10	0-30	0-100	0-365
This work	1.50×10^{-6}	1.33×10^{-5}	3.16×10^{-5}	5.45×10^{-5}	6.73×10^{-5}
This work (u)	1.44×10^{-6}	1.29×10^{-5}	3.07×10^{-5}	5.34×10^{-5}	6.04×10^{-5}
NCRP Model[*]	1.00×10^{-6}	3.30×10^{-6}	4.40×10^{-6}	5.61×10^{-6}	7.91×10^{-6}
	+43.8%	+290%	+597%	+849%	+666%
Double-Exponential[†]	1.89×10^{-6}	1.60×10^{-5}	3.42×10^{-5}	4.86×10^{-5}	5.05×10^{-5}
	-24.0%	-19.5%	-10.3%	+9.6%	+20.1%
Double-Exponential[**]	9.67×10^{-6}	7.20×10^{-5}	1.26×10^{-4}	1.43×10^{-4}	1.46×10^{-4}
	-85.1%	-82.1%	-75.7%	-62.8%	-58.5%
Power-Law[††]	4.47×10^{-5}	1.06×10^{-4}	1.19×10^{-4}	1.26×10^{-4}	1.34×10^{-4}
	-96.8%	-87.8%	-74.2%	-57.7%	-54.8%

[*]NCRP (1999), [†]Maxwell and Anspaugh (2011),
[**]Anspaugh et al. (2002), [††]Maxwell and Anspaugh (2011)

Additionally, RF values were calculated for the same time periods using the *perfect surface* release parameters for the closed two-compartment, open two-compartment, and closed three-compartment models. These are presented in Table 4.2 with comparison to previous models.

Table 4.2: Integrated resuspension factors for relative dose effect of current models compared to *perfect surface release*, 2- and 3-compartment variants of model fits from this work; values are in units of $d\ m^{-1}$.

	Integration period [days]				
	0-1	0-10	0-30	0-100	0-365
2C-closed	$3.39{\times}10^{-12}$	$3.30{\times}10^{-10}$	$2.80{\times}10^{-9}$	$2.58{\times}10^{-8}$	$1.96{\times}10^{-7}$
2C-open	$5.30{\times}10^{-11}$	$4.88{\times}10^{-9}$	$3.71{\times}10^{-8}$	$2.52{\times}10^{-7}$	$1.13{\times}10^{-6}$
3C-closed	$3.33{\times}10^{-10}$	$3.33{\times}10^{-9}$	$9.98{\times}10^{-9}$	$3.33{\times}10^{-8}$	$1.21{\times}10^{-7}$
NCRP Model*	$1.00{\times}10^{-6}$	$3.30{\times}10^{-6}$	$4.40{\times}10^{-6}$	$5.61{\times}10^{-6}$	$7.91{\times}10^{-6}$
Double-Exponential**	$9.67{\times}10^{-6}$	$7.20{\times}10^{-5}$	$1.26{\times}10^{-4}$	$1.43{\times}10^{-4}$	$1.46{\times}10^{-4}$
Double-Exponential†	$1.89{\times}10^{-6}$	$1.60{\times}10^{-5}$	$3.42{\times}10^{-5}$	$4.86{\times}10^{-5}$	$5.05{\times}10^{-5}$

*(NCRP, 1999); **(Anspaugh et al., 2002); †(Maxwell and Anspaugh, 2011)

4.1.3 Radioparticulate Model

The exposure to radiation from micron-sized alpha-emitting particulates was modeled using the Geant4 simulation code. The results of million-event runs present a clear loss of intensity for alpha emitters larger than a few microns, roughly the range of alpha particles in a uniform medium of the particulate compound. For the most part with a few exceptions in NpO_2, the average yield and exiting energy fraction of alphas appear to decrease with respect to the calculated range of respective characteristic alphas by particulate material.

The average energy emitted at the outer surface dramatically decreases with particle size, although this average value then levels out and begins to increase hyperbolically toward a limit. This is due to the loss of alpha particles absorped in the particulate, resulting in an average which is increasingly that of the most outer portion of the particle from which alphas may escape.

4.2 Resuspension Factor Model Outlook

4.2.1 Compartmental Modeling Conclusions

Coefficient and macro-rate constant fits with respective fitting errors of compartment models are provided in Tables 3.1 through 3.4. Based on the trend in reduced-χ^2 values, it appears a fewer-compartment model provides a better goodness-of-fit. The decrease in this parameter is seen to additionally correspond to an increase in fit parameter error among the compartment models.

Though the closest reduced-χ^2 value to unity was found with the closed two-compartment model, the constant offset presents an unphysical airborne equilibrium concentration based on the assumption that airborne quantities cannot exit the system. Therefore, with still reasonable goodness-of-fit, it is the opinion of the author that the open two-compartment model from this work present a fair improvement from the currently accepted model. Further, this model can still be elaborated further with additional kinetic processes by substituting any generic term (e.g. $k_{A \leftarrow S}$) with a sum kinetic rates for each process which contribute to the net rate of transport.

4.2.2 Recommendations for Improvement

The current accepted resuspension factor model is semi-empirical and lacks parameters based on first principles. This investigation laid out the site factors which influence the resuspension of particulates in the environment. While the array of radioparticulates release scenarios are few compared to other sources of fine particle generation, each still present a unique initial particle size distribution and fated dynamic evolution in both the environment and individuals upon exposure. Therefore, predicting the atmospheric fate can be enhanced assuming an available measurement or literature of expected particle size distribution. An N-compartment resuspension factor model based on the work in this study would consider available transport rates and equilibrium terms as a function of the particle size in such an environment (Eq. 4.1), where K_0 carries the m^{-1} dimension through measurements of mass, surface area, and sampled volume. This results in a resuspension

parameter (which itself is proportional to inhalation dose) which must also consider the distribution of particle size deposited in the site (Eq. 4.2). Finally, the total contribution to inhalation dose is the sum of all contributing resuspension parameters by radius (Eq. 4.3).

$$K(r,t) = \sum_i^N K_0 X_i(r) e^{\omega_1(r)t} \tag{4.1}$$

$$KP(r) = \int_{t_1}^{t_2} K(r,t) \times Dp(r) \times e^{-\lambda t} dt \tag{4.2}$$

$$D_{inh} = C_{D,inh} \times \bar{f}_B \times \sum_r KP(r) \tag{4.3}$$

This formulation is ideal direct instrumental analysis, as particle sizers readily discretize sample particle radii. A full theoretical derivation based instead on a known average size distribution requires the additional work of assigning sensitivities of each species of interest to changes in influencing factors (such as wind, temperature, etc.) in order to produce such a characteristic size distribution. Additionally, the self-shielding of the spherical radioparticulate can theoretically be accounted for using the results of this study. The yield and average fractional exiting energy are directly proportional to the dose received by an organ from the source. Therefore, the incorrect assumption of total alpha quantity and energy deposition in the inhalation dose can be fixed by directly factoring them within the radius summation: (Eq. 4.4).

$$D_{inh} = C_{D,inh} \times \bar{f}_B \times \sum_r KP(r) \times \bar{Y}_\alpha(r) \times \frac{\bar{E}_\alpha(r)}{E_\alpha(0)} \tag{4.4}$$

4.3 Future Experimental Directions

4.3.1 Aerosol Particulate Size Distribution

The particle size distribution governs many key kinetic transport rates and thus would be an ideal comparative investigation. In particular, measurements with smaller respirable particle sizes such as *nanopowder* in the range of 100-1000 nm using the same resuspension chamber setup would be expected to yield an enhanced resusupension factor. This would be due to relative increase in the ratio of upward forces to downward forces on a smaller mass, which would be in line with a classical statistical distribution in a gravitational potential. Furthermore, a mixture of particle sizes such as nanopowder and the micron-sized masses used in this experimental study may then present multiple resuspension factor processes over time, best expressed with a model like Eq. 4.1

4.3.2 Surface Material

The chemistry between the particulate material and the structures of different surfaces can give rise to a range additional interactions. Some interactions like complexing and absorption can reduce the overall availability of surface-bound particles to suspend which would reduce the resuspension factor. Porous or organic material may have additional downward pathways to remove particles from the surface, however a more accurate outdoor organic model may have bioturbators which would likely mix and further remove particles from the surface. If an experiment is set such that there is a depth-based deposition in soil, the bioturbators might then have the opposite effect and make more particles available to suspend.

4.3.3 Weathering Perturbations

This experiment demonstrated the sensitivity of low-level resuspension factor measurements to the presence of turbulent air flow. The lack of outdoor weather events provided values lower than detection limits within acceptable confidence intervals for the standard sampling height of one meter. At closer proximity (0.25 meter), the measured values were lower than expected but

within acceptable detection limits. This observation presents a convolution of: 1) the sampling air flow providing a stronger resuspending force, and 2) the resuspension of particles following a distribution wherein more particles are found at lower altitudes. Investigating the kinetic rate constant for various weathering events such as wind, humidity, and rainfall, will be possible from the perspective measuring net upward particle flux (individual resuspension rates). For the purpose of a more general resuspension factor prediction, a height distribution model must be determined and used to establish the relationship between sampling height and collected mass.

4.3.4 Radioparticulate Structure

The simulation study here investigated spherical particulates to establish a first-order approximation of the exiting alpha flux. The composition was assumed to be a uniform density of a homogenous oxide of the radioisotope. Variations in this composition, including stable nuclides (such as environmental dust) and other radionuclides can influence the resulting exiting flux. The former variation would surely reduce the specific activity of the particle, though both of these variations will have complicating effects on shielding alphas due to the difference in alpha cross-sections relative to the homoegenous model. Finally, the recoil of homogenous radioparticles due to electrostatic buildup and resulting discharge from the stochastic radioactive decays may also have an impact on a measured resuspension factor. These new or spent "fuel fleas", may then remain suspended due to this recoil, and can confound the upward kinetic rate constant from other mechanisms.

References

L.R. Anspaugh, S.L. Simon, K.I. Gordeev, I.A. Likhtarev, R.M. Maxwell, and S.M. Shinkarev. Movement of radionuclides in terrestrial ecosystems by physical processes. *Health Physics*, 82(5): 669–679, 2002.

A. Brodsky. Resuspension factors and probabilities of intake of material in process (or 'is 10 to the -6 a magic number in health physics?'). *Health Physics*, 39(6):992–1000, 1980.

R.D. Brook, S. Rajagopalan, and C.A. Pope III et al. Particulate matter air pollution and cardiovascular disease: An update to the scientific statement from the american heart association. *Circulation*, 121(21):2331–2378, 2010.

K. Bunzl, W. Kracke, W. Shimmack, and K. Auerswald. Migration of fallout pu-239+240, am-241 and cs-137 in the various horizons of a forest soil under pine. *Journal of Environmental Radioactivity*, 28:1734, 1995.

E. Caffrey, M. Johansen, J. Caffrey, and K. Higley. Comparison of homogenous and particulate lung dose rates for small mammals. *Health Physics*, 112:526–532, 2017.

G. Caruso, M. Nobili, and L. Ferroni. Modelling of dust resuspension in tokamak devices during an air inflow event. *Journal of Fusion Energy*, 34:1039–1050, 2015.

F. Chawla, P. Steinmann, H-R. Pfeifer, and P. Froidvaux. Atmospheric deposition and migration of

artificial radionuclides in alpine soils (val pioria, switzerland) compared to distribution of selected major and trace lements. *Science of the Total Environment*, 408:3292–3302, 2010.

O.G. Chkhetiani, E.B. Gledzer, M.S. Artamonova, and M.A. Iordanskii. Dust resuspension under weak wind conditions: direct observations and model. *Atmospheric Chemistry and Physics*, 12: 5147–5162, 2012.

L.A. Currie. Limits for qualitative detection and quantitative determination. *Analytical Chemistry*, 40:586–593, 1968.

M.J. Daniels, F. Dominici, J.M. Samet, and S.L. Zeger. Estimating pariticulate matter-mortality dose-response curves and threshold levels: An analysis of daily time-series for the 20 largest us cities. *American Journal of Epidemiology*, 152(5):397–406, 2000.

D. Delacroix, J.P. Guerre, P. LeBlanc, and C. Hickman. Radionuclide and radiation protection data handbook. *Radiation Protection Dosimetry*, 98(1), 2002.

D.D. DiJulio, C.P. Cooper-Jensen, I. Llamas-Jansa, S. Kazi, and P.M. Bentley. Measurements and monte-carlo simulations of the particle self-shielding effect of b4c grains in neutron shielding concrete. *Radiation Physics and Chemistry*, 147:40–44, 2018.

D.W. Dockery. Health effects of particulate air pollution. *Annals of Epidemiology*, 19(4):257–263, 2009.

H. Domenech. *Radiation Saftey: Management and Programs.* Springer, 2017.

M. Dreicer, T.E. Hakonson, C.G. White, and F.W. Whicker. Rainsplash as a mechanism for soil contamination of plant surfaces. *Health Physics*, 46(1):177–187, 1984.

M. Eisenbud and T. Gesell. *Environmental Radioactivity from Natural, Industrial, and Military Sources.* San Diego, CA: Academic Press, 4 edition, 1997.

EPA. Environmental protection agency. pag manual: Protective action guides and planning guidance for radiological incidents. Technical Report EPA 400-R-17-001, U.S. Environmental Protection Agency, Office of Radiation and Indoor Air, Washington, D.C., 2017.

N.D.M. Evans. Binding mechanisms of radionuclides to cement. *Cement and Concrete Research*, 38:543–553, 2008.

FRMAC. FRMAC assessment manual, volume 1, overview and methods. Sandia Report SAND2015-2884R, Federal Radiological Monitoring and Assessment Center, Albuquerque, NM, Apr. 2018.

K.A.A. Gamage and M.J. Joyce. An analytical approach to gamma-ray self-shielding effects for radioactive bodies encountered nuclear decommissioning scenarios. *Applied Radiation and Isotopes*, 69:1521–1532, 2011.

B.W. Gardner and J.C. Crespi. Characterizing the fluence of wpi's new deuterium-deuterium neutron generator. *Worcester Polytechnic Institute*, 2015.

E.K. Garger, V. Kashpur, G. Belov, V. Demchuk, J. Tschiersch, F. Wagenpfeil, H.G. Paretzke, F. Besnus, W. Hollander, J. Martinez-Serrano, and I. Vintersved. Measurement of resuspended aerosol in the chernobyl area i. discussion of instrumentation and estimation of measurement uncertainty. *Radiation Environmental Biophysics*, 1997.

E.K. Garger, F.O. Hoffman, K.M. Thiessen, D. Galeriu, A.I. Kryshev, T. Lev, C.W. Miller, S.K. Nair, N. Talerko, and B. Watkins. Test of existing mathematical models for atmospheric resuspension of radionuclides. *Journal of Environmental Radioactivity*, 42:157–175, 1999.

J.A. Garland. Some recent studies of the resuspension of deposited material from soil and grass. *Precipitation scavaging, dry deposition, and resuspension*, pages 1087—-1097, 1983.

J.A. Garland and I.R. Pomeroy. Resuspension of fall-out material following the chernobyl accident. *Journal of Aerosol Science*, 25(5):793–806, 1994.

A.R. Harris and C.I. Davidson. Particle resuspension in turbulent flow: A stochastic model for individual soil grains. *Aerosol Science and Technology*, 42:613–628, 2008.

R.M. Harrison and J. Yin. Particulate matter in the atmosphere: which particle properties are important for its effects on health? *Science of the Total Environment*, 249:85–101, 2000.

C. Henry and J-P. Minier. Progress in particle resuspension from rough surfaces by turbulent flows. *Progress in Energy and Combustion Science*, 45:1–53, 2014.

ICRP. Human respiratory tract model for radiological protection. *ICRP Publication 66*, 1994.

ICRP. Individual monitoring for internal exposure of workers. *IRCP Publication 78*, 1997.

E. Karlsson, I. Fangmark, and T. Berglund. Resuspension of an indoor aerosol. *Journal of Aerosol Science*, 27(Supplement 1):S441–S442, 1996.

J.M. Kaste, A.M. Heimsath, and B.C. Bostick. Short-term soil mixing quantified with fallout radionuclides. *Geology*, 35:243–246, 2007.

Y. Kim, G. Wellum, K. Mello, K.E. Strawhecker, R. Thoms, A. Giaya, and B.E. Wyslouzild. Effects of relative humidity and particle and surface properties on particle resuspension rates. *Aerosol Science and Technology*, 50(4):339–352, 2016.

M.E. Krar and K.F. Milad. Direct mathematical calculation of the self-shielding factor for cylindrical radioactive sources. *Journal of Taibah University for Science*, 10:266–270, 2015.

W.H. Langham. Plutonium distribution as a problem in environmental science. *Proceedings of Environmental Plutonium Symposium*, LA-4756:3–11, 1971.

W.H. Langham, P.S. Harris, and T.L. Shipman. Plutonium hazards created by accidental or experimental low-order detonation of atomic weapons. Technical Report LA-1981, Los Alamos: Los Alamos National Laboratory, 1955.

M.S. Lee and C.W. Lee. Association of fallout-derived cs-137, sr-90 and pu-239, pu-240 with natural organic substances in soils. *Journal of Environmental Radioactivity*, 47:25362, 2000.

David R. Lide. *CRC Handbook of Chemistry and Physics*. CRC Press, 87 edition, 2006.

G. Lujaniene, P. Benes, K. Stamberg, and T. Sciglo. Kinetics of plutonium and americium sorption to natural clay. *Journal of Environmental Radioactivity*, 108:4149, 2012.

S.A. Marshall, C.A. Potter, and D.C. Medich. Reassessment of resuspension factor following radionuclide dispersal. *Health Physics*, 114(5):500–506, 2018.

G. Matisoff, M.E. Ketterer, K. Rosén, J.W. Mietelski, L.F. Vitko, H. Persson, and E. Lokas. Downward migration of chernobyl-derived radionuclides in soils in poland and sweden. *Applied Geochemistry*, 26:105–115, 2011.

R.M. Maxwell and L.R. Anspaugh. An improved model for prediction of resuspension. *Health Physics*, 101(6):722–730, 2011.

B.J. Merrill and P.W. Humrickhouse. Aerosol resuspension model for melcor for fusion and very high temperature reactor applications. Technical Report INL/EXT-10-19683, Idaho National Laboratory, 2011.

A. Mori, W.R. Alexander, H. Geckeis, W. Hauser, T. Schaefer, J. Eikenberg, Th. Fierz, C. Degueldre, and T. Missana. The colloid and radionuclide retardation experiment at the grimsel test site: Influence of bentonite colloids on radionuclide migration in a fractured rock. *Colloid and Surfaces A*, 217:3347, 2003.

H.M. Moussa. Dust particle size effects on absorbed fraction values in the anterior nose. *Health Physics*, 93:307–311, 2007.

H. Muller-Lemens and F. van Dorp. Bioturbation as a mechanism for radionuclide transport in soil: Relevance of earthworms. *Journal of Envronmental Radioactivity*, 31:7–20, 1996.

S.P. Murarka. Neutron activation analysis. *Encyclopedia of Materials: Science and Technology*, 2001.

NCRP. Recommended screening limits for contaminated surface soil and review of factors relevant to site-specific studies. Technical Report 129, National Council on Radiation Protection and Measurements, 1999.

NMIII. Neutron capture. http://nmi3.eu/neutron-research/techniques-for-/chemical-analysis.html, 2012. [Image]. Accessed: 2017-07-17.

NRC. H122 - basic health physics - air sampling equations. *ML11229A717*, 2011.

NRC. H201 - health physics technology - chapter 5. *ML1126A163*, 2012.

NRC. Standards for protection against radiation. 2020.

F. Parozzi, L. Biasi, S. Paci, and L. Tagliaferri. Meeting on nuclear aerosols in reactor safety. Technical report, Centro Elettrotecnico Sperimentale Italiano, 1998.

R. Pollanen. Nuclear fuel particles in the environment: characteristics, atmospheric transport, and skin doses. *University of Helsinki*, Thesis, 2002.

D. Sahin and K. Unlu. Determination of self shielding factors and gamma attenuation effects for tree ring samples. *Journal of Radioanalytical Nuclear Chemistry*, 291:549–553, 2012.

B. Salbu and O.C. Lind. Radioactive particles released from various nuclear sources. *Radioprotection*, 40:S27–S32, 2005.

G. Sanchez and J. Lopez-Fidalgo. Mathematical techniques for solving analytically large compartmental systems. *Health Physics*, 85(2):184–193, 2003.

L.W. Stanek, J.D. Sacks, S.J. Dutton, and J.B. Dubois. Attributing health effects to apportioned components and sources of particulate matter: an evaluation of collective results. *Atmospheric Environment*, 45:5655–5663, 2011.

K. Supriya. Top 3 sampling methods for flowing water. http://www.environmentalpollution.in/wp-content/uploads/2016/07/clip_image002-19.jpg, 2016. Accessed: 2019-09-14.

A. Trkov, G. Zerovnik, L. Snoj, and M. Ravnik. On the self-shielding factors of neutron activation analysis. *Nuclear Instruments and Methods in Physics Research Section A: Accelerators, Spectrometers, Detectors and Associated Equipment*, 610:553–565, 2009.

J.E. Turner. *Atoms, Radiation, and Radiation Protection*. Pergamon Press, 1986.

U. Tveten. Environmental consequences of releases from nuclear accidents, a nordic perspective. Technical Report AKTU-200, Kjeller, Norway: Institute for Energy Technology, 1990.

C. Valentin, J. Kratky, and A. Brandl. Investigation of alpha and beta self-absorption factors in the calibration of water sample measurements. *Health Physics*, 103:S124–S130, 2012.

P. Vicini, H-T Su, and J.J. DiSTefano III. Identifiability and interval identifiability of mammillary and catenary compartmental models with some known rate constants. *Mathematical Biosciences*, 167:145–161, 2000.

P. Vilks and D.B. Bachinski. Colloid and suspended particle migration experiments in a granite fracture. *Journal of Contaminant Hydrology*, 21:269–279, 1996.

J. Voss. Los alamos radiation monitoring notebook. *Los ALamos National Laboratory*, LA-UR-00-2584, 2001.

WHO. Health and the environment: addressing the health impact of air pollution (resolution a68.8). Technical report, Geneva: World Health Organization, 2015.

Z. Xu, T. Jordan, and W. Breitung. Particle resuspension model for subatmospheric conditions. *IEEE Transactions on Plasma Science*, 44(9):1662–1665, 2016.

G. Ziskind, M. Fichman, and C. Gutfinger. Resuspension of particulates from surfaces to turbulent flows - review and analysis. *Journal of Aerosol Science*, 26(4):613–644, 1995.